Three-Dimensional Aero-Thermal Optimization of Film Cooling in a High Pressure Turbine

Carole El Ayoubi

A Thesis

In the Department of

Mechanical and Industrial Engineering

Presented in Partial Fulfillment of the Requirements

For the Degree of

Doctor of Philosophy

Concordia University

Montreal, Quebec, Canada

May 2014

CONCORDIA UNIVERSITY

School of Graduate Studies

This is to certify that the thesis prepared

By: **Carole El Ayoubi**

Entitled: **Three-Dimensional Aero-Thermal Optimization of Film Cooling in a High Pressure Turbine**

and submitted in partial fulfilment of the requirements for the degree of

Doctorate of Philosophy

complies with the regulations of the University and meets the accepted standards with respect to originality and quality.

Signed by the final examining committee:

_____ Dr. Fariborz Haghighat (Chair)

_____ Dr. Marius Paraschivoiu (Examiner)

_____ Dr. Nabil Esmail (Examiner)

_____ Dr. Christopher Trueman (Examiner)

_____ Dr. Jean-Yves Trepanier (Examiner)

_____ Dr. Wahid S. Ghaly (Supervisor)

_____ Dr. Ibrahim G. Hassan (Supervisor)

Approved by _____

MIE Department Chair or Graduate Program Director

_____2014 _____

Dean, Faculty of Engineering and Computer Science

ABSTRACT

Three Dimensional Aero-Thermal Optimization of Film Cooling in a High Pressure Turbine

Carole El Ayoubi, Ph.D.

Concordia University, 2014

Development of effective discrete film cooling is recognized as an essential task in gas turbine design since it has been shown necessary to ensure an acceptable turbine component life-time. Traditional design of film cooling schemes is driven by a single objective, maximizing the cooling performance. The aerodynamic penalty resulting from the coolant injection is generally neglected. Achieving an aero-thermal design of film cooling is a challenging task as it is based on two competing objectives; attaining a high thermal protection of the airfoil from the hot mainstream gas usually results in deteriorating the aerodynamic efficiency.

The present research addresses this challenge and investigates the complex flow underlying the aero-thermal interaction on a film cooled airfoil. The simultaneous effects of film coolant flow parameters and film hole geometric variables on the aerodynamic loss and the cooling effectiveness are examined. Trends in design variations to minimize the aerodynamic penalty, while maintaining a high cooling performance are established.

The research objective is achieved by implementing an automated optimization procedure that consists of a non-dominated sorting genetic algorithm coupled with an artificial neural network. The latter is used to provide prediction of the objective function at every optimization iteration

and reduces computation time. It is constructed based on numerical flow simulations where the three dimensional Reynolds-Averaged Navier-Stokes equations are solved.

The optimization methodology is applied on a typical high-pressure turbine with two staggered rows of discrete film cooling on the suction side. The Pareto front of optimal solutions is generated. The thermal, aero-thermal, and aerodynamic optimums are identified and investigated numerically. A subsonic wind-tunnel facility available in Concordia University is used to re-create experimentally the optimum design points. Measured experimental data allowed verification of the CFD model, and substantiated the optimization methodology as a reliable design tool for film cooling in turbomachinery applications.

ACKNOWLEDGMENTS

I would like to thank my supervisors Dr. Ibrahim Hassan and Dr. Wahid Ghaly for the opportunity they have given me to conduct research under their supervision at Concordia University. They have both provided me with great guidance and insight that was invaluable to the completion of this work.

I would also like to thank my colleagues, especially Dr. Othman Hassan who has given support with experimental manipulations and has always been generous with advice. I would also like to thank Haoming Li whose experience with CFD software was valuable. Many thanks go to Amen Younes, Fan Yan Feng, Kristina Cook, Yingjie Zheng, and Qian You for always providing support and advice. Big thanks go to Hamza Assi for his solid technical support with engineering drawings, his work is greatly appreciated.

Finally, this work is dedicated to my family whose unconditional love and support has carried me through this journey.

Table of Contents

List of Figures

List of Tables

List of Acronyms

AL	Aerodynamic loss
BR	Blowing ratio, $\rho_c U_c / \rho_\infty U_\infty$
C	Blade true chord, mm
CA	Compound angle
C_x	Blade axial chord, mm
c_p	Heat capacity at constant pressure, J/K
C_p	Total pressure loss coefficient, $(p_{0in} - p_{0e}) / p_{0in}$
D	Cooling hole tube diameter, mm
DR	Density ratio, ρ_c / ρ_∞
e	Specific internal energy, J
h	Heat transfer coefficient, $W/m^2 \cdot K$
k	Turbulence kinetic energy, m^2/s^2
k	Thermal conductivity, $W/m \cdot K$
L	Hole tube length, mm
L_c	Non-diffused hole tube length, mm
M	Mach number

$\dot{m}$	Mass flow rate, kg/s
p	Pressure, Pa
R	Ideal gas constant of air, J/kg·K
Re	Reynolds number, $(\rho \cdot U \cdot C) / \mu$
s	Curvilinear distance over airfoil surface, mm
T	Temperature, K
Tu	Turbulence
u_τ	Friction velocity at the wall, m/s
U	Velocity, m/s
x	Streamwise coordinate, mm
y	Vertical coordinate, mm
y^+	Non-dimensional wall distance, $u_\tau \cdot y / \upsilon$
z	Spanwise coordinate, mm

Greek letters

α	Hole injection angle
β	Conical diffusion angle
ε	Turbulence eddy dissipation, m^2/s^3

η	Adiabatic cooling effectiveness, $(T_{aw} - T_\infty) / (T_c - T_\infty)$
γ	Heat capacity ratio
Θ	Non-dimensional temperature, $(T - T_\infty) / (T_c - T_\infty)$
μ	Dynamic viscosity, kg/m·s
υ	Kinematic viscosity, m^2/s
ρ	Density, kg/m^3
ω	Specific turbulence dissipation rate, 1/s

Subscripts and Superscripts

aw	Adiabatic wall
c	Coolant
e	Exit
f	Film
h	Hole exit
i, j	Running index
in	Inlet
obj	Objective
span	Spanwise or laterally averaged

surf	Surface averaged
w	Wall conditions
0	Stagnation condition
∞	Mainstream conditions

Abbreviations

2D	Two-dimensional
3D	Three-dimensional
AL	Aerodynamic loss
ANN	Artificial neural network
BR	Blowing ratio
CFD	Computational fluid dynamics
DB	Database enrichment
GA	Genetic algorithm
LHS	Latin hypercube sampling
RANS	Reynolds-averaged Navier-Stokes
RSA	Response surface approximation
SST	Shear stress transport

Introduction

Modern gas turbine engines operate at turbine inlet temperatures that are beyond the melting threshold of turbine components. Film cooling of turbine rotors and stators has therefore become a common practice in turbine design, where low temperature air is bled from a compressor stage, bypassing the combustor, and ejected from discrete holes on the turbine airfoil surface to provide a film protection to the airfoil metal from the very high mainstream gas temperature. Film cooling technology has received much attention as it ensures a reasonable lifetime for turbine components and allows even higher turbine inlet temperatures. However, the coolant interacts with the mainstream flow, and aerodynamic and thermal losses incur due to the mixing that takes place between the coolant and mainstream flows. Mixing losses result from the coolant being ejected at temperature and velocity different from the mainstream. The best compromise between a high cooling performance and a low aerodynamic penalty becomes a major objective in cooled turbine airfoil design.

Considerable effort in literature has been dedicated to improving the coolant coverage of the airfoil surface, which translates into a better cooling performance. The latter is measured in terms of the film cooling effectiveness. Extensive research, available in literature, is devoted to the study of numerous geometric and flow parameters that have a direct impact on film cooling performance. The geometry investigations included the airfoil geometry profile or the effects of convex and concave curvatures, Chen et al. (2001), Gao et al. (2007), and the film cooling hole geometry, Ghorab and Hassan (2010). The investigated flow parameters encompassed the coolant to mainstream temperature ratio and the mass flux ratio, known as the blowing ratio (BR), Garg and Gaugler (1996), the mainstream Reynolds number, Baldauf and Scheurlm

(1996), and the mainstream and coolant turbulence intensity, Al-Hamadi et al. (1998), Mehendale et al. (1994), Mayhew et al. (2003), among others. However, research devoted to the impact of film cooling on the aerodynamic loss is limited. The studies available in literature quantified the effects on aerodynamics by computing the total pressure loss or the integrated aerodynamic loss downstream of the airfoil, Jackson et al. (2000), Chappell et al. (2010). Several attempts to define the efficiency of a cooled turbine cascade were recorded, but no general consensus exists, Hartsel (1972), Young and Horlock (2006).

Furthermore, as computing power has been steadily increasing and is becoming more affordable, automated aerodynamic shape optimization has become a viable design tool. Aerodynamic shape optimization techniques rely mostly on the concept of coupling heuristic/evolutionary optimization algorithms with a three-dimensional computational fluid dynamics (CFD) solver. A surface response approximation reduces the computational time by minimizing the number of calls between the optimization algorithm and the CFD solver. This methodology permits the designer to explore the design space in an automated manner to find a global optimum. Heuristic/evolutionary optimization algorithms are used to this intent instead of the traditional gradient-based techniques because aerodynamic design problems are complex and usually encompass many local minima or maxima. A gradient-based technique can easily converge towards a local minimum/maximum, neglecting to explore the remaining design space for other minima/maxima. Therefore, a trial and error technique is usually required when using a gradient-based algorithm to obtain the global optimum. Contrarily, an evolutionary algorithm, such as, the genetic algorithm has proven to be more reliable to detect global minima/maxima and has been applied increasingly to aerodynamic optimization tasks.

Shape optimization of aerodynamic profiles of vanes and blades in two dimensional as well as three dimensional flows has been conducted by specifying the objective function to be either the total pressure loss or the aerodynamic efficiency, e.g. Dennis et al. (1999), Wang and Damodaran (2001), Oyama et al. (2004), Mengistu and Ghaly (2003), Mengistu and Ghaly (2004), Mengistu and Ghaly (2008), Arabnia and Ghaly (2009).

However, not many authors have applied this technique to film cooled turbine blades or vanes. Lee and Kim (2010) have successfully implemented the simulated annealing optimization algorithm coupled with a weighted average surrogate model to optimize the geometry of a shaped film-cooling hole on a flat plate yielding a maximum film cooling effectiveness, which was spatially averaged over the entire surface of the plate. Subsequently, Lee et al. (2013) performed a multiple objective optimization and tried to maximize the film cooling effectiveness while minimizing the aerodynamic loss for a row of laidback fan-shaped cooling holes on a flat plate in subsonic flow (inlet Mach number of 0.3). They were successful in obtaining the Pareto front of optimal solutions, which were characterized by low values of hole exit width to hole pitch ratio, and hole exit area to hole inlet area ratio. Their optimal solutions were assessed through CFD flow simulations using the shear stress transport model (SST) for turbulence closure. For a blowing ratio of 0.5, the optimization decreased the thermal objective function by a maximum of 30% for the best optimum thermal solution, and decreased the aerodynamic objective function by 25% for the best optimum aerodynamic solution. The thermal objective function was defined as the inverse of the surface average of the film cooling effectiveness, whereas, the aerodynamic objective function was defined as the ratio of area-averaged actual to theoretical kinetic energies.

Literature indicates that there exists a need for investigating further the complex interaction between coolant and mainstream flows in turbine cascades. Furthermore, many film cooling studies have neglected the impact of the film cooling technique on the overall aerodynamic loss of the turbine. Numerous investigations aimed to design novel film cooling schemes such as to increase the film cooling effectiveness, but did not consider the resulting aerodynamic loss, e.g. Ghorab and Hassan (2010), Kusterer et al. (2007, 2011). The design of a film cooling scheme should achieve a high film cooling effectiveness while ensuring a minimum aerodynamic loss.

The motivations of the present work stem from the need to achieve an optimum aero-thermal film cooling design that ensures a maximum airfoil surface protection while maintaining to a minimum the impact of the film cooling technique on the aerodynamic efficiency.

The research goals are achieved by implementing a heuristic optimization approach. An objective function for the optimization is properly formulated to allow simultaneous reduction of the aerodynamic loss and increase of the film cooling effectiveness. The optimization procedure employs a genetic algorithm coupled with a response surface approximation algorithm of the artificial neural network (ANN) type. The ANN is used to approximate the objective function and is trained and tested using a set of design candidates equally spaced in the design space and selected using the Latin Hypercube Sampling (LHS) method. The objective function computation for the LHS design candidates is accomplished by solving the three-dimensional Reynolds-Averaged Navier-Stokes equations with the commercial CFD software ANSYS CFX v12.1.

The proposed optimization methodology is implemented on a typical high-pressure turbine airfoil. The airfoil experiences film cooling on its suction side where a double row of discrete

film holes are placed in a staggered arrangement. The methodology attempts to firstly optimize the film coolant flow parameters, and secondly, the film hole geometric parameters while taking into account the current machining limitations in the industry. The results are verified experimentally, and the methodology is therefore substantiated and proven as a reliable tool in turbomachinery film cooling design.

CHAPTER 1

Literature Review

The present chapter lays out a literature survey that focuses on four main axes; the advancements in film cooling hole technology, the developments in numerical modeling of film cooling, the relationship between film cooling and aerodynamic efficiency, and global optimization techniques applied to either aerodynamic or film cooling design problems.

1.1. Review of film cooling hole technology

Film cooling is achieved by injecting cold air through rows of evenly spaced discrete film cooling holes on the surface of turbine airfoils. The classical hole shape is round and referred to as the cylindrical hole. As research has focused on improving the film cooling performance, only one main technological advancement has been achieved in film cooling hole design and consists of shaping the hole exit. Shaped holes can be classified into four different categories: the conically flared, the laidback, the fanshaped, and the laidback-fanshaped hole which is a combination of the previous two. Figure 1-1 presents schematics of the cylindrical hole and the four categories of the shaped hole.

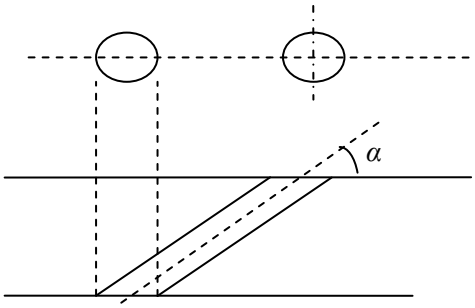

Cylindrical hole

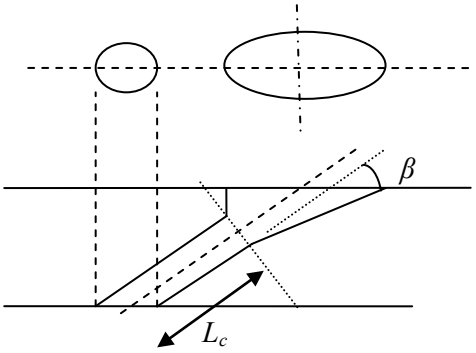

Conical

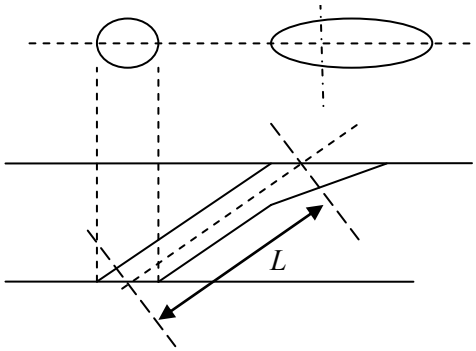

Laidback

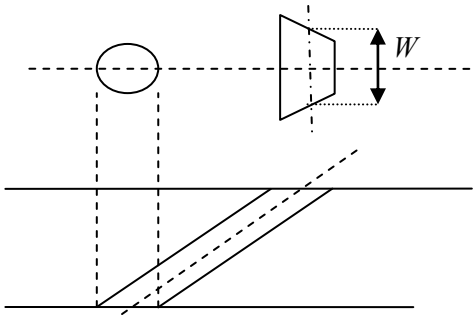

Fanshaped

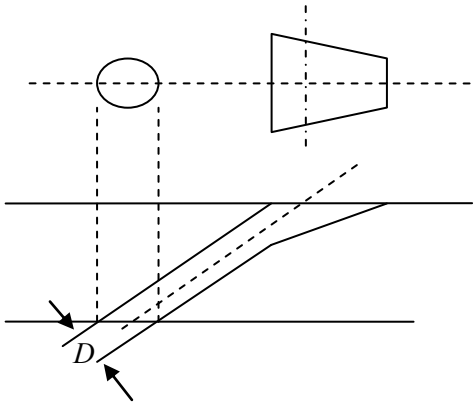

Laidback fanshaped

Figure 1-1: The cylindrical hole and the geometric variations of a shaped cooling hole; Bunker (2005)

The current section lists a chronological review of shaped hole studies that categorized the effects of geometry variations on film cooling effectiveness. Most researchers compared the performance of shaped holes to that of the classical cylindrical hole, either on a flat plate or on the surface of an airfoil. The main geometric parameters that have been used in literature to define a cooling hole, whether shaped or cylindrical, are enumerated below:

- Length to diameter ratio (L / D) is used to define the length of the cooling hole tube below the turbine airfoil surface.
- Injection angle (α) is used to define the inclination angle of the cooling hole tube with respect to the mainstream (horizontal) direction.
- Lateral expansion angle (β) is a measure of the lateral shaping of the hole exit. In case of a cylindrical hole, this angle is equal to zero.
- Forward expansion angle (Υ) is a measure of the forward shaping of the hole exit. In case of a cylindrical hole, this angle is nil. In case of a conically flared hole, the lateral and forward expansion angles are equal.
- Compound angle (CA) is a measure of the direction of coolant injection in the lateral direction.
- Hole pitch to diameter ratio (P / D) is a measure of the spacing between adjacent cooling holes in the same row of holes.
- Hole width to pitch ratio (W / P) is used with fanshaped holes only instead of the lateral expansion angle. W is the size of the breakout side of the hole exit. It allows evaluating the coolant surface coverage at the hole exit.
- Hole exit to inlet area ratio (A_{exit} / A_{inlet}) may be used instead of specifying lateral and forward expansion angles.

Bunker (2005) presented an impeccable review of film cooling hole technology research and advancements that had been achieved in the last 30 years. He noted that Goldstein (1974) was the first to quantify the improvements in film cooling performance due to hole shaping. Many researchers followed the footsteps of Goldstein, most notably Gritsch et al. (1998), to show that expanded hole exits provide significant improvement in film cooling effectiveness compared to cylindrical exits, and avoid coolant lift-off at high blowing ratios.

Therefore, the superior performance of shaped holes was widely recognized in film cooling literature. The principle behind shaping a hole exit was summarized by York and Leylek (2003). As the cross sectional area increases gradually towards the exit, the average coolant velocity decreases due to the diffusion; because the velocity is inversely proportional to the area. Provided a uniform velocity at the hole exit is achieved, the momentum of the coolant decreases with the square of the velocity. This allows the coolant to remain closer to the surface yielding a better protection of the surface at a given blowing ratio in comparison to a cylindrical hole.

Subsequent efforts focused on perfecting the coolant coverage. Further analysis was performed of the geometric parameters affecting the performance of shaped holes. Gritsch et al. (1998), Thole et al. (1998), and Gritsch et al. (2000) stated that laidback fanshaped holes yielded higher film cooling effectiveness than fanshaped holes.

Subsequently, Gritsch et al. (2005) performed an experimental sensitivity analysis of the shaped hole cooling effectiveness to some geometric parameters. The authors investigated the effects of the area ratio (A_{exit} / A_{inlet}), the pitch to diameter ratio (P / D), the hole length (L / D), coverage (W / P), and compound injection (CA). Blowing ratios ranged between 0.5 and 2.5, and the hole length was found to have insignificant effect on the laterally averaged adiabatic film cooling

effectiveness. The authors also found that there exists an optimal P / D ratio for a specific operating condition. As for the W / P ratio, it is defined such as a small ratio indicates a forward diffusing hole, whereas a large ratio indicates a laterally expanded hole. It was found that neither W / P nor the area ratio significantly affected the effectiveness. At low blowing ratios the compound angle effect was also found negligible, whereas at higher blowing ratios it seemed to reduce the cooling effectiveness.

Taslim and Khanicheh (2005) conducted an experimental investigation to compare the film cooling performance of a single row of compound laidback fanshaped holes on a flat plate to a single row of compound cylindrical holes. The shaped holes outperformed the cylindrical holes especially at higher blowing ratios. The increased film cooling effectiveness was attributed to a reduction in the penetration of the coolant into the mainstream, hence lower diffusion, a reduction in velocity gradients due to the larger hole exit area, and an increase in lateral spreading.

Gao et al. (2007) conducted experimental measurements on a high pressure turbine blade with film cooling on suction and pressure sides. The cooling holes were laidback fanshaped. Two injection types were investigated; axial and compound. The axial laidback fanshaped holes were shown to provide uniform and wide coolant coverage at all blowing ratios, and provided the best cooling performance at moderate blowing rates. Compound injection yielded higher effectiveness values especially at higher blowing rates.

Saumweber and Schulz (2008) investigated the effects of the lateral expansion angle (β), the inclination angle (α), and the hole length (L / D) on the film cooling effectiveness for a fanshaped hole on a flat plate. They also compared the performance of the shaped hole to that of

the standard cylindrical hole. They showed that increasing the lateral expansion angle widens the lateral spreading of the coolant, and shortens the cooled surface area at low blowing rates. However, compared to a cylindrical hole, a fanshaped hole avoids coolant lift-off at relatively low expansion angles. Furthermore, increasing the injection angle was found to shorten the cooled surface area but widen the coolant footprint, as a steeper angle increased the coolant penetration into the mainstream. It decreased the laterally averaged film cooling effectiveness, and the effect of the inclination angle was more pronounced at higher blowing rates. Increasing the hole length was found to reduce the width of the footprint and shorten the cooled area, especially at higher blowing rates. In fact, increasing the hole length, suppressed the flow separation inside the diffuser part of the hole, thus degrading the lateral spreading of the coolant, and reducing the laterally averaged effectiveness. The authors stated that the operating conditions and the hole geometry are of major importance for an accurate assessment of the film cooling performance.

Colban et al. (2011) developed an empirical correlation for predicting film cooling performance on a flat plate downstream of a row of shaped holes. The correlation included the effects of the most relevant film cooling parameters which were identified as follows: the blowing ratio, distance downstream the cooling hole, hole length (L / D), injection angle (α), coverage ratio (W / P), hole exit to inlet area ratios (A_{exit} / A_{inlet}), and hole spacing (P / D). They found that increases in effectiveness are not proportional to increases in blowing ratio; in fact, the improvement is reduced at higher blowing rates. For shaped holes, the maximum effectiveness is usually located at the exit of the hole. The effectiveness was found to decay downstream of the hole at a rate that they were able to correlate. The hole length was observed to have negligible effect on the effectiveness, and was removed from the correlation.

On another note, as Nguyen et al. (2011) have mentioned, film cooling holes are manufactured by water jet, electro-discharge, or laser machining methods. Therefore, conical shaped holes are more easily obtained from a manufacturing standpoint than other shaped holes. However, both Nguyen et al. (2011) and Bunker (2005) agree that literature pertaining to conical shaped holes is limited, and the data available is focused solely on precisely-shaped holes, as opposed to holes obtained with actual manufacturing methods.

Cho et al. (2001) investigated the performance of a conical shaped hole that uses a diffusion angle of 4 degrees and another that uses a diffusion angle of 8 degrees but whose cone centerline is tilted by 4 degrees with respect to the cylindrical tube centerline. The authors compared the conically shaped holes performance to a cylindrical hole. The effect of compound angles of 0^o, 45^o, and 90^o, on all three hole designs was also tested. The conical shaped hole that is not tilted yielded the best cooling performance at all conditions. The compound angle allowed a more uniform enhanced heat transfer area. The conical shaped holes had reduced heat transfer coefficients in comparison to the cylindrical hole. The effect of conical shaped holes on film cooling performance was stronger at higher blowing ratios.

Nguyen et al. (2011) tested experimentally two conically shaped holes; one obtained with a diffusion angle of 3 degrees, and the other with 6 degrees, and compared the results to a cylindrical hole. The authors concluded that the discharge coefficients obtained with the conical shape are higher than cylindrical holes. The discharge coefficient was in fact found proportional to the diffusion angle. The authors also determined that conical shaped holes yield a better cooling performance than cylindrical holes at all blowing ratios. The uniformity of the cooled surface temperature was analyzed as well, and better coolant uniformity was obtained with conical shaped holes.

1.1.1. Summary

In summary, shaped holes have been known to outperform the standard cylindrical holes, as they allow more lateral spreading of the coolant, and avoid coolant lift-off by reducing the momentum of the coolant jet. The effect of a shaped hole is in fact stronger at higher blowing ratios. Shaped holes also result in less shear mixing of the coolant with the mainstream.

Research has focused on depicting the effects of the individual geometric parameters on film cooling performance. Increasing the injection angle was shown to shorten the cooled surface but widen the coolant footprint. At a small blowing ratio, a shallow injection angle provides superior performance, whereas at high blowing ratios a steep angle allows better film cooling effectiveness. The most common injection angle used in literature is 30^{o}. The addition of a compound angle to a shaped hole may increase or decrease the film cooling effectiveness depending on the operating conditions. The hole length was shown to have negligible effect on film cooling performance except at really high blowing ratios where an increase in hole length yields a reduced coolant footprint. It was also shown that the hole length can be used to suppress flow separation inside the diffuser part of the hole.

As for the expansion angles of a shaped hole, it has been shown that increasing the lateral expansion angle usually results in a wider lateral spreading. Low expansion angles prevent the coolant from lifting off the surface. Flow separation has been observed in the diffuser section of an overly expanded hole. The addition of a laidback expansion angle to a fanshaped hole has been shown to provide a better lateral spreading, thus reducing the wall heat transfer coefficient. It also suppresses the horseshoe vortex and flow separation that are usually observed at the exit of the cooling hole. However, a laidback angle can yield higher diffusion of the coolant with the mainstream and generate kidney vortices which could be detrimental to the film cooling

performance. The laidback fanshaped hole is the most popular in literature and that is due mostly to its outstanding performance compared to other shapes and to the fact that it is easier to manufacture a hole that is expanded in both directions as opposed to only one.

However, from a manufacturing standpoint, the conically flared hole remains the most easily realizable. Literature studies focusing on the conically flared holes are scarce. This instigates the need to conduct a fundamental analysis of the conically expanded hole and assess its impact on the cooling effectiveness and the aerodynamic loss.

1.2. Numerical modeling of film cooling

The turbine geometry and associated fluid dynamics and thermodynamics is complex, three-dimensional and unsteady, and has been shown to be difficult to simulate numerically. The first challenge when modeling film cooling on a three-dimensional airfoil is due to the difference in scale between the film hole and the airfoil geometry. The second major challenge is the absence of a turbulence model that can be applied to such type of flows characterized by high Reynolds number, high mainstream turbulence, and heat transfer. CFD computations of film cooling applications must predict near wall turbulence, transition, and jet in cross-flow/wall bounded shear layer interaction. The flow near the coolant injection locations is highly disturbed and strained.

The standard k-ε model Launder and Spalding (1974) is the most widely used turbulence model for high Reynolds number flows and is based on two transport equations, one for the turbulence kinetic energy, k, and the other for the dissipation rate, ε. The main drawback of this model is the anisotropy of turbulence assumption and its inaccuracy in predicting the coolant spreading rates. The RNG k-ε incorporates an additional term in the ε-equation for the interaction between the

turbulence dissipation and the mean shear. The model improves the prediction for high strain flows and high streamline curvature yet fails to predict the spreading of a round jet. The realizable k-ε model incorporates a new formulation for the turbulent viscosity and a new transport equation for the dissipation rate ε that uses the mean-square of vorticity fluctuations. This model improves the prediction of round jet spreading and resolves well boundary layers under adverse pressure gradients. The standard k-ω model performs better in transitional flows Wilcox (1994) as the main advantage behind its formulation is the near wall treatment for low turbulent Reynolds number computations. However, its main drawback is still the anisotropy of turbulence assumption and its high sensitivity to free-stream turbulence intensity. Finally, the SST model Menter (1994) combines the k-ε model to the k-ω model using blending functions. It also takes into account the transport of the principal turbulent shear stress and is shown to perform well under adverse pressure gradients and in separated flows.

Researchers have focused on assessing the many turbulence models that are available in predicting the cooling performance. However, no general consensus exists on the best turbulence model for film cooling applications as problems of this nature encompass a wide variety of crucial criteria (CFD domain size, surface curvature, hole shape, coolant flow conditions, mainstream flow conditions) to be accounted for when selecting a particular turbulence model. Researchers have also focused on correctly resolving the near hole flow field by using adequate mesh element clustering. The literature below is a chronological review of some of the effort that has been done in this field for accurately predicting the airfoil surface heat transfer coefficient and adiabatic film cooling effectiveness. The literature also demonstrates that there exist more studies evaluating turbulence models prediction of the adiabatic effectiveness on flat plates than

on airfoil surfaces. Most of the studies conducted on flat plates aim to reproduce the experimental data of Sinha et al. (1991).

1.2.1. The computational domain and grid

Choi (1993) demonstrated a first effort to include the injection cooling hole tube into the computational domain. He developed a Navier-Stokes solver to analyze a single row of film cooling holes on the suction surface of a research transonic turbine blade. The modified Coakley's q-ω model was used for turbulence closure. An O-mesh was wrapped around the airfoil, whereas an H-mesh was used outside of the O-mesh zone, upstream of the leading edge, and downstream of the trailing edge. It was ensured that the O-mesh grid lines were orthogonal to the airfoil surface. Local fine grid zones were used around the coolant hole and its downstream. The length of the coolant injection pipe was equal to 10 times the diameter of the coolant hole. This choice of length allowed a fully developed turbulent flow exiting the film hole. Heat transfer results on the suction surface showed agreement with the experimental data. The numerical model was able to capture the horseshoe vortex usually observed downstream of the film hole.

Hall et al. (1994) attempted to determine the mesh characteristics for aerodynamic and heat transfer prediction on the surface of the C3X turbine vane cascade with leading edge shower head cooling holes. The numerical analysis aimed to solve the three-dimensional Navier Stokes equations using the Baldwin-Lomax algebraic turbulence model. It was observed that both streamwise and spanwise mesh resolutions are required. Additionally, mesh resolution normal to the airfoil surface is required for accurate prediction of film cooled airfoil heat transfer. The cooling hole tubes were not included in the numerical model, instead, the coolant hole meshes were aligned with the coolant injection angle to reduce the computational cost. The authors

recognized that grid generation in the case of airfoil cooling is a tedious and difficult task. Further CFD investigations were presented by Leylek and Zerkle (1994) who used the standard k-ε model for turbulence closure and a wall function treatment. Their numerical work aimed to describe the complex three-dimensional nature of the flow within the cooling hole. The results showed that the final distribution of dependent flow variables at the coolant exit plane results from the interaction of the counter-rotating structure and local jetting effects within the cooling hole, and the mainstream flow blockage. It was found that the shear layer above the coolant jet in the mainstream was the main source of turbulence at low blowing ratios, whereas at higher blowing ratios, turbulence emanated from the shear layer between the vortices and jetting regions within the cooling holes. The authors highly emphasized the importance of coupling the plenum, film hole, and mainstream flows into one numerical model.

Garg and Gaugler (1996a) conducted three-dimensional numerical flow simulations on the VKI blade of Camci (1985) to study the effect of coolant temperature, and coolant to mainstream mass flow ratio on the adiabatic effectiveness. They used the Baldwin Lomax algebraic turbulence model that is suitable for wall bounded turbulent shear layers but not appropriate for separating flows. However, unlike Choi (1993) and Leylek and Zerkle (1994), their computational model did not include the injection pipe nor the plenum. In fact, velocity and temperature profiles were specified at the exit of the holes as boundary conditions to avoid modeling the plenum and tube. They compared predictions of the blade surface heat transfer coefficient with experimental data and fair agreement was found between the two. The CFD considerably under-predicted the heat transfer especially near the film cooling holes. The adiabatic film cooling effectiveness was also simulated and found to be lower at a higher coolant to mainstream temperature ratio. It was noted that the adiabatic effectiveness is three-

dimensional and care should be taken when considering a laterally-averaged value. The authors performed several subsequent studies in which they analyzed the effect on cooling performance of several other parameters such as the spanwise pitch of the cooling holes, Garg and Gaugler (1996b), the blade rotation, Garg and Abhari (1997), and the turbulence modeling, Garg and Ameri (1997). The coolant velocity and temperature distribution were found to be the most influential parameters on the blade surface heat transfer.

Garg (2001) also conducted numerical investigations of the VKI blade with showerhead holes using the Wilcox k-ω turbulence model. The $1/7^{th}$ power law profile for coolant velocity and temperature was imposed at the exit of the shower head holes. Comparisons of the local and spanwise averaged heat transfer coefficient to the experimental values revealed that the flow does not follow the $1/7^{th}$ power law profile. However, it was noted that the power law profile did yield reasonable predictions of the spanwise averaged heat transfer coefficient. It was concluded that further experimental spatially resolved data is required for accurate validation of the numerical model.

In subsequent studies, the authors, Garg (2001), extended the CFD domain to include the plenum and hole pipes. They also employed the Wilcox's low Reynolds k-ω model instead of Baldwin Lomax. The numerical results obtained were in much better agreement with the experimental data than previous studies. The computations revealed that the flow physics and mechanisms occurring inside the plenum and cooling pipes are of major importance for correct resolution of blade surface heat transfer. Studying the distribution of main flow variables at the exit of the cooling holes showed that both coolant and velocity temperatures do not follow the $1/7^{th}$ power law profiles. A vortical structure was identified near the blade surface and it was found that a low Reynolds turbulence model is required to correctly resolve the near field flow.

1.2.2. Turbulence modeling and cooling effectiveness prediction

Most of the investigations were conducted on flat plates. However, recently, more airfoil studies began emerging. Typically, literature investigations assessed the cooling performance by measuring the laterally-averaged adiabatic effectiveness distribution downstream the cooling holes. The literature that is presented below indicates that an accurate prediction of the effectiveness distribution on airfoil surfaces remains challenging.

i. Flat plate investigations

Amer et al. (1992) conducted a numerical investigation to assess the accuracy of four different turbulence models in predicting film cooling effectiveness downstream two rows of standard cylindrical holes on a flat plate. Their numerical predictions were compared against experimental data. The turbulence models investigated consisted of the standard k-ε, a modified version of it by Bergeles to account for the anisotropic effect, the standard k-ω, and its modified version by Ilegbusi and Spalding. It was found that the success of all turbulence models in predicting the cooling effectiveness depends highly on the blowing ratio. No specific turbulence model was found fit to be generalized to all blowing ratios. It was also suggested that two-equation turbulence models do not work well for film cooling, especially in the near-hole field and at high blowing ratios. This was attributed to the fact that neither the shape nor the magnitude of the velocity profiles were predicted properly and the flow near the hole was referred to as disturbed and unsteady.

Sarkar and Bose (1995) also conducted a comparative investigation involving the low-Reynolds number versions of the k-ε and k-ω models, Baldwin Lomax, and a relaxation eddy viscosity model on a flat plate with a slot. The low-Reynolds k-ε model was found preferable for the selected application. The k-ω model performed the worst in capturing the surface temperature

distribution. It was also found that the relaxation model predicts the maximum separation, whereas k-ω predicts the minimum separation length. Results confirmed that the shear layer between the mainstream and the coolant flows is the main source of turbulence generation.

Ferguson et al. (1998) compared the performance of three different turbulence models combined with three different wall treatments in simulating film cooling flow on a flat plate against an experimental database. It was found that the standard k-ε turbulence model was best in predicting the trend in effectiveness in the near field region and the turbulence levels within the cooling hole. The two layer wall treatment was found to be essential in capturing the separation bubble that is present when the coolant lifts-off the flat plate surface and then reattaches to it.

Yavuzkurt and Hassan (2007) evaluated four turbulence models available in the commercial CFD solver FLUENT in predicting film cooling performance. One row of cylindrical cooling holes on a flat plate was considered. When high mainstream turbulence levels were applied at low blowing ratios, the standard k-ε model yielded the best effectiveness predictions. The RNG and realizable k-ε models yielded similar results but deviated from the experimental data by up to 60%; the trend of the data was not matched at all. The standard k-ω model, consistently under-predicted the cooling performance and deviated from the data by up to 70%. When higher blowing ratios were applied, all models failed to predict the cooling performance correctly and up to 200% deviation from the experimental data was recorded for the standard k-ω and k-ε models. The deviations were attributed to the limitations of the Boussinesq hypothesis which relates the direction of the Reynolds stresses to that of the strain rates.

Harrison and Bogard (2008) also investigated turbulence models performance in predicting cooling flow behavior on a flat plate. They analyzed the standard k-ω model, the realizable k-ε,

and the RSM model. Their investigations revealed that the standard k-ω predicted best the laterally averaged adiabatic effectiveness, and the realizable k-ε predicted best the centerline adiabatic effectiveness. All models predicted poorly the lateral spreading of the coolant. Even, the anisotropic RSM model did not show any improvements in the prediction of the spreading of the coolant. As for the heat transfer coefficient, all three turbulence models were able to yield agreeable predictions of laterally averaged normalized heat transfer coefficient distributions. The authors concluded that the best turbulence model must be determined based on the application that is being considered.

Silieti et al. (2009b) conducted a comparative numerical investigation involving the SST model, the v^2-f model, and the realizable k-ε model to predict film cooling effectiveness from a fan-shaped hole on a flat plate. Three topology grids were investigated: one using solely hexahedral elements, another with only tetrahedral elements, and a final one that was hybrid. Both conjugate heat transfer and adiabatic simulations were conducted. The numerical results were compared to experimental data. The predictions obtained with the hybrid mesh were identical to those obtained with a hexahedral mesh, indicating that the boundary layer has to be resolved for accurate prediction of the temperature field. It was concluded that the realizable k-ε model performs better than the v^2-f model in predicting the surface temperature distribution. The flow distribution with the SST model was similar to that of the realizable k-ε. The conjugate heat transfer model predicted a significant difference in the temperature fields. The authors concluded that modeling heat conduction through the metal is crucial for accurate depiction of the wall temperature.

Silieti et al. (2009a) investigated film cooling effectiveness for one and two cooling slots on a flat plate using both conjugate heat transfer and adiabatic simulations. Five different turbulence

models were examined; the RNG k-ε, realizable RSM k-ε, k-ω, and SST. It was found that modeling conjugate heat transfer influences greatly the predictions of film cooling effectiveness. The RNG k-ε, realizable k-ε, and RSM yielded almost the same results with slight deviations. The two versions of the k-ω model under-predicted the flow field and over-predicted the temperature field. The reattachment points inside the cooling hole and outside on the flat plate were very different. The SST model predicted a reattachment point that was twice the distance downstream the RNG and the realizable k-ε reattachment points.

Yao and Yao (2011) conducted Reynolds averaged Navier Stokes computations for four different cooling hole geometries; namely, the cylindrical hole, the cylindrical hole with an upstream wedge, the fan-shaped cooling hole, and a double console slot. The investigation was carried out on a flat plate. Numerical predictions were compared against the experimental data of Sinha et al. (1991). The numerical computations were carried out using the RNG k-ε turbulence model. The clustering of hexahedral elements near the wall yielded a y^+ of about 7. A velocity boundary condition is applied at the inlet of the plenum yielding a blowing ratio of unity. This was maintained for all cooling hole geometries. Numerical predictions of the center-line adiabatic cooling effectiveness were about 50% higher than the experimental data in the near hole field. Predictions improved further downstream but still over-predicted the cooling performance. The authors attributed this discrepancy to an inaccurate prediction of the penetration depth of the coolant jet into the mainstream flow. The significant improvements that were observed for the fan-shaped and double console slot with respect to the cylindrical hole were attributed to the weakening of the vortex structures in the near-hole field and the consequent reduction of hot mainstream entrainment. The diffuser of the fanshaped hole slows down the coolant flow and

forces it to remain attached along the way up to the hole exit and beyond. This yields a prolonged cooling coverage in the streamwise direction.

ii. Airfoil investigations

Medic and Durbin (2002b), Medic and Durbin (2002a), conducted three-dimensional CFD simulations of the VKI blade of Camci and Arts (1985). They focused on two of Camci and Arts film cooling cases, the first consists of two rows of staggered axial holes on the suction side, and the second consists of one row on the pressure side. They compared results of the standard k-ε, k-ω, and v^2-f turbulence models to the experimental data with and without film cooling. The computational domain consisted of one film hole, tube, plenum, and airfoil. Four non-matching mesh blocks were generated for the plenum, the cooling tubes, holes, and the rest of the geometry. The plenum pressure was adjusted iteratively to match the experimental blowing ratio. It was found that two equation turbulence models, namely the k-ε and k-ω models, yield unreasonable predictions of blade surface heat transfer coefficient. The substantial over-prediction of heat transfer coefficient on the suction surface and near the stagnation region was attributed to "the stagnation point anomaly" that was identified by Durbin (1996). An anomalous production of turbulent kinetic energy occurs in regions of large strain rate. Predictions of the heat transfer coefficient were majorly improved by imposing time scale bounds to the models. The k-ε model with the time scale bound and the v^2-f model gave heat transfer results that agreed well with experiments except at high blowing ratios. On the pressure side however, the k-ε with the time scale yielded in very good agreement with experiments but the v^2-f model over predicted the lateral spreading of the coolant.

Walters and Leylek (2002) validated the use of the realizable k-ε model, in combination with a two-layer near wall treatment for the study of film cooling on a linear turbine cascade. Their

simulation modeled a single row of streamwise-injected film holes on the pressure and suction surfaces of an airfoil. The CFD domain consisted of the airfoil passage, the plenum and the film hole. For simplicity, only half of the hole to hole pitch was modeled. Symmetry planes were applied at the center of the hole and at the mid distance between the holes. CFD results were compared against experimental data. The data analyzed included the laterally averaged adiabatic effectiveness and the local effectiveness. Agreement was found best between experimental and numerical data at low blowing ratios (namely BR = 0.5). It became progressively worse as the blowing ratio increased (BR = 2). Their study indicated that numerical computations can accurately resolve the physical mechanisms in the mean flow. However, two-equation eddy viscosity turbulence models fail to predict the correct heat transfer magnitudes. In a subsequent paper Walter and Leylek (2002), the authors analyzed the turbulence models deficiencies responsible for the discrepancies between numerical and experimental data. It was observed that numerical simulations over-predicted the adiabatic effectiveness but always represented the correct trend which indicates a good resolution of the mean flow mechanisms. Although, the realizable k-ε model was found most appropriate for predicting the cooling performance, however it was not diffusive enough and was deficient in reproducing the turbulent mixing that occurs close to the surface in the near field. It is a two-equation isotropic turbulence models and tends to under-predict the lateral spreading rate of the coolant. It lacks history effects on Reynolds stresses and is insensitive to streamline curvature.

York and Leylek (2002) validated the use of the realizable k-ε model and a two layer near wall treatment for prediction of surface effectiveness in the stagnation region of a leading edge film cooled blade. Their simulation modeled a turbine blade of an elliptical leading edge with three staggered rows of cylindrical cooling holes. For simplicity, a symmetry plane was applied at the

center of the stagnation row of holes. And periodic planes were applied halfway between the centers of two adjacent holes. All holes had the same uniform velocity profile. Walls were assumed to be adiabatic. An unstructured multi topology grid was used. FLUENT was used to perform the CFD simulations. The predicted adiabatic effectiveness was compared against experimental data. Good agreement in trend was observed between the numerical and experimental distribution of effectiveness in the streamwise direction. But the spanwise averaged effectiveness was consistently over predicted. Predictions of the spanwise averaged effectiveness progressively worsened as the BR increased (BR = 2.5).

Charbonnier et al. (2008) compared and assessed two different commercial CFD software, CFX and FLUENT, using experimental measurements of heat flux and adiabatic film cooling effectiveness on a film cooled nozzle guide vane. The authors used the same unstructured mesh and boundary conditions with both CFD codes. The computational domain included the plenum, the cooling holes, and the mainstream flow. Both software solutions showed good agreement with the experimental data. The authors also tested several turbulence models with and without transition. They noted that the SST model yielded the best agreement with the experimental data. The authors concluded that even though the two commercial CFD codes belong to the same software vendor, ANSYS, and use the same turbulence models, they use different methodologies for convergence and hence yield similar but not identical results. They also confirmed that resolving the coolant flow structure in the plenum is extremely important as it significantly affects the numerical results.

Nadali et al. (2012) assessed the accuracy of the Spalart-Allmaras, the realizable k-ε, and the SST models in predicting the film cooling performance of cylindrical and fan-shaped cooling holes on a gas turbine vane. The analysis was conducted for a blowing ratio ranging from 0.2 to 1.8. Wall

treatment was implemented as a y^+ value below unity was used. Both the realizable k-ε, and the SST models over-predicted the spanwise averaged film cooling effectiveness by about 50%, especially in the near hole field. The Spalart-Allmaras agreed very well with the experimental data. The latter was therefore chosen to analyze the effect of blowing ratio, hole position, and hole shape on the cooling performance. It was found that fan-shaped holes could experience severe lift-off for blowing ratio exceeding unity depending on the local airfoil curvature. Furthermore, the hole position had negligible effect on the cooling performance of pressure surface holes.

1.2.3. Summary

In summary, literature indicates that recent film cooling research has been moving away from flat plates and toward airfoil geometries. That is because the coolant jet exiting the film cooling hole of an airfoil is subjected to streamline curvature and pressure gradients that are not existent on a flat plate. The film cooling performance is influenced by the penetration of the coolant into the hot mainstream, the secondary flow structures formations, and the turbulent mixing. Thermal analysis on film cooled turbine airfoils is usually presented in terms of the adiabatic film cooled effectiveness and the heat transfer coefficient distributions on the surface.

Traditionally, heat transfer modeling of film cooled turbine airfoils has been done by decoupling the external flow, internal flow, and film cooling holes. Recently efforts have been employed to combine the internal flow, external flow, and film cooling holes into one computational model for a multiple-row film-cooled airfoil.

Additionally, literature has shown that only hexahedral meshes are able to correctly resolve the flow in the near-hole region. In fact, hexahedral elements are better aligned with the mainstream

and cooling flow and an appropriate clustering of elements near the wall permits a larger number of elements inside the boundary layer.

On another note, current computational resources still require the use of periodic interfaces at the centers of film cooling holes and halfway between adjacent airfoils to simulate an infinite-span cascade with infinite rows of film cooling holes.

Literature indicates that film cooling flow can be accurately predicted in the far-field, but the near hole region is always difficult to resolve, especially in the case of coolant lift-off, meaning when the coolant flow mixes with the mainstream flow and separates from the cooled surface. Furthermore, it is widely agreed on that the success of a numerical solution is highly influenced by the choice of the turbulence model and wall treatment. The above literature review indicates that eddy viscosity models tend to under-predict the spanwise spreading of film coolant; and the discrepancies between predictions and experimental data usually increases with increasing blowing ratio. This signifies that difficulties still arise when jet lift-off occurs.

It has been broadly shown in literature that a turbine airfoil's external heat transfer coefficient is very difficult to predict numerically as it is mainly dependent on near wall viscous flow effects. The wall heat transfer coefficient is in fact linked to molecular diffusion, turbulent convection, and turbulent shear stress transport. Numerical studies have shown that the heat transfer coefficient is usually under predicted near the film cooling hole. The adiabatic cooling effectiveness on the other hand is predicted with adiabatic wall CFD simulations and is dependent on the adiabatic wall temperature. Most literature has shown that k-ω based models predicted best the spanwise averaged adiabatic effectiveness, and the k-ε based models predicted

best the centerline adiabatic effectiveness. However, no general consensus exists on the best turbulence model to be used in film cooling applications.

1.3. Effect of film cooling on aerodynamic loss

Although film cooling has received much attention to date, little is known about its impact on the turbine aerodynamics. The following is a chronological review of the studies conducted to quantify the aerodynamic penalty due to film cooling.

Hartsel (1972) introduced a one-dimensional mixing layer model for aerodynamic loss prediction in which only part of the coolant mixes with the boundary layer at the coolant injection position. The model assumes that cooling losses resulting from the mixing of the coolant with the mainstream flow can be superimposed on boundary layer losses such as those caused by viscous effects and trailing-edge blockage. Each of these losses can be determined separately and then added up to yield the total pressure loss of a cooled turbine cascade. The ideal exit kinetic energy was defined as the sum of the ideal kinetic energy of the mainstream and that of the coolant as they expand separately and isentropically to the exit static pressure. Numerical predictions of Hartsel's model were compared against experimental data and good agreement was found. The results showed that film cooling effects on the aerodynamic loss are highly dependent on the mainstream Mach number, the coolant blowing ratio, the injection angle, and the ratios of coolant to mainstream total temperature and velocity. It was found that losses decrease with decreasing injection angle.

Walter and Leylek (2000) investigated numerically the impact of film cooling on the aerodynamic loss. They attempted to prove that CFD simulations can be used consistently to accurately predict the impact of film cooling on blade aerodynamics. They analyzed a row of

cylindrical cooling holes on a blade suction surface. They implemented several variations of the *k-ε* turbulence model and demonstrated that proper turbulence modeling is crucial for aerodynamic loss prediction. The aerodynamic loss was reported in terms of the total pressure loss downstream of the blade row at a single spanwise location, downstream of one of the film hole centers. They found that the realizable *k-ε* model showed the best agreement with the experimental data. They also showed that film cooling can impact the aerodynamic loss through two separate mechanisms: the mixing of the coolant injected with the mainstream and the increase of drag on the airfoil.

Similarly, Jackson et al. (2000) investigated experimentally the effects of suction surface film cooling on the turbine aerodynamic loss in transonic flow. They used symmetric turbine airfoils and two different film cooling hole configurations, cylindrical and conically flared. The aerodynamic penalty was quantified using profiles of total pressure losses and normalized exit kinetic energy, measured one chord downstream of the trailing edge of the blade. Experiments with no film cooling yielded the lowest total pressure loss. It was found that film cooling may reduce the strength of the shock waves with increasing blowing ratio when conically expanded holes are used. The integrated aerodynamic loss was determined by integrating profiles of $\left(p_{0\infty e} - p_{0e}\right)$ with respect to *y,* the vertical direction, one chord downstream. These profiles excluded pressure losses resulting from oblique shockwaves. It was found that the integrated aerodynamic loss is higher with film cooling than without, and that the aerodynamic loss due to the mixing occurring between coolant and mainstream flows is higher than that resulting from the oblique shock waves. It was also found that the integrated aerodynamic loss is strongly dependent on the film hole geometry, as it was much lower for conically flared film holes than for cylindrical holes (about three times lower loss for the conical hole).

Bunker (2005) provided a concise summary of the effects on aerodynamics that demonstrates the complexity of such phenomenon. He stated that at forward portions of vanes where the local Mach number is low, shaped holes may lower the coolant momentum, and allow reductions in the aerodynamic loss in comparison to cylindrical holes. On the other hand, when the local Mach number is high expanded hole exits can increase the aerodynamic loss.

Young and Horlock (2006) provided a critical review of the different methods of estimating the aerodynamic efficiency of cooled cascades and turbine stages. They indicated that the main issue is the definition of the ideal gross power output that is used in the denominator of the efficiency expression. The first step in their analysis consisted in reviewing the efficiency definition of Hartsel (1972). It assumed that the coolant and mainstream flows expand separately. This methodology was shown to be unsatisfactory as the Hartsel efficiency exceeded unity when the gases have different but constant values of c_p and γ. The authors deduced that the ideal process should be defined as a mixed expansion of coolant and mainstream flows. Three different methodologies were developed and analyzed. The first one was named the mainstream pressure efficiency and its ideal process is based on the assumption that coolant and mainstream flows mix to result in a fixed mainstream pressure then expand to the exit conditions. Turbine manufacturers may be drawn to the weighed pressure turbine efficiency, in which the ideal gross power output includes the entropy generation associated with the equilibration of coolant and mainstream static temperatures. However, the authors argue that a cooled efficiency in which the p_{ideal} is based on a fully reversible adiabatic process has the soundest thermodynamics foundation but yields efficiency values that are lower than the ones obtained with the Hartsel efficiency.

Chappell et al. (2010) studied the performance of film cooling on the suction surface gill region of a turbine vane using a transonic wind tunnel. They investigated local distributions of total

pressure loss coefficient, local normalized exit Mach number, local normalized exit kinetic energy, and integrated aerodynamic losses. Profiles of total pressure loss coefficients were measured at a location of 0.25 axial chord downstream of the vane trailing edge. The integrated aerodynamic loss was found by integrating profiles of $(p_{0in} - p_{0e})$ with respect to *y,* the vertical direction across the wake, for one vane spacing. They recorded a general trend of increasing integrated aerodynamic loss with increasing blowing ratio and with increasing the number of rows of holes. Computed integrated aerodynamic loss values were compared to the one-dimensional mixing loss equation given by Denton (1993) and good agreement was found between the two. The authors also studied four different hole geometries: round axial, shaped axial, round radial, and round compound. They demonstrated that round axial holes yielded the lowest integrated aerodynamic loss magnitudes at a particular blowing ratio. The shaped axial holes yielded the highest peak in total pressure loss coefficient.

1.3.1. Summary

The analysis of the effects of film cooling on turbine aerodynamics brings about the main question of how the boundary layer is affected when coolant flow is injected into it. During the mixing process, entropy generation results from the heat transfer process between the coolant and mainstream flows due to the difference in their static temperatures. It also results from the viscous dissipation that occurs because of the difference in their velocities.

Available studies in literature that analyzed the effect of film cooling on aerodynamics are scarce. The studies quantified this effect by computing the total pressure loss downstream of the airfoil, the normalized exit kinetic energy, and the integrated aerodynamic loss. Such investigations brought about the conclusion that aerodynamic loss is higher with film cooling than without. It was also found that the aerodynamic loss is highly dependent on mainstream

flow condition, and on hole geometry. Specific trends in the variation of the aerodynamic loss with respect to such flow and geometric variables have not been established. This demonstrates the need to conduct a fundamental analysis for the variation of the aerodynamic loss with respect to film cooling parameters.

1.4. Numerical optimization

CFD based optimization techniques can be accomplished by coupling a CFD solver with an optimization algorithm. Genetic algorithms are widely used to ensure reaching a global minima or maxima of the design objective function. To reduce computation time, response surface approximation techniques, mostly of the artificial neural network (ANN) type, can be used to approximate the objective function over the design space. The ANN can be constructed using two sets of CFD simulations, one for training and the other for testing the ANN. Many airfoil shape optimization studies have been implemented to reduce the aerodynamic loss and increase the aerodynamic efficiency. One study is available in literature where the shape of the film cooling hole was optimized to increase the film cooling effectiveness and reduce the aerodynamic loss.

The following is a chronological review of all shape optimization studies that aimed to either increase the aerodynamic efficiency by optimizing the airfoil shape, or to increase film cooling effectiveness by optimizing the cooling hole shape.

1.4.1. Aerodynamic shape optimization

Dennis et al. (1999) demonstrated the applicability of combining the genetic algorithm with a sequential quadratic programming (SQP) algorithm to optimize the aerodynamic shape of a two-dimensional airfoil cascade. The optimization aimed to minimize the entropy generation. The

airfoil profile was parameterized using conic section parameters and B-spline curves. The parameters defining the airfoil profile were chosen as design variables. The SQP was used to enforce the design constraints for cross sectional area and thickness distribution. Penalty terms were added to the optimization objective function to enforce the remaining design constraints, namely, the lift, mass flow rate, and flow angles. The optimization procedure was coupled with a two-dimensional k-ε based Navier Stokes flow solver. It required 220 to 675 calls to the flow solver.

Wang and Damodaran (2001) successfully implemented the Simulated Annealing algorithm on multiple processors to optimize several aerodynamic shapes of internal flow systems (nozzles and diffusers). The algorithm was coupled with two-dimensional Euler/Navier-Stokes solver to evaluate the design objective functions. The authors focused on examining efficiency and speedup of the parallel algorithm. They compared the variation of wall-clock time with the number of processors. They found that an optimal number of processors exists to maintain the speedup as well as the efficiency of the algorithm. It was also found increasing number of design variables required increasing number of processors to reduce wall clock time.

Oyama et al. (2004) successfully optimized the aerodynamic shape of a compressor blade known as the NASA rotor67. They used a real-coded genetic algorithm coupled with a three-dimensional Navier-Stokes solver. The optimization aimed to minimize the objective function that was defined as the entropy production. The blade shape was described using four blade profiles at different spanwise locations. The blade profiles were defined by their camber line and thickness distribution. They were represented by B-spline curves of the third order. The coordinates of the control points of the B-spline curves were chosen as design variables. The objective function was penalized with design constraints, namely the mass flow rate and the

pressure ratio. The initial population of design candidates was selected by random sampling from the design space. The optimization procedure successfully yielded an optimum three-dimensional blade design that reduced the entropy production by 19%.

Mengistu and Ghaly (2003) successfully demonstrated the applicability of the genetic algorithm and simulated annealing to optimize the aerodynamic shape of a transonic turbine cascade. The optimization aimed to minimize the objective function that was defined as the total pressure loss. The blade profile was defined by its camber line and thickness distribution. The camber line was represented by a Non-Uniform Rational B-Splines or NURBS curve. The curves consisted of 7 to 11 control points. The y coordinates of the NURBS control points and weights were chosen as design variables. The constraints consisted of the inlet and exit flow angles, the mass flow rate through the blade passage, the blade pitch, and the thickness distribution. Two-dimensional numerical simulations were performed using an Euler solver. 180 calls to the CFD solver were required for the genetic algorithm optimization. The optimization eliminated the shock through a relatively small number of objective function evaluations. It was found that the genetic algorithm was best suited for cases with large number of design variables, whereas the simulated annealing was more appropriate for a smaller number of design variables.

In a subsequent research, Mengistu and Ghaly (2004) used the genetic algorithm and the simulated annealing to optimize a NACA 65 subsonic axial compressor. They successfully coupled the algorithms with an artificial neural network (ANN) that was trained and tested with a two-dimensional RANS solver. The objective function was chosen to be the aerodynamic efficiency. Similarly to their previous research, the blade profiles were parameterized using NURBS curves. 35 blade profiles were employed to train the ANN and 15 to test it. 200 CFD simulations at both design and off-design operating conditions were required. It was found that

the use of ANN reduced the computation time by ten. The optimization scheme was successful and resulted in an optimal profile that yielded 4% gain in adiabatic efficiency. Their work was validated as it compared well with that of Oyama et al. (2004).

Arabnia and Ghaly (2009) successfully applied an optimization strategy to redesign a turbine stage. Single and multipoint optimizations were carried out using the genetic algorithm coupled with ANN. The design variable was the stacking line of the blade and the vane. The stacking line was represented by a quadratic rational Bezier curve (QRBC), and its parameters were the lean, sweep, and bow. The objective function was a weighed sum of individual objectives and was penalized with design constraints. Individual objectives included turbine efficiency, total pressure loss, tip clearance loss, secondary loss, and shock loss. The design constraints included the mass flow rate, which implies a fixed rotor speed, and fixed inlet and exit boundary conditions. The ANN was tested and trained using a database of CFD simulations performed with the commercial software FLUENT. The QRBC parameters were selected using the Latin Hypercube Sampling method. The optimum blade shape corresponding to single point optimization is different from the one obtained with multi-point optimization. The aerodynamic efficiency improved by 0.4% with single point and 0.6% with multi-point optimization. This improvement was attributed to a reduction of the three dimensional flow effects compared to the reference geometry.

1.4.2. Film cooling optimization

Lee and Kim (2009) performed the first optimization of a cylindrical film cooling hole geometrical shape on a flat plate. The optimization was performed at an optimum blowing ratio of 0.65, which was determined for the reference geometry. The spatially averaged film cooling effectiveness was chosen as the objective function. Two design variables were selected, namely,

the ratio of length to diameter of the hole (L/D) and the ejection angle (α). Twelve experimental points were selected in the design space using the Latin Hypercube Sampling algorithm. The cooling effectiveness was resolved for those experimental points by Reynolds Average Navier Stokes (RANS) simulations, and the SST model was used for turbulence closure. The authors conducted the optimization using a gradient based search algorithm (Sequential Quadratic Programming algorithm or SQP) coupled with different types of weighted average surrogate models. It was found that the Kriging surrogate model predicted the optimum design that yielded the highest spatially-averaged film cooling effectiveness (3.6% improvement from baseline design) as indicated by RANS simulations.

In a subsequent study Lee and Kim (2010), they successfully demonstrated the use of a weighted average surrogate model coupled with the SQP algorithm to optimize a fan-shaped film cooling hole on a flat plate. The weighted average surrogate model was defined as the weighted sum of three different basic surrogates, which are the response surface approximation, Kriging, and radial basis neural network. The objective function was the spatially averaged film cooling effectiveness. The injection angle (α), lateral expansion angle (β), and length to diameter ratio (L / D) of the hole were chosen as design variables. Twenty experimental points were selected with Latin Hypercube Sampling algorithm to train the surrogate model. RANS simulations were performed to resolve the spatially averaged effectiveness using the commercial software CFX v.11.0. The SST model was used for turbulence closure. For a blowing ratio of 0.5 the optimization algorithm yielded an optimized shape that increased the objective function by 28% from the reference geometry. This study was followed with the optimization of a laidback fan-shaped hole on a flat plate Lee and Kim (2011). This time four design variables were used for the optimization. Those were the injection angle (α), lateral expansion angle (β), length to diameter

ratio (L / D), and the forward expansion angle (Υ) of the hole. The objective function was once again the spatially averaged adiabatic film cooling effectiveness. The surrogate model chosen was the Kriging model. RANS simulations were conducted with the SST turbulence model as well. The optimization was performed for blowing ratios of 0.25 and 0.5, and the optimum hole shapes obtained improved the objective function by 44.9% and 31.8% respectively.

Subsequently, Lee et al. (2010) proposed a novel shaped film-cooling hole which they optimized using the same methodology as in their previous studies. The radial basis neural network was coupled with the sequential quadratic programming algorithm. The design variables were four and consisted of the ratio of pitch to diameter of the hole (P / D), the lateral expansion angle (β), the forward expansion angle (Υ), and the length to diameter ratio of the hole (L / D). The optimization objective was the spatially averaged cooling effectiveness once again, however, this time it was normalized by the pitch to diameter ratio of the hole. The optimized geometry improved the objective function by 18.1%. The novel shaped film cooling hole was analyzed using RANS simulations with the SST turbulence model as was done previously. Its cooling performance was compared against that of the fan-shaped, the laidback fan-shaped, and the dumbbell shaped holes.

Finally, Lee et al. (2011) took into account the aerodynamic penalty in their optimization work. They implemented a multiple objective optimization of a laidback fan-shaped hole on a flat plate. Two objective functions were constructed, one for the spatially averaged adiabatic film cooling effectiveness, and the other for the aerodynamic loss. Four geometric design variables were selected namely, the injection angle (α), lateral expansion angle (β), forward expansion angle (Υ), and the ratio of pitch to diameter between the holes (P / D). 40 design points were selected with the LHS algorithm, and computation of the objective functions for the 40 design

cases, were conducted using the commercial software CFX. Once again, they employed SST model for turbulence closure. Kriging model was used for prediction of the objective functions during the optimization, and the global Pareto optimal solutions were obtained.

Recently, Lee et al. (2013) applied their multiple objective shape optimization technique to a row of laidback fan-shaped film cooling holes. Once again an evolutionary optimization algorithm was used in combination with the sequential quadratic programming technique. The design variables consisted of the injection angle (α), lateral expansion angle (β), forward expansion angle (Υ), and the ratio of pitch to diameter between the holes (P / D). Latin hypercube sampling yielded 40 experimental design candidates used to construct the surrogate model. The same two objective functions were used. The optimization yielded the Pareto front of optimal solutions. The authors concluded that, generally, a decrease in the injection angle, the lateral expansion angle, the pitch to diameter ratio and an increase in the forward expansion angle yields an increase in the film cooling effectiveness and a decrease in the associated aerodynamic penalty.

1.4.3. Summary

Literature review has shown that the automated shape optimization techniques rely on the coupling of three fundamental processes: a numerical optimization algorithm, a response surface approximation, and a CFD solver. Typically, the genetic algorithm is coupled with an artificial neural network to reduce the computation time by reducing the number of calls from the genetic algorithm to the CFD code.

The objective for aerodynamic design optimization is usually chosen to either minimize the total pressure loss, or maximize the efficiency. The objective function for film cooling performance

optimization is usually defined as the laterally (spanwise) or spatially averaged adiabatic film cooling effectiveness.

Previous work has shown that it is good practice to keep the number of design variables to a minimum. The appropriate formulation of the objective function is a fundamental ingredient to a successful optimization work.

1.5. Motivations and objectives of the present work

The above literature review indicates the need to conduct a fundamental investigation of the three-way relationship between the film cooling governing parameters, the cooling performance, and the aerodynamic loss. Generally, turbine engine manufacturers have been opting for a higher cooling performance instead of a higher aerodynamic efficiency to ensure the required engine life-time. Furthermore, the impact of high cooling effectiveness on the aerodynamic loss is usually neglected when investigating film cooling holes, and the sensitivity of the aerodynamic loss to the coolant flow parameters and cooling hole geometry is not accounted for.

Additionally, film cooling research seems to lack established design trends for film cooling schemes that provide a superior cooling performance while minimizing the aerodynamic penalty. On another note, novel cooling schemes are mostly finite shaped and are expensive to manufacture. There is a need for discrete film cooling research that takes into account machining costs and limitations.

There are three other motivations for this research besides the need for a film cooling design with high aero-thermal performance. Firstly, film cooling automated optimization is somewhat non-existent compared to aerodynamic shape optimizations. The second motivation emanates from the current computing capacities that have turned simulation-based automated optimization tasks

into a realizable task. The final motivation is the fact that engine manufacturers strive to reduce the design cycle time while enforcing more design constraints than before. This can be accomplished by using an optimization algorithm that could sweep the design space entirely, allowing designers to focus on the study of the resulting optimum design instead of manually exploring the design space.

There are two types of film cooling parameters that govern the cooling performance of film holes and the corresponding aerodynamic penalty: flow parameters and geometric parameters. The coolant flow parameters are the mass flux ratio and the density ratio between the coolant flow and the mainstream. The geometric parameters allow an accurate definition of a cooling hole shape. They mainly include the hole exit expansion angle (β), the hole tube inclination angle (α), the lateral injection angle (compound angle, CA), and the hole tube length (L / D). Literature has shown that a laidback fanshaped hole provides a superior cooling performance whereas it could either increase or decrease the aerodynamic penalty. On the other hand, a conically flared hole is easiest to manufacture. However, investigations of the effects of the conically flared geometry on the cooling performance and the aerodynamic loss are not common in literature.

The above demonstrates the need for the present research, which aims to determine effective film cooling hole design guidelines for achieving a superior cooling performance and a minimum aerodynamic loss, while taking into account machining limitations. The present problem is related to two competing objectives. In fact, the improvement of one objective, the cooling performance, results in the deterioration of the other objective, the aerodynamic efficiency, and vice-versa.

The objectives of the present research are summarized as follows:

- Conduct a fundamental investigation of the effects of film-coolant flow parameters on the cooling performance and the aerodynamic loss.
- Conduct a fundamental investigation of the effects of the conical hole geometry on the cooling performance and the aerodynamic loss.
- Enhance the fundamental knowledge underlying the aero-thermal interactions in gas turbine film cooling applications.
- Provide effective film cooling design guidelines for achieving an optimum aero-thermal performance.

The research objectives are achieved by implementing an optimization methodology coupled with three-dimensional CFD flow simulations.

The research will be implemented through three consecutive optimization phases, complementing one another, to achieve the established objectives. The current thesis presents the work conducted for each phase as laid out in the following chapters:

- In Chapter 2, an aero-thermal global optimization methodology is conceived for film cooling applications. The numerical components employed to form the optimization procedure are detailed.
- In Chapter 3, the film coolant flow parameters are optimized for two rows of discrete cooling holes on the suction surface of a turbine airfoil. The optimization is used to investigate the cooling performance and aerodynamic loss sensitivity to the coolant flow parameters.
- In Chapter 4, an experimental procedure is implemented in order to verify two important parameters: the accuracy of the CFD model in predicting the optimization objective

functions; and the effectiveness of the optimization methodology in identifying the optimum designs.

- In Chapter 5, the experimentally substantiated optimization methodology is used to optimize the cooling hole geometry. This optimization is employed to analyze the impact of the conical hole geometry on the cooling performance and the aerodynamic loss.

The research will conclude in novel geometric design guidelines for achieving an optimum aero-thermal design of film cooling. Such design will yield a high cooling performance and a minimum aerodynamic loss, otherwise an optimum aero-thermal performance.

CHAPTER 2

Numerical Methodology

This section presents a detailed description of the components of the proposed optimization methodology, namely, the mathematical modeling, the genetic algorithm, the artificial neural network, and the optimization algorithm.

2.1. Governing equations

CFD simulations are conducted using the commercial software ANSYS CFX v.12.1 to solve the Reynolds Averaged Navier Stokes (RANS) equations. The shear stress transport (SST) turbulence model available in CFX is selected for turbulence closure in the present study. It is a two-equation eddy viscosity turbulence model that utilizes the original k-ω model of Wilcox inside the boundary layer and switches to the standard k-ε model in the mainstream. This model developed by Menter (1994) has been shown to perform well in flows with adverse pressure gradients and separating flows.

In this study, the flow through the turbine cascade is considered three-dimensional, turbulent, steady, and compressible. Air is selected as the working fluid, consistently with the experiments, and is considered as an ideal fluid. The instantaneous governing flow and heat transfer conservation equations are presented herein. The continuity equation is:

$$\frac{\partial \rho}{\partial t} + \frac{\partial}{\partial x_i}\left(\rho U_i\right) = 0 \tag{2-1}$$

The momentum equation,

$$\frac{\partial}{\partial t}(\rho U_i)+\frac{\partial}{\partial x_i}(\rho U_i U_j)=-\frac{\partial p}{\partial x_i}+\frac{\partial t_{ij}}{\partial x_j} \tag{2-2}$$

and the energy equation,

$$\frac{\partial}{\partial t}\left[\rho\left(e+\frac{1}{2}U_i U_i\right)\right]+\frac{\partial}{\partial x_j}\left[\rho U_j\left(h+\frac{1}{2}U_i U_i\right)\right]=\frac{\partial}{\partial x_j}(U_i t_{ij})-\frac{\partial q_j}{\partial x_j} \tag{2-3}$$

where e is specific internal energy and $h=e+\frac{p}{\rho}$ is the specific enthalpy,

the molecular stress tensor, including normal and shear components, is

$$t_{ij}=2\mu s_{ij}-\frac{2}{3}\mu\frac{\partial u_k}{\partial x_k}\delta_{ij} \tag{2-4}$$

where, δ_{ij} is the identity matrix or the Kronecker Delta, and the heat flux vector is obtained from Fourier's law as

$$q_j=-k\frac{\partial T}{\partial x_j} \tag{2-5}$$

Air is assumed to be an ideal gas, and its density is calculated from the ideal gas equation of state:

$$\rho=\frac{p}{RT} \tag{2-6}$$

2.2. Turbulence modeling

Turbulence fluid motion is an irregular condition of the flow in which all flow quantities show a random variation with time and space coordinates. Turbulent flows are characterized by

properties such as irregularity, diffusivity, large Reynolds number, 3D vorticity fluctuations, dissipation and continuum. Turbulence is a complex process mainly because it occurs over a wide range of time and space scales. Turbulence must be treated using a statistical approach since it consists of random velocity fluctuations. The Reynolds averaging method consists of decomposing all flow quantities into their mean value, and their fluctuations with zero mean. Taking the velocity as an example, it is defined by:

$$U_i = \overline{u}_i + u_i' \tag{2-7}$$

Where, $\overline{u}_i$ is the ensemble-averaged value of the velocity, u_i' is the fluctuations of the velocity from $\overline{u}_i$, and is a function of time and space. The subscript *i* is the coordinate component of the velocity vector and can be either *x*, *y*, or *z*. In the subsequent sections, the subscript *j* also refers to the coordinate axis. In compressible flow, density and temperature fluctuations must also be accounted for. When the equation above is inserted into the governing flow and heat transfer equations, the Reynolds Averaged Navier-Stokes equations are obtained. In effect, the set of equations solved by ANSYS CFX are the unsteady Reynolds Averaged Navier-Stokes equations in their conservation form; ANSYS. In the equations below the over-bar referring to the ensemble average value is dropped for simplicity.

The continuity equation becomes

$$\frac{\partial \rho}{\partial t} + \frac{\partial}{\partial x_j}\left(\rho u_j\right) = 0 \tag{2-8}$$

The momentum,

$$\frac{\partial \rho u_i}{\partial t} + \frac{\partial}{\partial x_j}\left(\rho u_i u_j\right) = -\frac{\partial p}{\partial x_j} + \frac{\partial}{\partial x_j}\left(\mu\left(\frac{\partial u_i}{\partial x_j} + \frac{\partial u_j}{\partial x_j} - \frac{2}{3}\delta_{ij}\frac{\partial u_i}{\partial x_j}\right) - \rho\overline{u_i' u_j'}\right) + S_M \tag{2-9}$$

where S_M is the sum of body forces, and the energy equation becomes:

$$\frac{\partial \rho h_0}{\partial t} - \frac{\partial p}{\partial t} + \frac{\partial}{\partial x_j}\left(\rho u_j h_0\right) = \frac{\partial}{\partial x_j}\left(\lambda \frac{\partial T}{\partial x_j} - \rho \overline{u_j' h}\right) + \frac{\partial}{\partial x_j}\left[u_i\left(t_{ij} - \rho \overline{u_i' u_j'}\right)\right] + S_E \tag{2-10}$$

The mean total enthalpy is

$$h_0 = h + \frac{1}{2} u_i u_j + \frac{1}{2} \overline{u}_i'^2 \tag{2-11}$$

The last term of the mean total enthalpy equation is the turbulence kinetic energy defined as:

$$k = \frac{1}{2} \overline{u}_i'^2 \tag{2-12}$$

When averaging the instantaneous governing equations, new unknown variables are created. These unknowns appear in the Reynolds stress tensor written as follows:

$$\tau_{ij} = -\rho \overline{u_i' u_j'} \tag{2-13}$$

Turbulence modeling consists in using approximations for the unknown variables in terms of known flow parameters, such as to create sufficient number of equations for the existing number of unknown variables. Defining such approximations closes the system of equations. The Boussinesq hypothesis is used for turbulence closure in most two-equation turbulence models, particularly the shear stress turbulence model employed in the current research. The Boussinesq approximation relates the Reynolds stresses to the mean velocity gradients as follows:

$$-\rho \overline{u_i' u_j'} = \mu_t \left(\frac{\partial u_i}{\partial x_j} + \frac{\partial u_j}{\partial x_i}\right) - \frac{2}{3}\left(\rho k + \mu_t \frac{\partial u_i}{\partial x_i}\right)\delta_{ij} \tag{2-14}$$

where μ_t is the eddy viscosity or turbulent viscosity that must be modeled.

Two equation turbulence models are commonly used due to their low computational cost, and they solve for both the velocity and length scale using two separate transport equations. The two most important two-equation models are the *k-ε* and *k-ω* model. They use the Boussinesq hypothesis and relate the Reynolds stresses to the velocity gradients and the turbulent viscosity. However, the *k-ε* model requires non-linear damping function for low-Reynolds computations. The *k-ω* model is overly sensitive to mainstream conditions of *ω*.

In order to avoid the previous two drawbacks of the standard two-equation models, Menter (1994) presented a new two-equation eddy viscosity turbulence model, the shear stress transport (SST) model which consists of a blend between *k-ε* and *k-ω*, and takes into consideration the transport of the principal turbulent shear stress, $\tau_{ij} = \rho\overline{u_i' u_j'}$. SST uses the *k-ω* model in the inner region of the boundary layer and then switches to the standard *k-ε* model in the outer region and in the mainstream. To achieve this, the standard *k-ε* model is first transformed into a *k-ω* formulation by using the relation $\omega = \frac{\varepsilon}{\beta^* k}$, where $\beta^* = c_\mu$. The transformed model is then multiplied by a blending function $(1 - F_1)$ and added to the *k-ω* model that is multiplied by F_1. The resulting transport equations for the SST model are:

$$\frac{D(\rho k)}{Dt} = \tau_{ij}\frac{\partial u_i}{\partial x_j} - \beta^* \rho\omega k + \frac{\partial}{\partial x_j}\left(\Gamma_k \frac{\partial k}{\partial x_j}\right) \tag{2-15}$$

$$\frac{D(\rho\omega)}{Dt} = \frac{\gamma}{\nu_t}\tau_{ij}\frac{\partial u_i}{\partial x_j} - \beta\rho\omega^2 + \frac{\partial}{\partial x_j}\left(\Gamma_\omega \frac{\partial \omega}{\partial x_j}\right) + 2\rho(1 - F_1)\sigma_{\omega 2}\frac{1}{\omega}\frac{\partial k}{\partial x_j}\frac{\partial \omega}{\partial x_j} \tag{2-16}$$

Where $\Gamma_k = \mu + \sigma_k \mu_t$ is the effective diffusivity of k, and, $\Gamma_k = \mu + \sigma_\omega \mu_t$ is the effective diffusivity of ω.

σ_k and σ_ω are the turbulent Prandtl numbers of k and ω and they are obtained from:

$$\sigma_k = \frac{1}{F_1 / \sigma_{k,1} + (1 - F_1)/\sigma_{k,2}} \tag{2-17}$$

and,

$$\sigma_\omega = \frac{1}{F_1 / \sigma_{\omega,1} + (1 - F_1)/\sigma_{\omega,2}} \tag{2-18}$$

And the constants are:

$\sigma_{k,1} = 1.176$

$\sigma_{k,2} = 1.0$

$\sigma_{\omega,1} = 2.0$

$\sigma_{\omega,2} = 1.168$.

The last term in the ω equation is the cross diffusion term and can be referred to as

$$D_\omega = 2\rho(1 - F_1)\sigma_{\omega 2} \frac{1}{\omega} \frac{\partial k}{\partial x_j} \frac{\partial \omega}{\partial x_j} \tag{2-19}$$

Furthermore, both the production and dissipation terms of k and ω are represented in the transport equations and can be defined as follows. $G_k = \tau_{ij} \frac{\partial u_i}{\partial x_j}$ is the production of the turbulent

kinetic energy and $Y_k = \beta^* \rho \omega k$ is its turbulence dissipation. $G_\omega = \frac{\gamma}{\nu_t} \tau_{ij} \frac{\partial u_i}{\partial x_j}$ is the production of the specific dissipation rate and $Y_\omega = \beta \rho \omega^2$.

If the transport of turbulent shear stress is not taken into account, then the eddy viscosity is over-predicted. The SST model obtains the proper transport behavior by placing a limiter to the formulation of the eddy viscosity. The turbulent viscosity is then given by:

$$\mu_t = \frac{\rho k}{\omega} \frac{1}{\max\left[\frac{1}{\alpha^*}, \frac{S \times F_2}{a_1 \omega}\right]} \tag{2-20}$$

S is the strain rate magnitude and it given by:

$$S = \sqrt{2 S_{ij} S_{ij}} \tag{2-21}$$

a_1 is a constant and is defined as:

$a_1 = 0.31$

And α^* is given by $\alpha^* = \alpha_\infty^* \left(\frac{\alpha_0^* + \mathrm{Re}_t / R_k}{1 + \mathrm{Re}_t / R_k} \right)$, where, $R_k = 6$ and $\alpha_\infty^* = 1$

F_1 and F_2 are blending functions and were defined by Menter as:

$$F_1 = \tanh\left(\arg_1^4\right) \tag{2-22}$$

Where,

$$\arg_1 = \min\left(\max\left(\frac{\sqrt{k}}{\beta'\omega y}, \frac{500\nu}{y^2\omega}\right), \frac{4\rho k}{CD_{k\omega}\sigma_\omega 2y^2}\right) \tag{2-23}$$

Furthermore, it was found important for accurate qualitative prediction of the coolant flow field to couple the SST model with the full transitional model provided by CFX; ANSYS *User Guide*. The transition model is based on two transport equations, for the intermittency, and for the transition onset criteria in terms of momentum thickness Reynolds number, respectively. The transition model was developed by Menter et al. (2006) to cover natural and bypass transition. The intermittency is defined as the probability of a point in the flow field to be located inside a fully turbulent region. The value of intermittency is nil in laminar regions of the flow and reaches unity in fully turbulent flows. As for the onset of transition, it is estimated using the critical Reynolds number where the intermittency first starts to increase within the boundary layer. This critical Reynolds number occurs upstream of the transition Reynolds number, and the difference between the two was obtained from empirical correlations; Menter et al. (2006).

In the present research, it was found that transition modeling is necessary for accurately predicting the peak in surface heat transfer coefficient resulting from the transition of the laminar boundary layer to turbulence. Analysis of the results revealed as well, that transition over the film cooled blade surface is initiated by the injection of coolant.

2.3. Wall Treatment

The flow near a no slip wall can be subdivided into three layers: the viscous sublayer, the buffer layer, and the fully turbulent layer. The viscous sublayer is characterized by a laminar-like flow, in which molecular viscosity is dominant. In the fully turbulent layer, turbulence is highly dominant. While in the buffer layer, viscosity and turbulence have equal importance on the

mixing process. CFX provides an automatic near-wall treatment option for ω based models. This option switches automatically from wall functions to a low-Reynolds near wall formulation as the mesh is refined. It requires a finer mesh near the wall, hence placing grid points inside the viscous sub layer. This formulation is recommended for simulations requiring accurate boundary layer calculations such as heat transfer predictions. In k-ω turbulence models, the wall boundary conditions for the k-equation are accounted for using the automatic near-wall-treatment option.

In the wall function approach, empirical formulas are employed to connect the wall conditions to the dependent variables at the near-wall mesh node. The latter is assumed to be in the fully turbulent region of the boundary layer.

The logarithm relation for the velocity near the wall is:

$$u^+ = \frac{1}{\kappa}\ln\left(y^+\right) + C \tag{2-24}$$

Where, u^+ is the near wall velocity, κ is the von Karman constant, C is a constant dependent on the wall roughness, and y^+ is the dimensionless distance from the wall and is defined as:

$$y^+ = \frac{\rho \cdot \Delta y \cdot u_\tau}{\mu} \tag{2-25}$$

Where, Δy is the dimensional distance from the wall, and u_τ is the friction velocity given by:

$$u_\tau = \sqrt{\frac{\tau_w}{\rho}} \tag{2-26}$$

τ_w being the wall shear stress.

The wall function is problematic at low Reynolds numbers, less than 10^5, as displacement thickness errors of up to 25% can be recorded. The automatic near wall treatment provided by CFX switches automatically from wall functions to low Reynolds near wall formulations as the mesh is refined. In effect, it blends the wall value for ω between the logarithmic and the near wall formulation, while an analytical value of ω is known from the k-ω model.

The flux for the momentum equation becomes:

$$F_U = -\rho \cdot u_\tau \cdot u^* \tag{2-27}$$

with

$$u^* = \sqrt[4]{\left(\sqrt{\frac{\mu}{\rho}\left|\frac{\Delta U}{\Delta y}\right|}\right)^4 + \left(\sqrt{a_1 k}\right)^4} \tag{2-28}$$

$$u_\tau = \sqrt[4]{\left(u_\tau^{vis}\right)^4 + \left(u_\tau^{\log}\right)^4} \tag{2-29}$$

Where,

$$u_\tau^{vis} = \sqrt{\frac{\mu}{\rho}\left|\frac{\Delta U}{\Delta y}\right|} \tag{2-30}$$

and

$$u_\tau^{\log} = \frac{U}{1/\kappa \log\left(y^+\right) + C} \tag{2-31}$$

The flux for the k-equation is kept artificially to zero,

$$F_k = 0 \tag{2-32}$$

As for ω, a blend between the analytical expression in the logarithmic region:

$$\omega_l = \frac{u^*}{a_1 \kappa} y \tag{2-33}$$

and the corresponding equation in the sublayer:

$$\omega_s = \frac{6\upsilon}{\beta(\Delta y)^2} \tag{2-34}$$

to form:

$$\omega_\omega = \omega_s \sqrt{1 + \left(\frac{\omega_l}{\omega_s}\right)^2} \tag{2-35}$$

2.4. Heat Transfer Calculations in CFX

In CFX, isothermal simulations are conducted to determine the wall heat transfer coefficient. The wall boundary is therefore fixed at a specified temperature T_w. The wall heat transfer is then calculated from:

$$h_w = \frac{q_w}{(T_w - T_r)} \tag{2-36}$$

Where, T_r is the recovery temperature or the adiabatic wall temperature of the experiments which can be obtained from:

$$T_r = T_\infty + \left(1 + r\frac{\gamma - 1}{2} M_\infty^2\right) \tag{2-37}$$

Where the recovery factor r is defined as:

$$r = \frac{T_r - T_\infty}{T_0 - T_\infty} \tag{2-38}$$

For turbulent flows, it becomes:

$$r = \mathrm{Pr}^{1/3} \tag{2-39}$$

As for the wall heat flux, it is determined from:

$$q_w = \rho c_p u^* \frac{T_w - T_{nw}}{T^+} \tag{2-40}$$

Where T_{nw} stands for the near wall temperature and it is solved for in the control volume adjacent to the wall. As for u^* and T^+, they are non-dimensional and are based on the automatic near wall treatment as shown below:

$$T^+ = \mathrm{Pr}\, y^* e^{-\Gamma} + \left(2.12 \ln y^* + \beta\right) e^{-1/\Gamma} \tag{2-41}$$

Where,

$$\beta = \left(3.85\,\mathrm{Pr}^{1/3} - 1.3\right)^2 + 2.12 \ln \mathrm{Pr} \tag{2-42}$$

and,

$$\Gamma = \frac{0.01\left(\mathrm{Pr}\, y^*\right)^4}{1 + 5\,\mathrm{Pr}^3\, y^*} \tag{2-43}$$

The definition of the Prandtl number is:

$$\mathrm{Pr} = \frac{\mu c_p}{\lambda} \tag{2-44}$$

Where, λ is the thermal conductivity of the fluid (air ideal gas), and,

$$y^* = \frac{u^* \Delta n / 4}{\nu} \tag{2-45}$$

Where, Δn is the distance between the first and second grid points off the wall, which indicates that y^* is based on ¼ of the grid spacing near the wall. As for u^*, it is based on the momentum flux equation (F_U) as seen earlier in (2-27).

Finally, when adiabatic simulations are conducted, then,

$$q_w = 0 \tag{2-46}$$

2.5. Genetic Algorithm

The genetic algorithm (GA) is the most popular type of evolutionary algorithm, and has been successfully used as an optimization technique to resolve practical engineering problems. The search technique employed by genetic algorithms is based on the mechanisms of natural evolution and selection. The search starts from an initial ensemble of solutions, also called chromosomes or individuals that are randomly selected from the design space. In this study Latin Hypercube Sampling is employed to select the initial generation of individuals. Each individual, or chromosome, or solution, from that initial population can evolve, mutate, or crossover. Successive iterations are identified as generations. The individuals of each generation are evaluated based on some measure of fitness, which in this work, is chosen as the objective function. After many generations, the algorithm converges to the optimal individual or solution. In fact as the algorithm runs through generations, the population in each generation consists of better individuals. Two operations govern the search technique of the genetic algorithm, namely crossover and mutation, known as genetic operators, and selection, known as an evolution operator.

2.5.1. Selection

The selection procedure chooses an individual from the current generation to include it in the next one. The selected individual may undergo crossover and/or mutation depending on the probability of each operation, and in that case the offspring individual is transferred to the next generation as it will have the best qualities of each parent and preferably be better than both

parents. The selection scheme adopted in the present study is called the Roulette Wheel approach, and can select new generations based on fitness values.

2.5.2. Crossover

Crossover is the process of creating new offspring (or candidate solutions) from two parent chromosomes that were paired for mating. The new offspring would form the next generation of population. Crossover occurs during the optimization process according to a user-defined crossover probability P_c. Two types of crossover mechanisms are included in the genetic algorithm used in the present research. The first is an arithmetic crossover operator that combines two parent chromosomes to yield two offspring chromosomes as follows:

$$\text{Child } 1 = \alpha \text{ Parent1} + (1-\alpha)\text{Parent2} \tag{2-47}$$

$$\text{Child } 2 = (1-\alpha)\text{Parent1} + \alpha \text{ Parent2} \tag{2-48}$$

The second is a heuristic crossover operator that combines the best parent with the worst one as follows:

$$\text{Child } 1 = \text{Bestparent} + \alpha(\text{Bestparent} - \text{Worstparent}) \tag{2-49}$$

$$\text{Child } 2 = \text{Bestparent} \tag{2-50}$$

In both crossover operations α is a random number between 0 and 1.

2.5.3. Mutation

Mutation is an operation that introduces a random change in the gene values of a particular chromosome. The random value that is introduced is selected from the user defined range of the particular gene. This operation is particularly important to avoid overly fast convergence towards a local optimum. It occurs according to a user defined mutation probability P_m. If the probability

is set too high, then the optimization transforms into a random search process. The mutation probability is therefore typically set fairly low (around 0.15).

2.5.4. Elitism and convergence

Elitism is a genetic operator that ensures that the best chromosomes survives and is transmitted from one generation to another. Generally, elitism creates duplicates of the best chromosomes and places them in the new generation thus ensuring the survival of the fittest. The algorithm calculation is stopped automatically when any of the following three criteria are reached:

- The best fitness value in the current or latest generation of chromosomes becomes less than the specified fitness threshold.
- The maximum number of generation is attained.
- The elapsed evolution time exceeds the specified maximum computing time.

The GA is hence an evolutionary algorithm that does not use gradient information making it a computationally expensive optimization technique as it requires a relatively large number of iterations compared to the gradient based search methods. However, the GA cannot be trapped in local minima/maxima as it encompasses many genetic operators such as mutation and cross over.

2.6. Artificial neural network

Response surface approximation techniques are normally used to approximate the objective function instead of using computationally expensive RANS solvers to compute it. The approximation model can be combined with the optimization algorithm allowing faster optimization calculations.

In the present research, a response surface approximation model of the artificial neural network (ANN) type is used as a low fidelity model to approximate the objective function. The main

objective of using an ANN is to reduce the computational load, and speed up the optimization process.

An ANN generally consists of a number of layers, namely the input, output, and one or more hidden layers located in between the input and output. It can be defined as a computational model composed of simple elements or neurons interconnected in a re-configurable way. The model used in this research is open loop, meaning the connections between the neurons are non-recurrent. The connections between the neurons are characterized by their weights, which represent the strength of the connection. Assigning different values to the various weights exhibits the degree of influence of each neuron on the final output of the model. A neuron multiplies the various inputs by their corresponding weights, then adds those products together and feeds them to a transfer function to generate the final output. A diagram of the artificial neuron with *n* inputs is shown in Figure 2-1.

Several artificial neurons in parallel form a layer, whereas the sum of several layers constitutes a neural network. The ANN is designed using two different sets of data. One set of data is used for training the model. The second data set is used for testing the ANN and validating the accuracy of the objective function approximation.

The equations corresponding to Figure 2-1 are:

$$I = \sum_{i=1}^{n} \left(W_i X_i \right) \tag{2-51}$$

$$Y = f\left(I \right) \tag{2-52}$$

The total output Y is obtained by applying a transfer function f, also known as an activation function, to the weighted sum of outputs of the previous layer. There are three types of transfer functions;

- Step
- Sigmoid
- Tan hyperbolic

The step function is used such as to simulate a binary decision. Whereas sigmoid and tan hyperbolic are non linear functions, continuous, and differentiable. The sigmoid function is most popular and robust. It is used in the present research and is defined by:

$$f(x) = \frac{1}{1+e^{-x}} \tag{2-53}$$

The hyperbolic tan function allows a higher ANN learning speed and is defined by:

$$f(x) = \frac{e^{x} - e^{-x}}{e^{x} + e^{-x}} \tag{2-54}$$

There are two types of ANN training techniques: the unsupervised learning, in which the ANN learns from the input data only; and the supervised learning scheme, used in the present study, in which the ANN learns from the input as well as the output data.

The back propagation algorithm is used for training the multi-layered feed-forward ANN in the current study.

Finally, the error difference between the targeted output and the ANN predicted output is computed as follows:

$$E = \frac{1}{2}\sum_i (t_i - o_i)^2 \tag{2-55}$$

Where, E is the squared sum of errors, t is the target output, and o is the ANN predicted output. Depending on the magnitude of the error computed, the ANN weights are adjusted as follows:

$$W_i \leftarrow W_i + \Delta W_i \tag{2-56}$$

Where,
$$\Delta W_i = -\eta \frac{\partial E}{\partial W_i} \tag{2-57}$$

$\frac{\partial E}{\partial W_i}$ is the gradient of the error function with respect to its corresponding connection weight W_i.

η is defined as the ANN learning rate, it is problem dependent, and takes a value between 0 and 1 depending on the nature of the error surface. It is recommended to begin the training process with a low training rate.

2.7. Optimization algorithm

The flow chart in Figure 2-2 describes the complete optimization cycle used in the present work. First, the design variables are selected and an appropriate objective function is constructed. Then, the design space is clearly defined by imposing lower and upper bounds on the design variables. The design space is set-up based on the definition of the optimization problem. The Latin hypercube sampling algorithm is used next to select specific design points from the design space; this process is called the Design of Experiments. The use of Latin hypercube sampling ensures that the sampled design points are equally distributed over the design space. CFD simulations are conducted for those design points and the objective function is computed. The CFD results are used to construct the ANN model. In fact, the initial design points are sub-divided into two

groups; one is used as the training data set to the ANN, and the other as the testing data set. At the end of this step, the ANN is constructed, and its parameters are clearly defined such as the number of hidden nodes, type of transfer function, learning rates, etc.… It is then trained and tested for accuracy using the training and testing cases respectively. Then, the ANN is coupled with the genetic algorithm, to form the optimizer and search for the optimal design point within the design space.

During the optimization, the ANN is used as a low-fidelity tool for predicting the objective function. The main advantage behind using a response surface approximation model is to minimize the number of calls from the genetic algorithm to the CFD solver and hence, drastically reduce the computation and optimization cycle time. The optimum design candidate predicted by the optimizer is then analyzed using CFD simulations. The CFD-predicted objective function of the optimum design is computed and compared to the low-fidelity prediction given by the ANN. The percentage error between the two predictions is evaluated, and ANN database enrichment is carried out until the percentage error is deemed acceptable. An acceptable percentage error must be of the same order as the relative percentage error associated with the ANN test data set. The completion of this iterative process yields the final optimum solution.

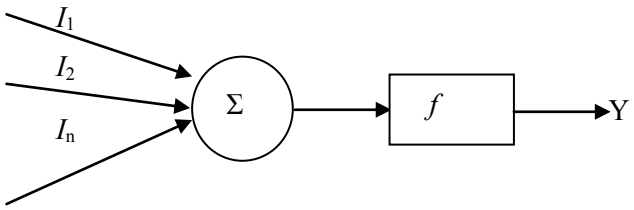

Figure 2-1: Schematic of an artificial neuron

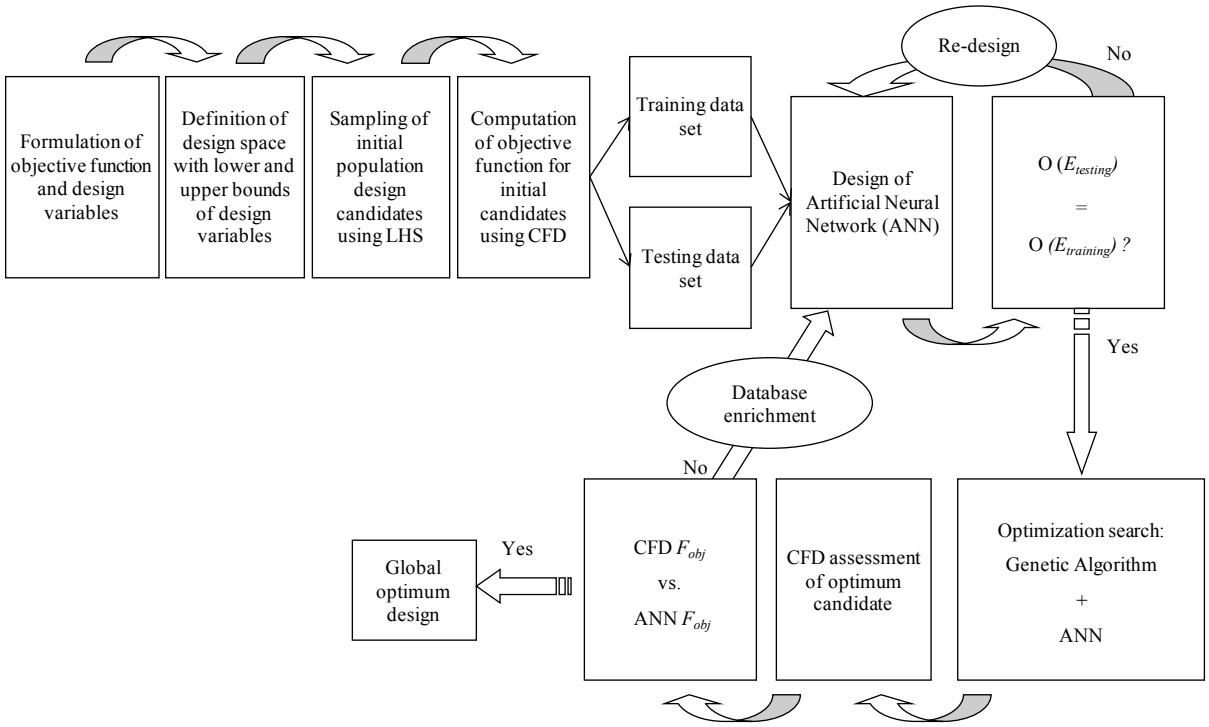

Figure 2-2: Flowchart of the optimization algorithm

2.8. Optimization objectives and design variables

The objective of the present optimization research is to simultaneously maximize the film cooling performance on the suction surface of a turbine airfoil downstream of two rows of cooling holes, and minimize the aerodynamic penalty that results from injecting the coolant into the hot mainstream flow. Throughout the optimization problem, the film cooling performance is measured using the adiabatic film cooling effectiveness, which is defined as:

$$\eta = \frac{T_\infty - T_{aw}}{T_\infty - T_c} \tag{2-58}$$

Where T_c is the static coolant temperature and T_{aw} is the adiabatic temperature of the cooled airfoil surface. The distribution of the spanwise (or laterally) averaged effectiveness, η_{span}, on the suction surface of the airfoil is an effective measure of the performance and allows for comparison between different cooling designs:

$$\eta_{span} = \frac{1}{\Delta z}\int_{-z}^{+z} \eta dz \tag{2-59}$$

The aerodynamic penalty is measured by the mass-averaged total pressure loss coefficient across the airfoil and cooling holes configuration:

$$AL = \frac{\left(\dot{m}_\infty p_{0\infty} + \dot{m}_c p_{0c}\right)_{inlet} - \dot{m}_{exit} p_{0exit}}{\left(\dot{m}_\infty p_{0\infty} + \dot{m}_c p_{0c}\right)_{inlet}} \tag{2-60}$$

The aerodynamic penalty is calculated far enough downstream from the airfoil trailing edge (two chords downstream) allowing the coolant and mainstream flows to be completely mixed out and the velocity and temperature distribution to be uniform. The approach allows for quantifying the mixing loss that results from the injection of coolant flow into the mainstream.

Multiple objective optimizations are achieved by minimizing two separate objective functions simultaneously. One function allows maximizing the cooling performance using the adiabatic effectiveness and is referred to as the thermal objective function. The other minimizes the aerodynamic loss and is referred to as the aerodynamic objective function. They are shown below:

$$F_{obj\_cooling}(X) = 1 - \eta_{surf} \tag{2-61}$$

$$F_{obj\_aero}(X) = AL \tag{2-62}$$

Where ,

$$\eta_{surf} = \frac{1}{n}\sum_{i=1}^{n}(\eta_{span,i}) \tag{2-63}$$

Single objective optimizations are achieved by minimizing one single objective function that is constructed as a weighed sum of the thermal and aerodynamic functions. The function aims to firstly, maximize the adiabatic film cooling effectiveness over the airfoil surface by maximizing (η_{surf}); secondly, ensure a uniform distribution of the cooling effectiveness on the blade suction surface; thirdly, minimize the aerodynamic loss (AL) computed at the cascade exit. The function is given by:

$$F_{obj}(X) = \left[C_1(1-\eta_{surf}) + C_2 \sum_{i=1}^{n}\sum_{j=1}^{n} \left| \eta_{soan,j} - \eta_{span,i} \right| + C_3 AL \right] \tag{2-64}$$

Where X is the vector of design variables. The thermal objective is computed at n different locations on the blade suction surface. The first term in the objective function allows maximizing the film cooling effectiveness at all n points. The second term ensures a uniform distribution of the effectiveness on the blade surface. And the third term minimizes the aerodynamic loss induced by the film cooling. C_1, C_2 and C_3 are user-defined weights ranging from 0 to 1 such that

their sum is equal to 1. The weights allow the designer to assign a different level of importance to each term of the objective function. The summation is carried over n locations on the blade suction surface. All three terms of the single objective function in equation (2-64) are normalized between 0 and 1 with respect to the minimum and maximum values in the design space.

Two types of design variables are considered in the present research:

- In Chapters 3 and 4, coolant flow parameters are selected as design variables.
- In Chapter 5, cooling hole geometric design variables are investigated.

The flow design variables that are considered in this optimization problem are as follows: the coolant to the mainstream static temperature ratio (T_c / T_∞) and the coolant to the mainstream total pressure ratio ($p_{0c} / p_{0\infty}$). These variables are the most widely used coolant flow parameters as they control the film cooling performance. The pressure ratio is related to the mass flux ratio whereas the temperature ratio is related to the density ratio. Usually, a high mass flux ratio indicates a higher coolant mass flow rate exiting the cooling holes which translates into a higher blowing ratio. Therefore, a higher blowing ratio produces a better cooling protection as long as jet lift-off does not occur. Furthermore, a lower coolant temperature, i.e. a lower temperature ratio for a fixed pressure ratio induces a better film protection. However, these two governing flow parameters may produce an opposite effect on the aerodynamic loss. In effect, the aerodynamic loss generated from the mixing of the coolant with the mainstream is governed by two fundamental mechanisms. The first is the entropy generation that results from the heat transfer process between the coolant and the mainstream due to the difference in their static temperatures. The second is the viscous dissipation that occurs because of the difference in their velocities. This implies that the higher the mass flow rate of coolant exiting the cooling holes the

higher the resulting aerodynamic penalty. It also indicates that the larger the difference in their static temperatures the higher the aerodynamic loss.

The geometric parameters that are investigated consist of the hole exit diffusion angle β, the hole lateral injection angle or the compound angle CA, and the length of the non diffused portion of the hole tube normalized but the hole diameter L_c / D. The impact of these variables on the aerodynamic loss is not available in literature. As seen earlier, some research has attempted to investigate the impact of those variables on the cooling performance but no general trend has been established. The latter remains application-specific and is dependent on the mainstream and coolant flow conditions as well as the location of film cooling on the turbine airfoil. The design space that is considered in the present work was examined and proven to be physically feasible. It allows the hole shape to vary from the standard cylindrical hole to a conically diffused one. The optimization will, therefore, sweep a very wide design space.

2.9. Uncertainty calculations

The optimum solution outputted by the optimization procedure is a dataset consisting of the ANN predicted objective function, and the corresponding optimum design variables. The uncertainties in the optimization procedure are computed by implementing the genetic algorithm for three separate optimization cycles. Meanwhile, the genetic algorithm is coupled with the same ANN for all three optimization cycles. The average deviation is then computed for the values of the objective functions and the design variables. The uncertainties were calculated for thermal and aerodynamic single objective optimizations.

During a thermal single objective optimization, the measured uncertainties for the objective function, $F_{obj\_cooling}$, and the design variables, T_c / T_∞, $p_{0c} / p_{0\infty}$, L_c / D, β, and CA are $\mp$ 0.05%,

0.3%, 0.8%, 2.8%, 0.04°, and 1.34° respectively. During an aerodynamic single objective optimization, the measured uncertainties for F_{obj_aero}, T_c / T_∞, p_{0c} / $p_{0\infty}$, L_c / D, β, and CA are $\mp$ 0.23%, 0.2%, 0.02%, 3.6%, 0.4°, and 1.9° respectively.

CHAPTER 3

Film Cooling Optimization on the VKI Blade Suction Surface

In this chapter a turbine blade from literature with suction side film cooling is selected for optimization. The von Karman Institute (VKI) blade is typical of a first stage high pressure turbine airfoil. The cooling scheme placed on its suction surface is representative of current machining limitations and consists of two staggered rows of axially oriented, conically flared, film cooling holes.

As stated earlier, the initial optimization task is focused on optimizing film coolant flow parameters. Two design variables are selected: the coolant to mainstream temperature and total pressure ratios. The objective is to obtain an optimum compromise ensuring a maximum film cooling effectiveness and a minimum aerodynamic loss.

3.1. Heat transfer to the non-cooled VKI blade

Prior to the film cooling optimization work, the heat transfer distribution on the non-cooled VKI blade is investigated using RANS simulations, and the predicted data assessed against the experimental database available in literature, generated by Consigny and Richards (1982). To this end, the commercial software ANSYS CFX v.12.1 is employed.

Consigny and Richards (1982) conducted an experimental investigation that analyzed the effect of Mach number, Reynolds number, inlet flow angle, and mainstream turbulence level on the

heat transfer rate to the non-cooled VKI blade. All measurements reported in their paper, Consigny and Richards (1982), were performed on the blade's mid-span section.

3.1.1. CFD model

The VKI blade is two-dimensional cylindrical, meaning it has the same airfoil profile throughout its span. Only one cascade passage is modeled for the present numerical flow simulations. The geometry of the blade and the CFD domain is created in CATIA V5R19. The airfoil curvature is constructed in CATIA by fitting a spline through the curvature points given by Camci (1985). The inlet of the CFD domain is placed one chord upstream of the blade leading edge. The outlet is placed one chord downstream of the trailing edge. Table 3-1 summarizes the main flow parameters for the transonic blade cascade as found in Consigny and Richards (1982), and Table 3-2 summarizes the main geometric parameters.

The three-dimensional computational domain is shown in Figure 3-1. A two-dimensional section in the *xy* plane is shown in Figure 3-2. A stagnation pressure of 288,000 Pa, stagnation temperature of 415K, a turbulence intensity level of 5%, and a flow direction of 30^{o} is specified at the inlet boundary to the CFD domain. An initial guess for the exit static pressure is computed from the isentropic approximation. The exit static pressure is then adjusted iteratively to match the exit isentropic Mach number of 0.92 as cited in Consigny and Richards (1982). Periodic boundary conditions are set along the mid-pitch line to model an infinite cascade. Adiabatic, no-slip wall boundary conditions are specified at the end walls in the spanwise direction. There was no need to conduct conjugate heat transfer simulations since a wall temperature of 290K, provided in Consigny and Richards (1982), is applied on the blade surface. The no-slip wall condition is also specified on the blade surface.

A multi-block unstructured grid was constructed in ICEM CFD v12.1, and consists of 600,000 hexahedral elements. An O-grid is wrapped around the blade and an H-mesh is used for the flow passage. The O-grid ensures that mesh elements are orthogonal to the blade surface. An exponential clustering law is used inside the boundary layer. The distance of the first grid node away from the blade surface normalized by the blade chord is set to 1.10^{-4}. An element growth ratio from the wall of 1.1 is used. The clustering allows a non-dimensional wall distance (y^+) below unity.

RANS simulations are conducted using the commercial software ANSYS CFX v12.1 to resolve the flow field and obtain the blade surface heat transfer coefficient distribution. The SST turbulence model is used for turbulence closure. Convergence of the simulations is established when the following three criteria are met:

- The root mean square of the normalized residual of the mass, momentum, and energy equations is reduced to $10^{-4.}$
- The integral mass and energy imbalances of the entire flow domain fall below 10^{-5}.
- Target values that are being monitored reach a steady solution that is no longer changing with successive iterations.

A single CFD simulation reaches convergence in about 1500 iterations. Each computation is subdivided into 6 to 8 tasks and performed on the Concordia HP parallel computing cluster which consists of AMD Opteron processors (x86, 64 bit, dual core). Convergence requires typically a total wall clock time of about 1 to 2 days.

Numerical predictions of the wall heat transfer coefficient are computed using Equation (2-36), and the recovery temperature is obtained from Equation **Error! Reference source not found.**) sing a recovery factor of 0.896, which is suggested in the experiment Camci and Arts (1985).

3.1.2. CFD predictions

Figure 3-3 presents the blade surface isentropic Mach number distribution. The results are presented with respect to the curvilinear distance (s) on the blade suction surface downstream of the stagnation point normalized by the blade chord (C). No flow separation or spanwise flow shift was observed on the surface of the blade. The CFD predictions are compared against the experimental data of Consigny and Richards (1982) and predictions by Medic and Durbin (2002b) who employed the k-ε turbulence model coupled with a bound on the turbulent time scale to avoid over prediction of turbulence in stagnation regions. A discrepancy on the aft of the blade suction surface is observed and exhibits an over prediction of the Mach number. The same trend is noted with the prediction of Medic and Durbin (2002b). The remaining of the surface distribution agrees well with the experimental data. The discrepancies observed on the blade suction surface between the numerical and experimental data were attributed to two experimental difficulties as mentioned in Consigny and Richards (1982). First, the Mach number is deduced from the value of total to static pressure whereas more accurate data could have been obtained from velocity measurements using differential transducers. Secondly, larger diameter tubes were used on the suction surface than on the pressure surface which could have caused cramping and leaks and hence scattered data.

The heat transfer predictions obtained with the current numerical model are compared with those of Medic and Durbin (2002b) who performed CFD simulations using the standard k-ω model, the k-ω model with a bound on the turbulent time scale, and the v^2-f model. Figure 3-4 shows the

comparison. Most turbulence models under-predict the heat transfer coefficient on the pressure surface and over-predict it on the suction surface. The over prediction on the suction surface downstream of the stagnation region is attributed to the occurrence of transition on the blade surface. The over prediction in the stagnation region is explained by Durbin (1996) as an anomalous over production of turbulent kinetic energy. This is known in literature as the "stagnation point anomaly". The present heat transfer results obtained with the SST fully turbulent model compare well with the v^2-f predictions provided by Medic and Durbin (2002b).

Table 3-1: Main flow parameters of the VKI blade cascade; Consigny and Richards (1982)

M_{in}	0.25
$p_{e\infty} / p_{0in,\infty}$	0.574
$T_{0,in}$ [K]	415
T_w [K]	290
Tu_{in}	5%
Re_C	$8.5 \cdot 10^5$
$M_{e,\,is}$	0.92

Table 3-2: Main geometric parameters of the VKI blade cascade; Consigny and Richards (1982)

True chord length [mm]	80
Span [mm]	100
Stagger angle	38.5^o
Inlet blade angle	30^o
Inlet flow angle	30^o
Outlet flow angle	69.5^o

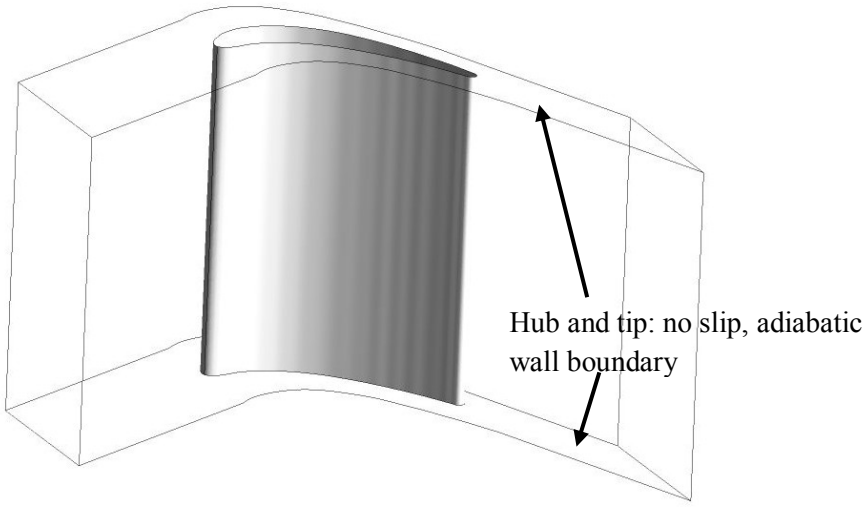

Figure 3-1: The 3D CFD domain of the non-cooled VKI blade

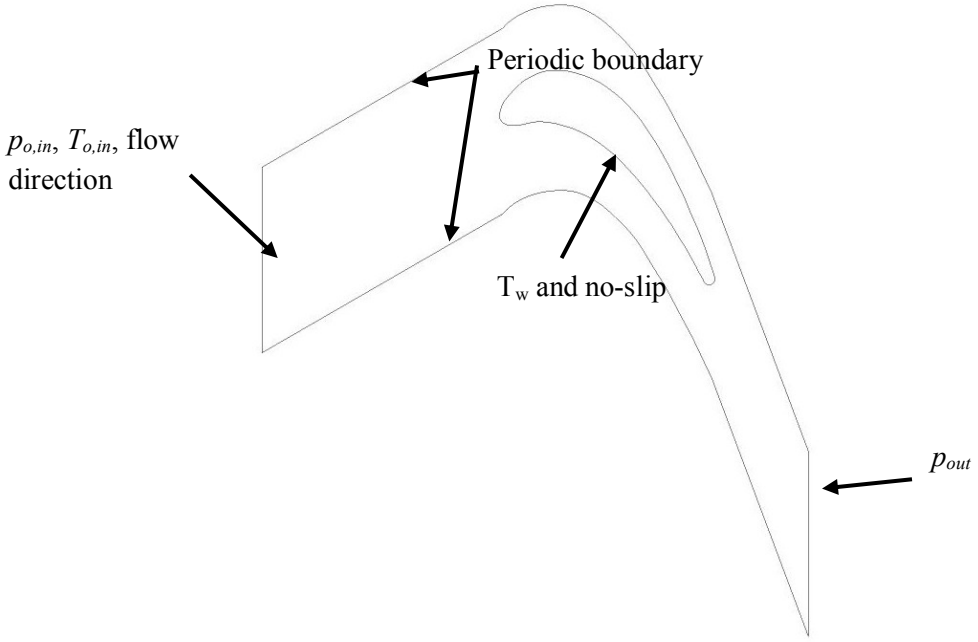

Figure 3-2: 2D profile of the CFD domain of the non-cooled VKI blade

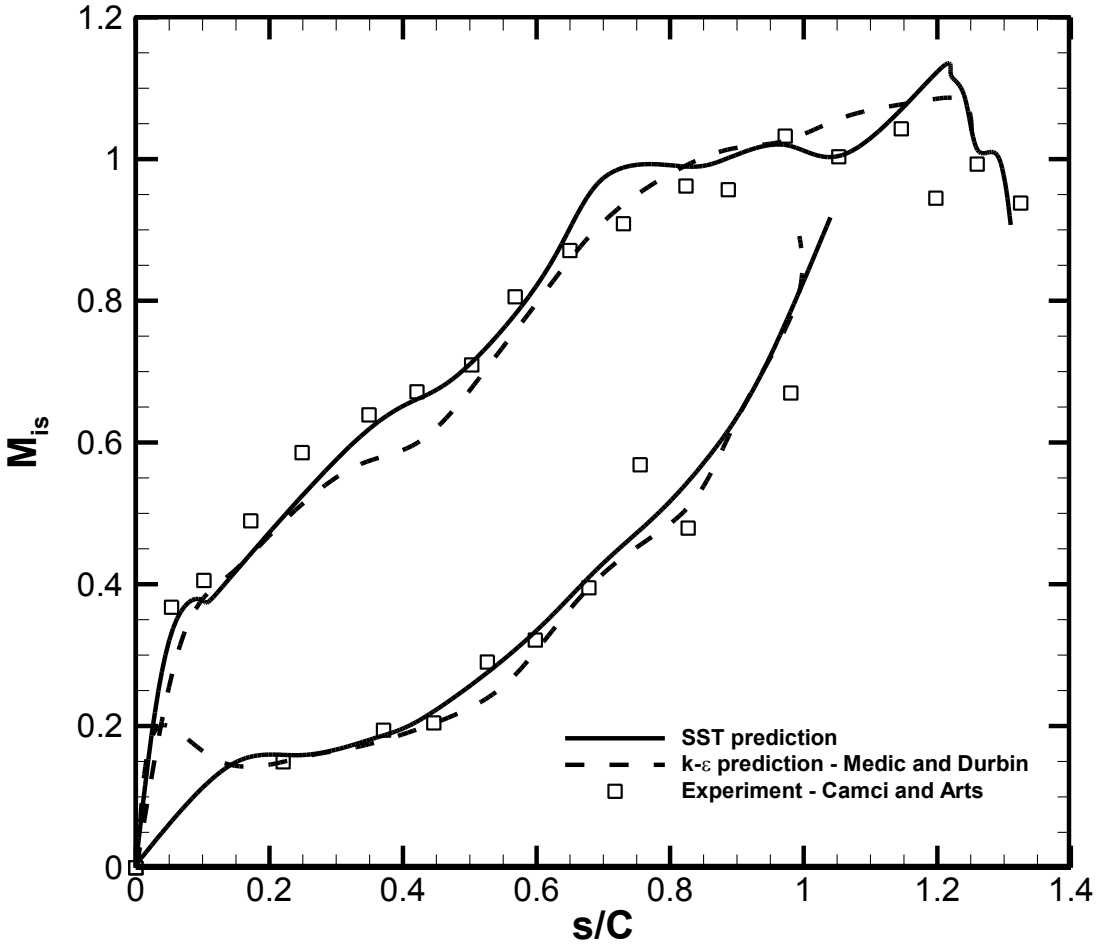

Figure 3-3: Isentropic Mach number distribution at the mid-span of the VKI blade

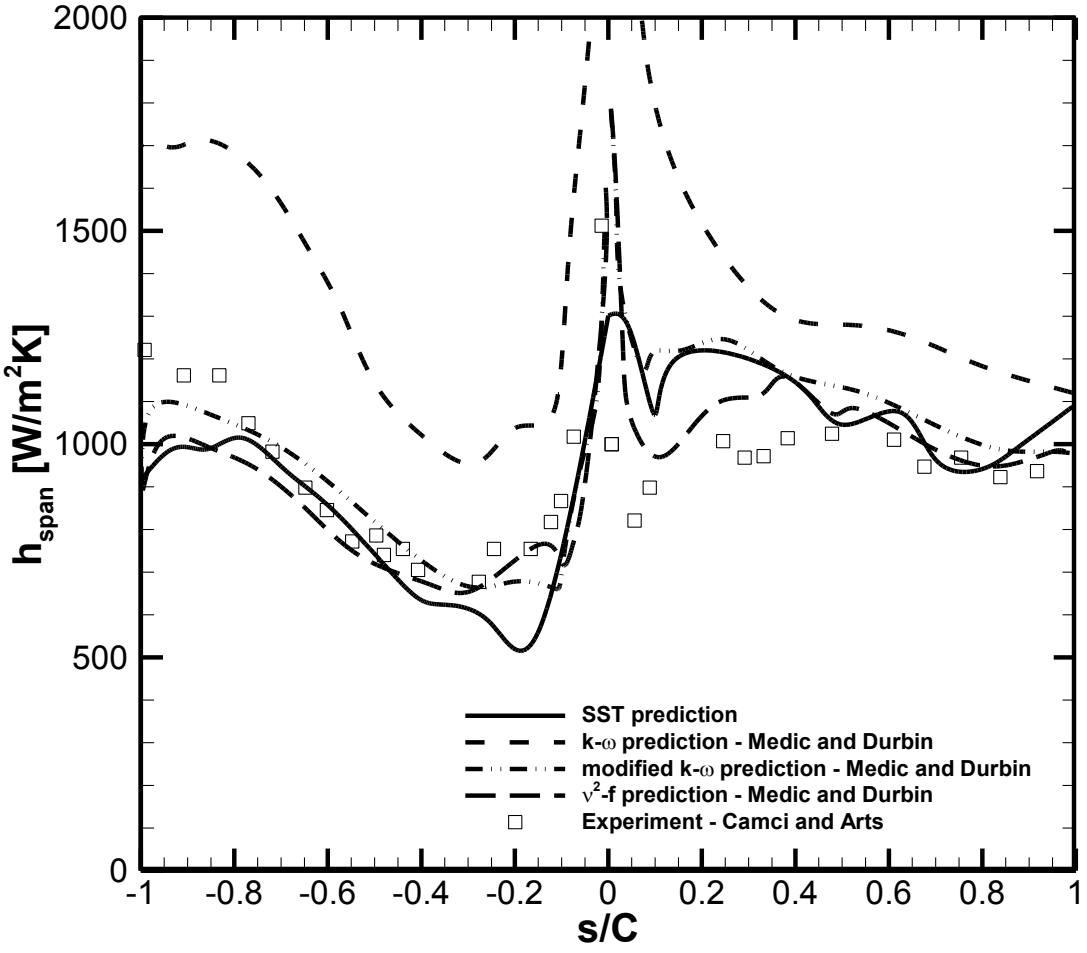

Figure 3-4: Surface heat transfer coefficient distribution at the mid-span of the non-cooled VKI blade

3.2. Heat transfer to the film cooled VKI blade

Camci (1985) conducted heat transfer investigations for the VKI blade, with suction surface film cooling. In the work of Camci and Arts (1985), several coolant inflow conditions are analyzed, namely for blowing ratios varying between 0.43 and 1.0, and coolant temperatures varying from the blade wall temperature (i.e. $T_c = T_w = 298$K) down to half of the mainstream temperature (i.e. $T_c = T_\infty/2 = 205$K). Their experimental results are reproduced in the present study using the commercial software ANSYS CFX v12.1.

3.2.1. CFD model

The computational domain consists of the mainstream, the plenum, and the cooling holes. A two-dimensional profile of the CFD domain is given Figure 3-5. The inlet to the domain is placed one chord upstream of the blade leading edge, and the exit is placed one chord downstream of the trailing edge in accordance with the experimental test section of Camci (1985). Two staggered rows of axially oriented conically flared film cooling holes are placed on the blade suction surface. They are located at the non-dimensional curvilinear distances $s/C = 0.206$ and $s/C = 0.237$. The holes are flared conically using a conical expansion angle of $\beta = 10^o$ below the exit of the hole. The holes are angled at $\alpha = 37^o$ and $\alpha = 43^o$ with the blade surface and the row spacing is 2.5 mm; the holes spacing is 2.6 mm and diameter is 0.8 mm. The details of the cooling holes configuration are presented in Figure 3-6.

Air is employed as the working fluid for both the mainstream and the coolant and is assumed to be an ideal gas. The mainstream flow is under the same conditions as in the previous section where no film cooling was present. Periodic boundary conditions are applied along the mid-pitch line to model an infinite cascade. Only one full cooling hole pitch is modeled in the spanwise direction. Symmetry planes are applied at the centre of the two adjacent film holes in the second

row of holes. This effectively models a blade with an infinite span. The main geometric and flow parameters of the blade cascade are summarized earlier in Table 3-1 and Table 3-2

The plenum total inlet pressure is iteratively adjusted until the experimental blowing ratio is reached.

A multi-block unstructured grid is constructed in ICEM CFD v12.1. The computational domain is divided into several blocks to allow more control over the grid quality and density. An O-grid is wrapped around the airfoil. An exponential clustering law is used inside the boundary layer. The distance of the first grid node away from the blade surface normalized by the blade chord (y/C) is set to 10^{-4}. An element growth ratio from the wall of 1.1 is used. The clustering of the elements near the blade surface yields a non-dimensional wall distance (y^+) below unity. An H-mesh is used for the remaining of the mainstream flow. The entire mainstream is meshed using hexahedral elements. As for the plenum and cooling hole tubes, tetrahedral elements are used with prism layers clustered at the walls of the plenum and cooling hole tubes to obtain a $y+$ below unity. The mesh on either side of the cooling hole exit does not match since the plenum side consists of tetrahedral elements and the mainstream side consists of hexahedral elements. A general grid interface connection, provided by CFX, ANSYS *User Guide*, is used in between the two overlapping meshes. Details of the computational mesh are presented in Figure 3-7.

RANS simulations are conducted using the commercial software ANSYS CFX v12.1 to resolve the flow field and obtain the blade surface heat transfer coefficient distribution. The numerical predictions are compared with data from Camci (1985) to assess the accuracy of the CFD model. The SST turbulence model is used for turbulence closure. Convergence of the present simulations is established when the following three criteria are met:

- The root mean square of the normalized residual of the mass, momentum, and energy equations is reduced to $10^{-4.}$
- The integral mass and energy imbalances of the entire flow domain fall below 10^{-5}.
- Target values that are being monitored reach a steady solution that is no longer changing with successive iterations.

A single CFD simulation reaches convergence in about 1400 to 2000 iterations. Each computation was subdivided into 6 to 8 tasks and performed on the Concordia HP parallel computing cluster which consists of AMD Opteron processors (x86, 64 bit, and dual core). Convergence requires typically a total wall clock time of about 2 days. The present CFD model is used subsequently to predict the aero-thermal cooling performance, which is measured in terms of the adiabatic film cooling effectiveness (η) and the mass-averaged total pressure loss coefficient (AL).

3.2.2. CFD predictions

The blade surface distribution of isentropic Mach number is presented earlier in Figure 3-3 and the CFD model is shown appropriate for accurate resolution of the aerodynamic flow field around the blade.

A turbulence model sensitivity study is conducted; the turbulence models that are investigated include the standard k-ε, the RNG k-ε, and the SST model. The blade surface heat transfer coefficient (h) is found to be very sensitive to the turbulence model as it is dependent on near wall viscous effects. Furthermore, the surface heat transfer in film cooling applications is strongly dependent on the interaction occurring between the coolant and mainstream flows, and accurate depiction of such interaction relies heavily on the turbulence model, the mesh clustering

through the film cooling holes and around their exit. The heat transfer coefficient along the blade suction surface downstream of the two rows of cooling holes is presented in Figure 3-9. The SST turbulence model is found to be the most appropriate one in predicting the wall heat transfer and is used for all subsequent CFD simulations. The heat transfer predictions are obtained at the reference design point at a blowing ratio of 0.43; the latter is defined as the ratio of coolant to mainstream mass fluxes and is given by:

$$BR = \frac{\rho_c U_c}{\rho_\infty U_\infty} \tag{3-1}$$

Where the film coolant flow parameters are mass-averaged and measured at the exit of the film cooling-hole in accordance with the experiments of Camci (1985).

In general, deviations of the numerical results from the experimental data are not higher than 10%. Furthermore, the experimental uncertainty for the heat transfer coefficient was ±7.6% as provided by Camci (1985). It is deemed that the agreement is reasonable between the current numerical predictions and the experimental data. Furthermore, it is worth noting that the experimental data of Camci (1985) and Camci and Arts (1985) do not incorporate effectiveness values; therefore a comparison of the effectiveness values from CFD with experimental data is not possible. However, computing the heat transfer coefficient involves computing the temperature gradient along the blade wall. Based on numerical methods principles, the computation of the temperature gradient is less accurate than the computation of the actual temperature. The latter enforces a higher confidence level in the fact that all other flow variables such as the temperature fields, the centreline, and laterally averaged cooling effectiveness are

computed accurately. The numerical model is therefore proven reliable to provide predictions of the film cooling performance measured in terms of film cooling effectiveness.

The sensitivity of the surface heat transfer coefficient to the mesh size is investigated as well. Three mesh sizes were examined. The mesh topology is similar for all three meshes. A fine resolution of elements is employed in the region near the cooling-hole exits. The node count in the streamwise direction (x) is varied, namely, upstream of the blade leading edge, on the blade surface, and downstream of the blade trailing edge. The node count in the circumferential direction (z) is varied as well. y^+ is kept below unity for all three meshes. Figure 3-10 provides a comparison of the wall heat transfer coefficient predictions for all three meshes. The mesh consisting of 4.8 million elements is selected for all subsequent analysis as it was deemed to provide acceptable accuracy at a reasonable computing time.

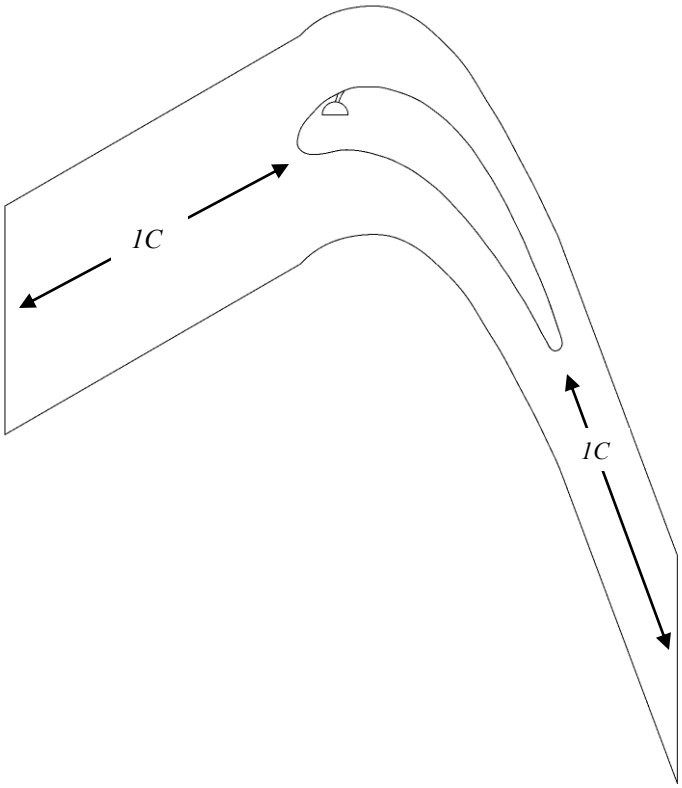

Figure 3-5: 2D profile of the CFD domain of the film-cooled VKI blade

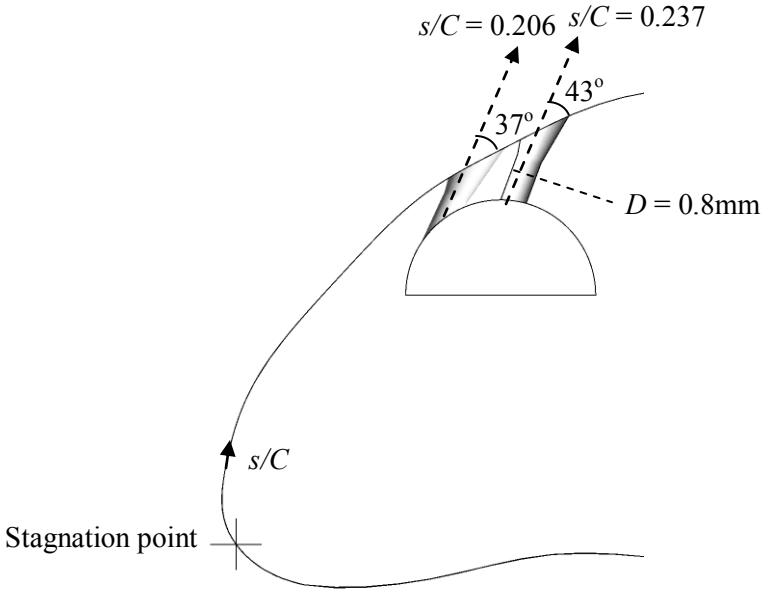

Figure 3-6: 2D details of the cooling hole configuration on the VKI blade suction surface

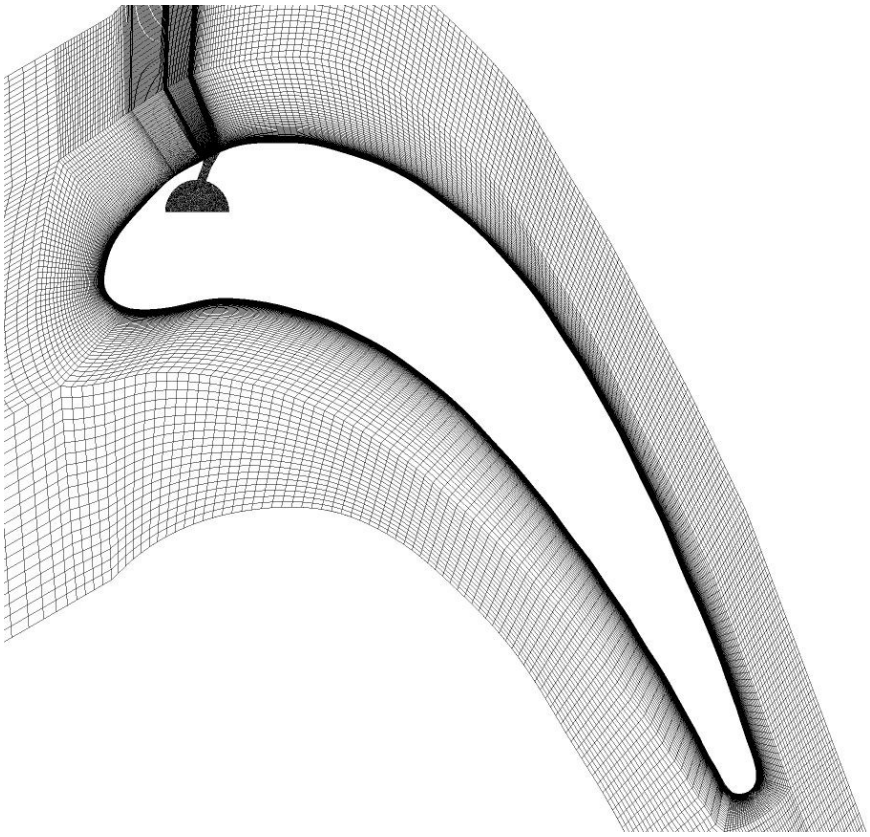

Figure 3-7: Details of the computational grid around the cooled VKI blade

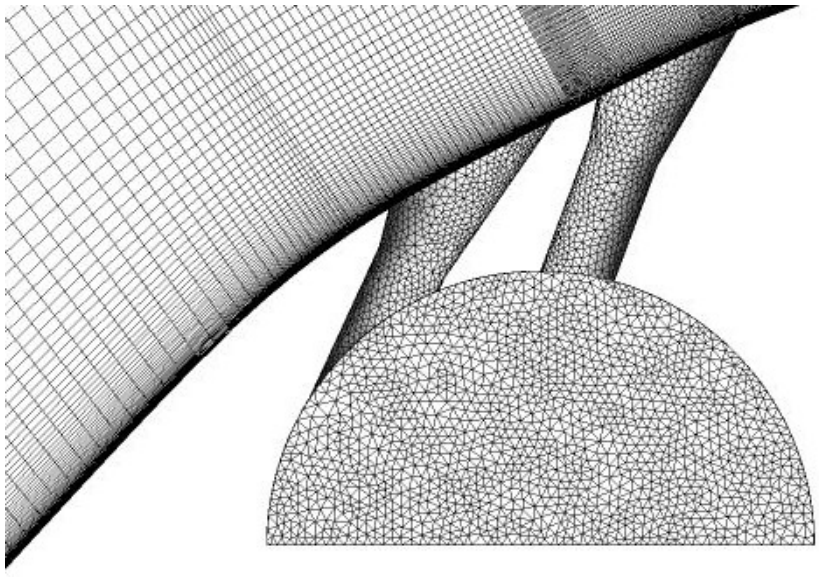

Figure 3-8: Details of the computational grid inside the coolant plenum and at the blade wall

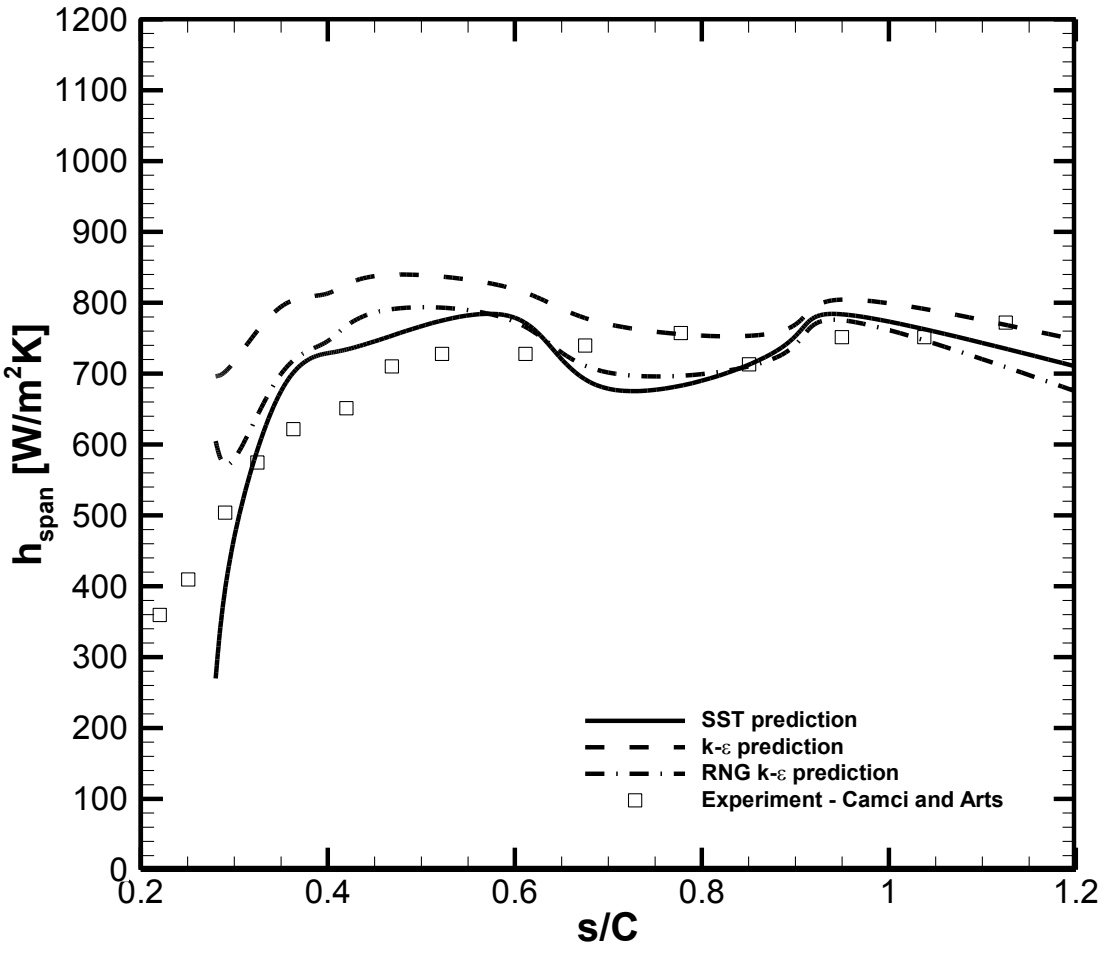

Figure 3-9: Sensitivity of the laterally averaged wall heat transfer coefficient distribution to turbulence modeling at BR = 0.43

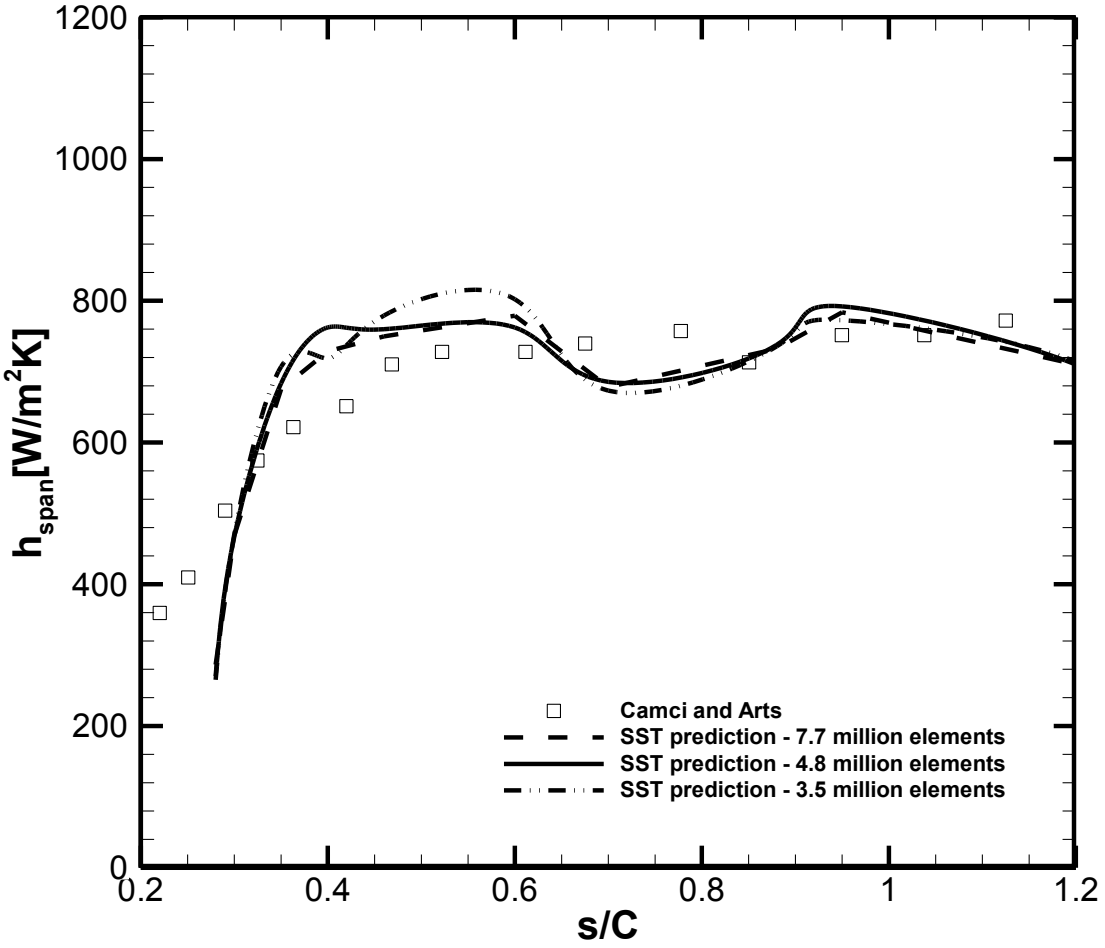

Figure 3-10: Sensitivity of the laterally averaged wall heat transfer coefficient distribution to mesh refinement at BR = 0.43

3.3. Film cooling optimization for the VKI blade

In this first optimization problem, two design flow variables are considered: the coolant to the mainstream static temperature ratio (T_c / T_∞) and the coolant to the mainstream total pressure ratio ($p_{0c} / p_{0\infty}$). The objective of the present optimization is to simultaneously maximize the film cooling performance on the blade suction surface downstream of the two rows of cooling holes, and minimize the aerodynamic penalty that results from film cooling.

A single objective optimization function is constructed as a weighted sum of three-components that aim to: firstly, maximize the adiabatic film cooling effectiveness over the blade suction surface (η_{surf}); secondly, ensure a uniform distribution of the cooling effectiveness on the surface; thirdly, minimize the aerodynamic loss (AL) computed at the cascade exit. The optimization algorithm aims to minimize the objective function that is given in equation (2-64). Initially, the user defined weights are set to $C_1 = 0.45$, $C_2 = 0.05$, and $C_3 = 0.5$ to reach an aero-thermal optimum where equal importance is assigned to a high cooling performance and a low aerodynamic loss.

A multiple objective optimization is conducted to generate the Pareto front of the design space. The single objective function given in (2-64) is broken down into two separate functions. The optimization aims to minimize both of these functions simultaneously; one insuring a maximum cooling performance, $F_{obj\_cooling}$ of equation (2-61), and one insuring a minimum aerodynamic penalty, F_{obj_aero} of equation (2-62).

3.3.1. Single objective optimization results

The design space constituted by the lower and upper limits of the design variables is shown in Table 3-3. Ten design candidates are selected using Latin Hypercube Sampling (LHS). CFD

simulations are performed for these design candidates to yield predictions of the cooling and aerodynamic objective functions. CFD predictions of the aerodynamic loss (AL), and the adiabatic cooling effectiveness averaged over the suction surface of the blade downstream of the cooling holes (η_{surf}) are presented in Table 3-4. The ANN is trained with 70% and tested with 30% of the data set. It is designed with one hidden layer composed of 14 nodes.

Figure 3-11 presents the evolution of the RMS training and testing errors during the construction of the ANN. The x-axis represents the number of computing iterations of the ANN. At around 10,000 iterations both testing and training errors reach a plateau. The ANN training is stopped at this point, where the testing error is minimal.

The ANN is then coupled to the genetic algorithm to approximate the objective function during the optimization. Four database enrichments are carried out. For every database enrichment, the genetic algorithm reaches convergence, and yields an optimum that is simulated using CFD. The optimum case is then added to the database, and the ANN is retrained again and used in the next genetic algorithm search. Each genetic algorithm generation consists of 50 individuals. The optimization process converges after about 1,400 generations. The mutation probability is set to 0.15, whereas the cross over probability is set to 0.7. Two elite individuals are transferred from one generation to the next. Figure 3-12 presents the evolution of the CFD predicted objective function with the database enrichment cycles. It shows as well the evolution of η_{surf} and AL. The objective function decreases by 28.7% after four database enrichment cycles. This improvement is translated into a noticeable increase in η_{surf} from 0.12 to 0.27 whereas AL changes by less than 1%. Figure 3-13 shows that the database enrichment improves the ANN accuracy. The optimal solution selected at the end of this iterative process is obtained with an ANN accuracy of 0.5%.

Since this error is lower than the ANN testing error of 2.5% (corresponding to a RMS error of 0.05, see Figure 3-11), the optimization process is deemed completed.

Figure 3-14 presents the sensitivity of AL and η_{surf} to the two design variables. In accordance with the aforementioned discussion and the authors' expectations, AL increases slightly with increasing $p_{0c} / p_{0\infty}$, or the aerodynamic penalty increases with increasing blowing ratio. Figure 3-14 shows also that AL decreases with increasing T_c / T_∞ which agrees with the fact that decreasing the difference between the properties of the mainstream and those of the coolant flow, namely temperature and velocity, reduces the AL. As for η_{surf}, it decreases with increasing T_c / T_∞, in other words, the cooling performance improves with lower film coolant temperatures. Conversely, it increases with increasing $p_{0c} / p_{0\infty}$ until it reaches the maximum η_{surf} value at $p_{0c} / p_{0\infty} = 0.94$, which corresponds to a blowing ratio (BR) of 0.57, for a constant $T_c / T_\infty = 0.72$. Beyond this particular pressure ratio, the cooling performance starts decreasing as the coolant begins to detach from the surface of the blade and the coolant lateral spreading begins to narrow down. The reduced lateral spreading yields increased blade surface areas that are unprotected from the hot mainstream gas. Furthermore, the behaviour of F_{obj} as noted previously is almost a mirror image of that of η_{surf}. This indicates that for the present film cooling application, the cooling performance is much more sensitive to the design variables than the aerodynamic penalty.

The user-defined weights (C_i) are employed to assign particular levels of importance to maximizing the cooling performance and minimizing the aerodynamic penalty. Table 3-5 presents the optimization results for five different variations of the user-defined weights. Case1 is obtained for $C_1 = 0.45$, $C_2 = 0.05$ and $C_3 = 0.5$, and corresponds to an equal level of importance to a maximum η_{surf} and a minimum AL. This optimum case is the one that has been analyzed

previously. Case2 consists of a slight variation as $C_1 = 0.5$ and $C_2 = 0$. The thermal part of the optimization is focused solely on increasing η_{surf}, and no consideration is given its uniformity on the blade surface. η distribution, shown in Figure 3-15, demonstrates that assigning 5% weight value to C_2 yields an optimum case with a lower blowing ratio, as indicated by the lower peak of η. However, it results in a higher η_{surf} value on the blade surface. Based on these observations, a value of $C_2 = 0.05$ was used for all subsequent cases.

Case3 is obtained for C_1 and C_3 equal to 0.70 and 0.25, i.e. more weight is assigned to the cooling performance. As expected, Case3 has a higher $p_{0c} / p_{0\infty}$ and a lower T_c / T_∞ than Case1. Since more emphasis is assigned to a maximum η_{surf}, more coolant mass flow is required and lower coolant temperature is needed. Furthermore, the design space is constructed for $p_{0c} / p_{0\infty}$ varying between 0.85 and 1.1. However, coolant lift-off is recorded at $p_{0c} / p_{0\infty} = 1.0$. Therefore, the maximum possible cooling performance that can be obtained for the present cooling set-up will be reached for $p_{0c} / p_{0\infty}$ lower than 1.0 always. This trend is detected by the optimization as Case3 has $p_{0c} / p_{0\infty}$ and a blowing ratio that are higher than Case1 and Case2.

Moreover, Case4 is obtained for a purely thermal optimization; meaning the third component of the optimization function is non-existent and AL is ignored in the optimization process, i.e. the user-defined weights are set to $C_1 = 0.95$, $C_2 = 0.05$ and $C_3 = 0$. For this particular situation, the optimum case corresponds to the maximum $p_{0c} / p_{0\infty}$ possible before inducing coolant separation. It also corresponds to the minimum T_c / T_∞. In effect, the optimization methodology employed in the present research was successful in recognizing this requirement, and the optimization algorithm converged to $p_{0c} / p_{0\infty} = 0.967$ and $T_c / T_\infty = 0.401$. $p_{0c} / p_{0\infty}$ and BR are the highest amongst the different optimum cases obtained. T_c / T_∞ is the lowest. Subsequently, Case4 yielded the highest η_{surf} and the highest AL as well.

Finally, Case5 is obtained for a purely aerodynamic optimization; meaning the first two components of the optimization function, which account for the cooling effectiveness, are ignored and only the AL is taken into account in the optimization process. The user defined weights are therefore $C_1 = 0$, $C_2 = 0$ and $C_3 = 1$. As expected, Case5 corresponds to the lowest allowable $p_{0c} / p_{0\infty} = 0.853$ and the highest allowable $T_c / T_\infty = 0.798$. Consequently, Case5 exhibits the lowest η_{surf} amongst all optimum cases and the lowest AL. The present exercise re-enforces the confidence level in the proposed optimization methodology as a valid and effective one that can be used in the design of film cooling applications in gas turbines.

The η_{span} distribution on the blade suction surface downstream of the cooling holes is presented in Figure 3-15 for Case1, which is referred to as the aero-thermal optimum, and for the original case. The optimum η_{span} peak is shifted downstream of the original peak. Also, the value of the optimum η_{span} peak is lower than that of the original case. This indicates a greater mass flow of coolant exiting the cooling holes for the optimum, which is confirmed by the higher blowing ratio recorded in Table 3-5.

Furthermore, Figure 3-15 illustrates the superior cooling performance of the aero-thermal optimum since the level of η_{span} is higher overall on the blade suction surface, namely for s/C ranging between 0.4 and 1.4 ($s/C = 0.4$ being downstream of the hole, and $s/C = 1.4$ being at the blade trailing edge). The optimum η_{span} is 15% higher than the original; this constitutes a good improvement in cooling. It is important to note that the optimization started from an original case that was shown by Camci and Arts (1985) to provide a good cooling performance as well.

Figure 3-16 presents coloured contours of η on the blade surface. It is observed that immediately downstream of the cooling holes, the original η value is higher than the optimum. This is related

to the fact that the original case has a blowing ratio lower than the optimum. The optimum case presents an increased coolant mass flow rate exiting the hole hence, pushing the coolant further away from the surface of the blade and resulting in a lower cooling effectiveness immediately downstream the holes. However, the optimum coolant trace on the blade surface persists all the way to the blade trailing edge in contrast with the original case. For the original case, η drops to 0.57 at around s/C = 0.37, whereas the contour of η = 0.57 prevails until s/C = 0.47 for the optimum case. The optimum contours of high η cover a wider and longer part of the blade surface. This translates into a better cooling performance as observed in Figure 3-15.

Coloured contours of the non-dimensional coolant temperature Θ are shown in Figure 3-17, and plotted on two *xy* planes passing through the hole centrelines of the first and second rows of film holes. The two planes are superimposed for visualization purposes. The extent of the coolant penetration into the mainstream can be evaluated through this figure. The Θ contour of unity extends higher in the vertical direction (y) and reveals a deeper penetration of the coolant into the mainstream. This observation is in accordance with the fact that the optimum is obtained for a higher blowing ratio. This means that a higher mass flow rate is exiting the cooling hole, which suggests a higher coolant momentum at the hole exit, which leads to more penetration of the coolant into the mainstream. Conversely, the original case is obtained at a lower blowing ratio, indicating a lower momentum of the coolant exiting the cooling holes, which leads to less penetration of the coolant in the mainstream. This indicates that the original η peak is higher than the optimum as was shown previously in Figure 3-15.

Figure 3-18 presents the normalized turbulence kinetic energy k/U_∞^2 on a *yz* plane, normal to the flow direction, and located downstream of the second row of cooling holes at s/C = 0.35. Compared with the optimum, the original case exhibits a higher turbulence intensity level over a

wider region. This indicates a higher heat transfer performance in this specific location for the original case, and a much stronger interaction of the coolant with the mainstream, leading to a higher *AL* in comparison with the optimum case. Conversely, the optimum presents a much narrower region of high turbulence kinetic energy in comparison with the original case. This indicates a lower heat transfer performance at $s/C = 0.35$ (shortly downstream of the hole), which is confirmed in Figure 3-16. It also indicates a lower *AL* than the original case.

Figure 3-19 depicts vorticity contours on the same *yz* plane located downstream of the second row of cooling holes at $s/C = 0.35$. The contours illustrate the kidney vortices that are usually observed in film cooling downstream of the cooling holes. The original case exhibits vortices with a core that is wider or, more elongated in the spanwise direction. Alternatively, the vortices presented by the optimum case are differently shaped. The core is smaller and is less stretched out in the lateral direction. Kidney shaped vortices bring the coolant cores closer together, detach the coolant from the surface by lifting it in the vertical direction, hence reducing the film cooling effectiveness.

Table 3-3: Design space and design variables

Design variable	Lower bound	Upper bound
$p_{0c}/p_{0\infty}$	0.85	1.10
T_c/T_∞	0.40	0.80

Table 3-4: CFD prediction for the LHS design candidates

Design Candidate	Input from LHS		CFD Output		
	$p_{0c}/p_{0\infty}$	T_c/T_∞	η_{surf}	AL	BR
1	1.079	0.473	0.207	0.485	1.24
2	1.031	0.762	0.248	0.504	0.84
3	0.982	0.690	0.289	0.499	0.74
4	0.909	0.654	0.261	0.488	0.49
5	1.006	0.581	0.275	0.506	0.90
6	1.055	0.617	0.221	0.512	1.01
7	0.885	0.798	0.220	0.481	0.34
8	0.958	0.726	0.295	0.495	0.64
9	0.861	0.509	0.136	0.477	0.27
10	0.934	0.545	0.285	0.494	0.649

Table 3-5: CFD predictions for the optimum design cases at different user defined weights

	Design weights			GA output (ANN based)		CFD output		
	C_1	C_2	C_3	$p_{0c}/p_{0\infty}$	T_c/T_∞	η_{surf}	AL	BR
Case1	0.45	0.05	0.50	0.956	0.809	0.302	0.493	0.60
Case2	0.50	0.00	0.50	0.950	0.616	0.292	0.495	0.67
Case3	0.70	0.05	0.25	0.959	0.707	0.297	0.495	0.65
Case4	0.95	0.05	0.00	0.967	0.401	0.305	0.505	0.92
Case5	0.00	0.00	1.00	0.853	0.798	0.094	0.473	0.21

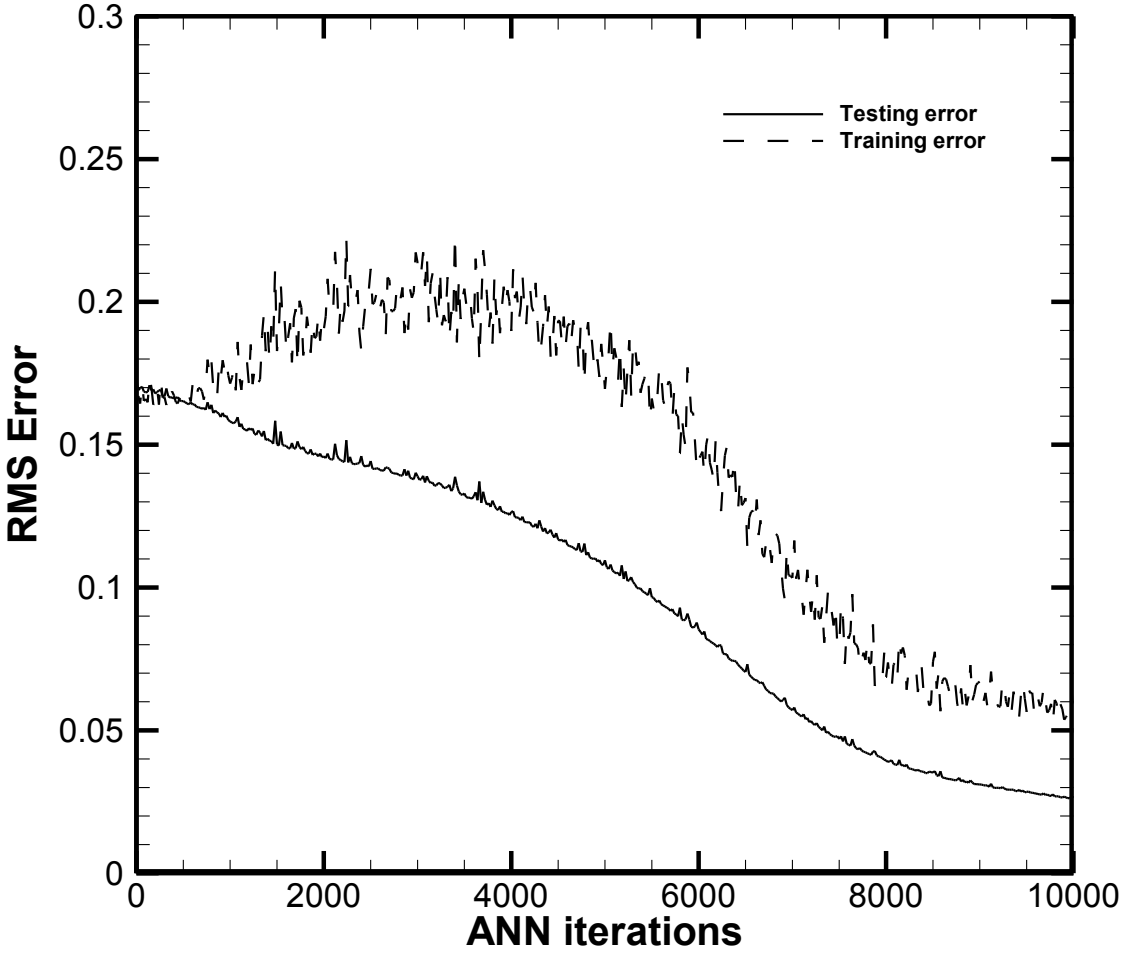

Figure 3-11: Evolution of ANN training and testing RMS errors

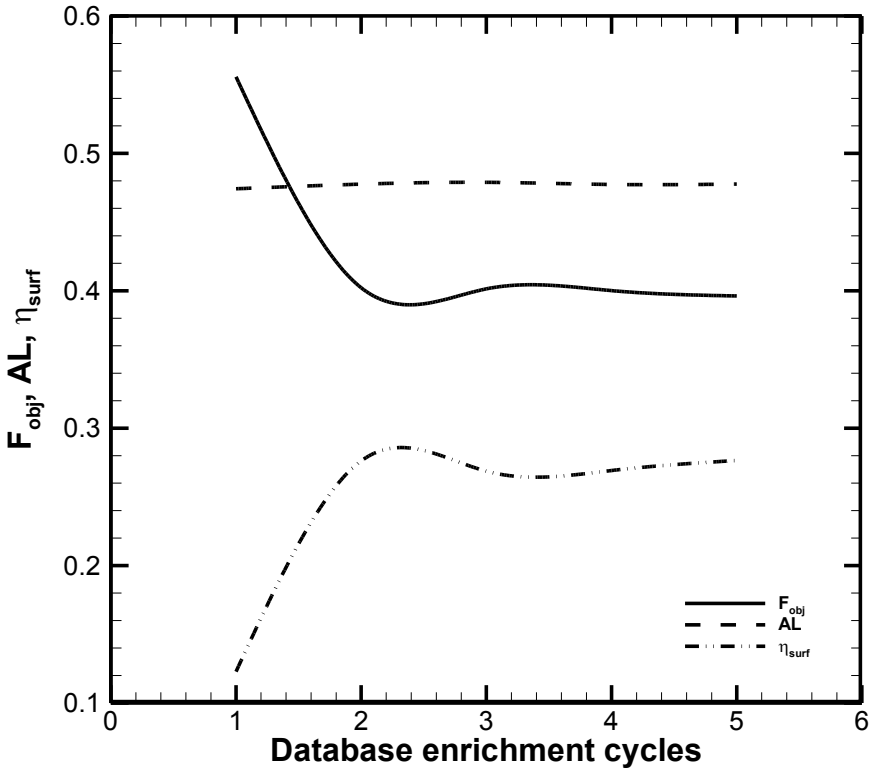

Figure 3-12: Evolution of F_{obj}, η_{surf}, and AL with database enrichment cycles

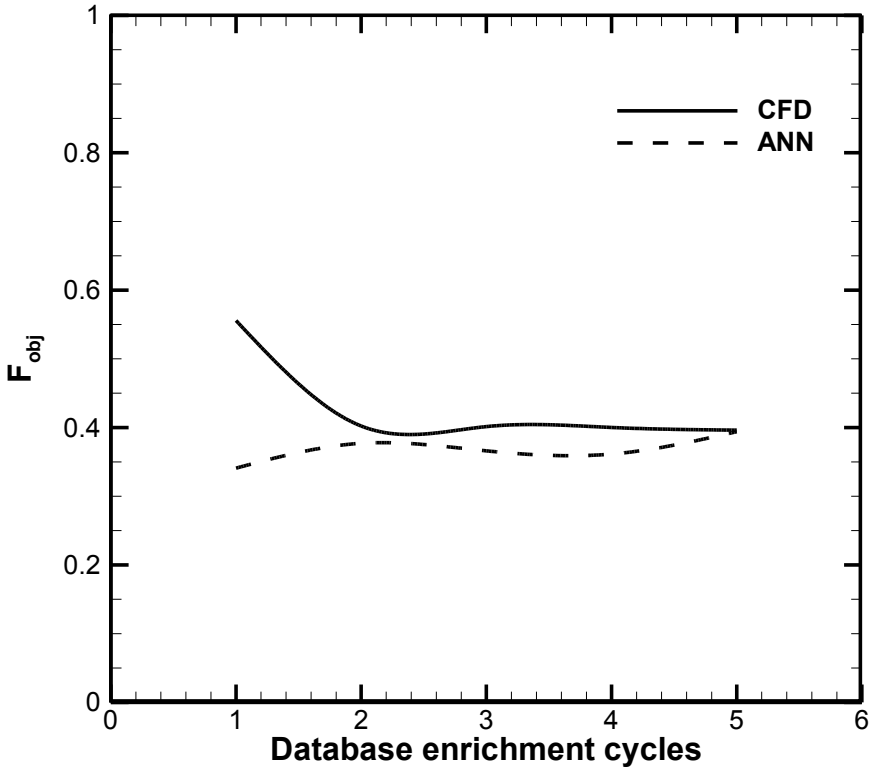

Figure 3-13: Effect of database enrichment cycles on the ANN accuracy

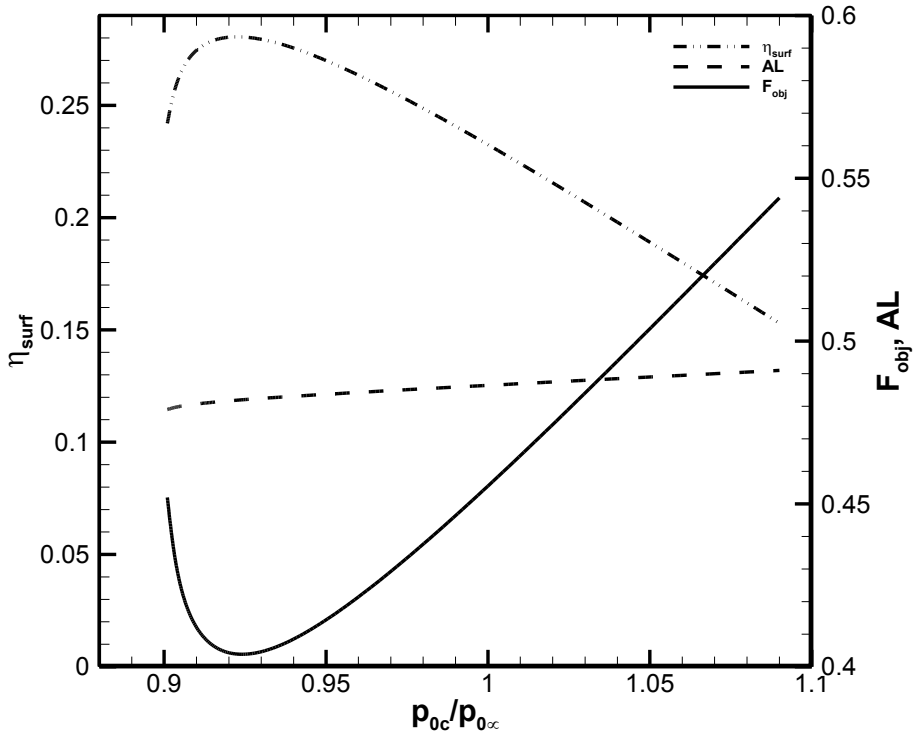

Sensitivity to total pressure ratio at constant $T_c / T_\infty = 0.72$

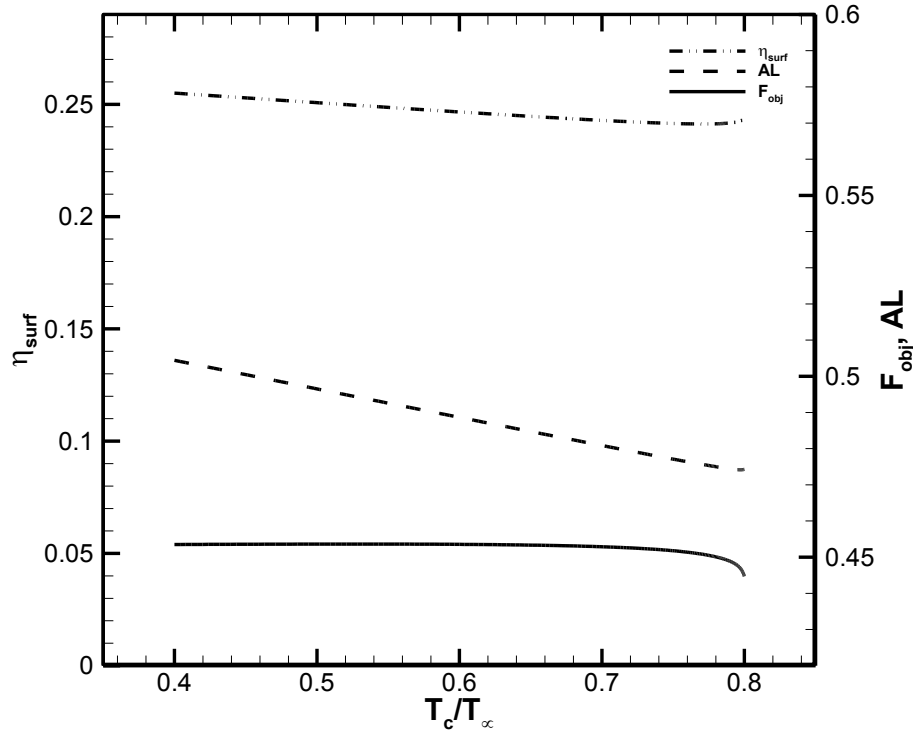

Sensitivity to temperature ratio at constant $p_{0c} / p_{0\infty} = 0.90$

Figure 3-14: Sensitivity of the CFD predictions of *AL*, η_{surf}, and F_{obj} to the design variables

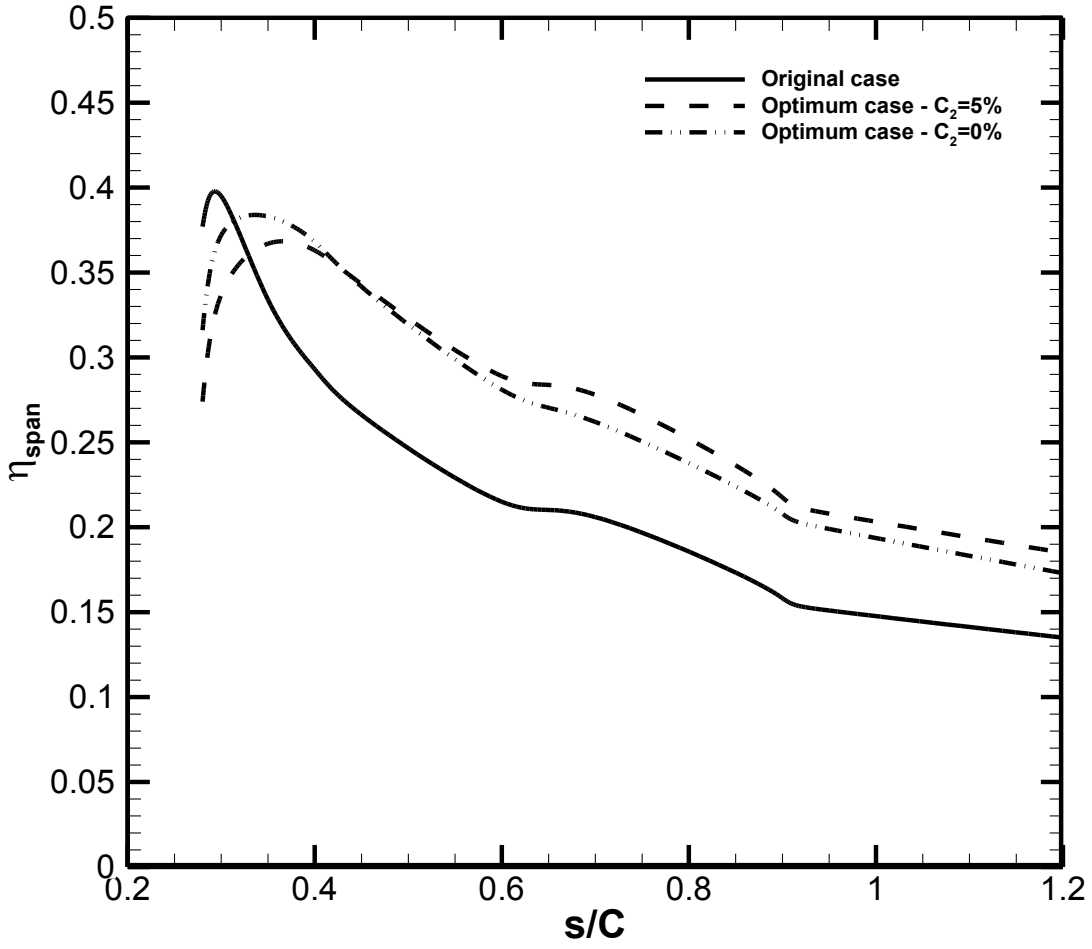

Figure 3-15: Adiabatic cooling effectiveness distribution for the optimum and original cases and the effect of different values of C_2

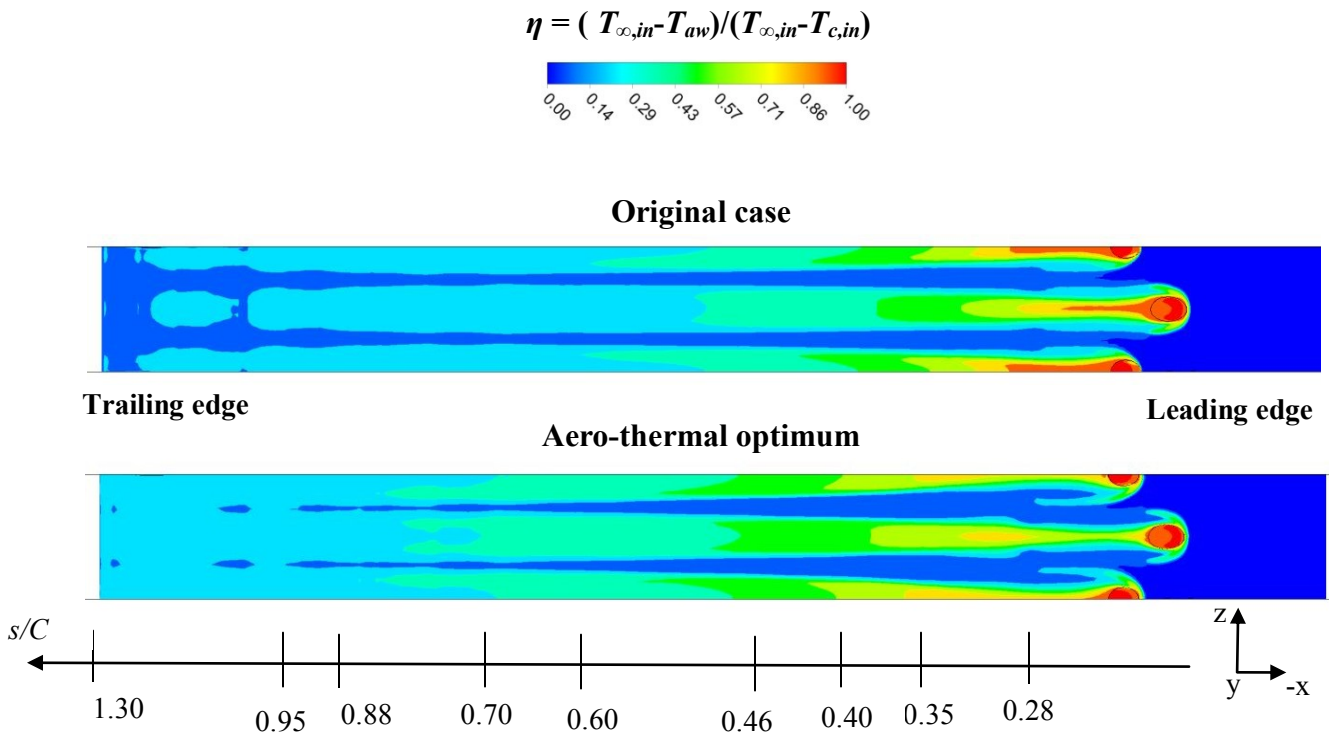

Figure 3-16: Adiabatic cooling effectiveness contours on the suction surface for the optimum and original cases

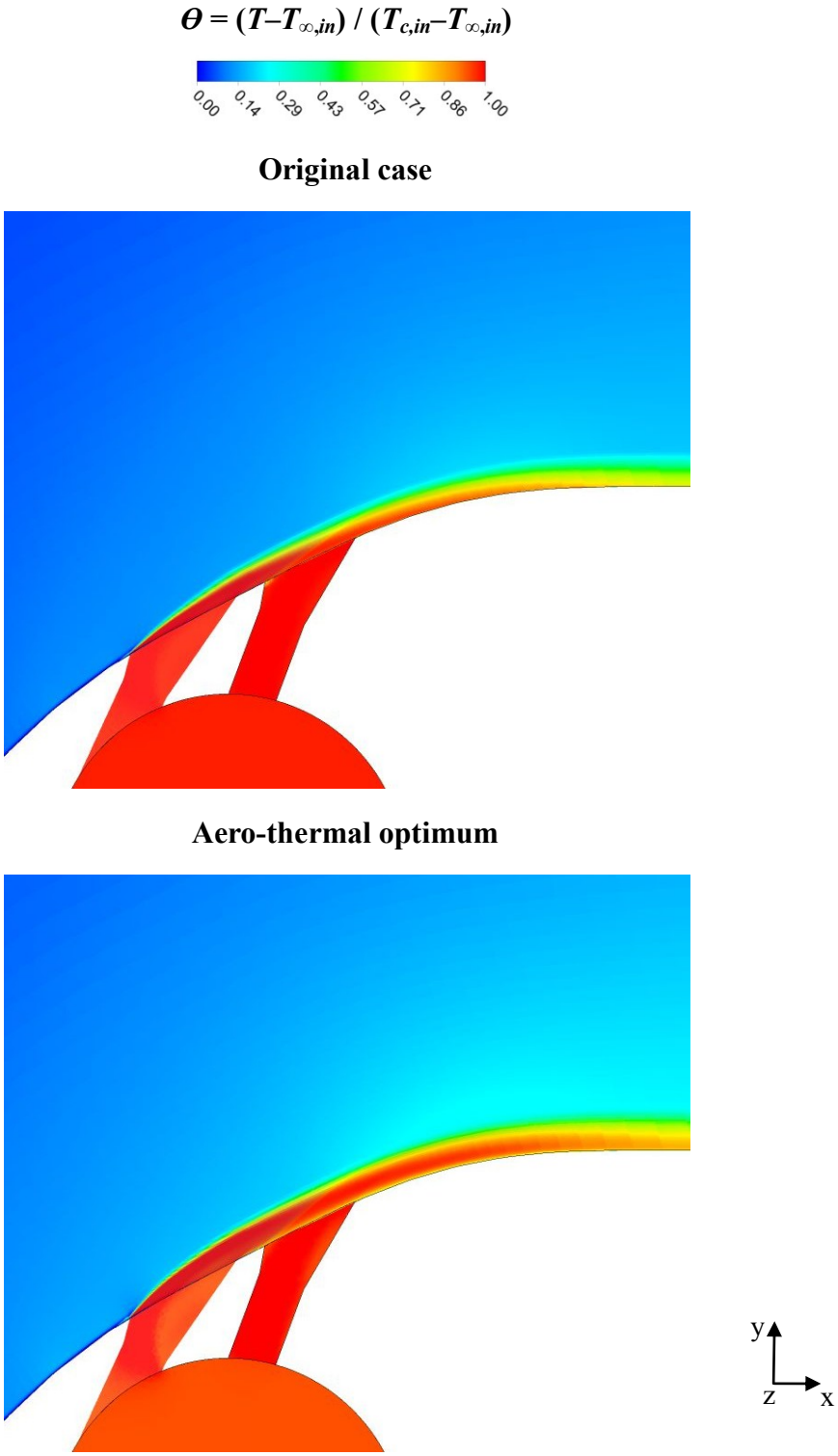

Figure 3-17: Non-dimensional temperature contours on *xy* planes located along the centrelines of the first and second rows of holes

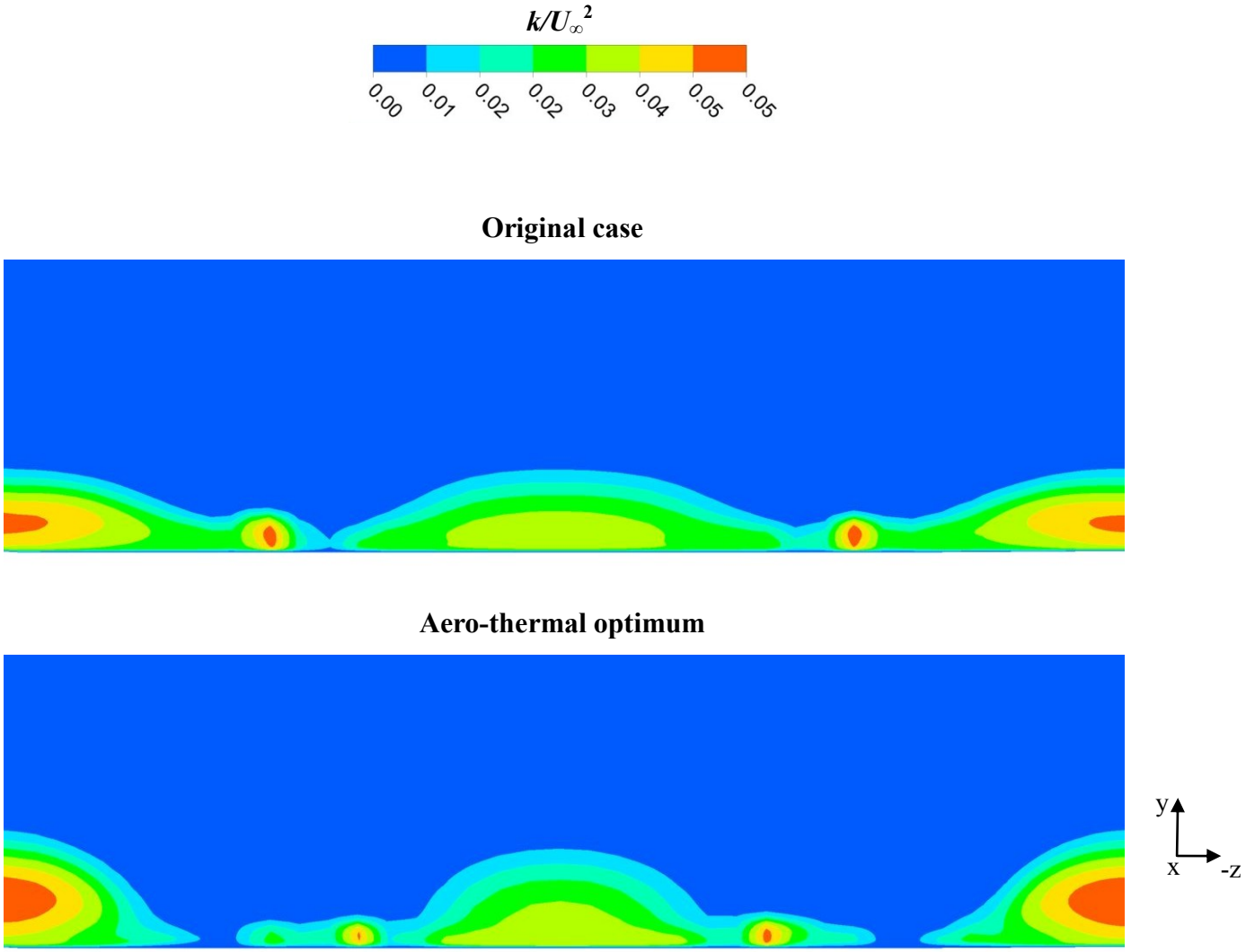

Figure 3-18: Turbulence kinetic energy contours on a *yz* plane located at *s/C* = 0.35

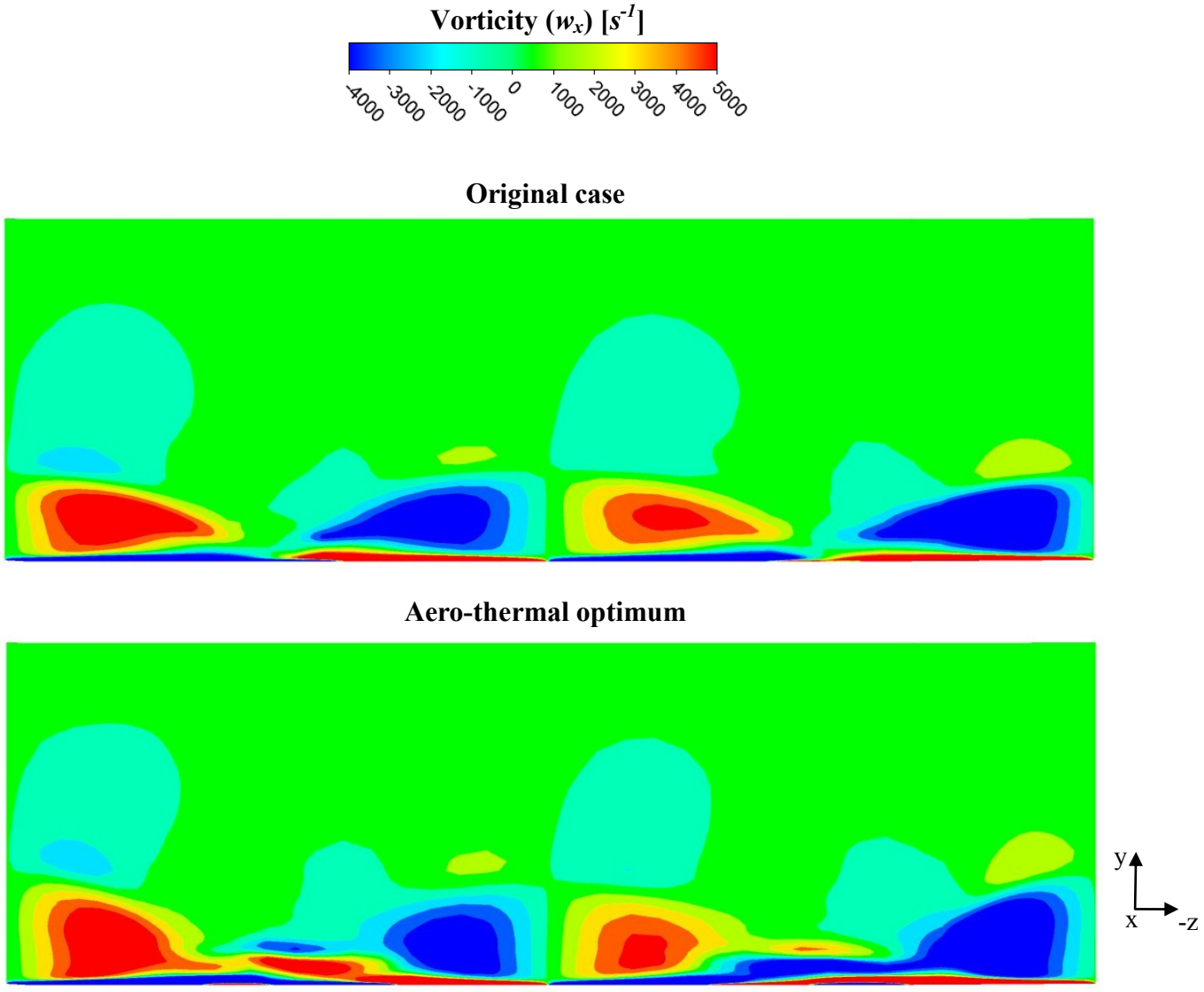

Figure 3-19: Vorticity (w_x) contours on a *yz* plane located at $s/C = 0.35$

3.3.2. Multiple objective optimization results

The optimization methodology adopted herein is in a way similar to the single objective optimization presented earlier. The design variables are the same: $p_{0c} / p_{0\infty}$ and T_c / T_∞. The optimization objectives are also the same: η_{surf} and AL. However, for a multiple objective optimization, there are two objective functions that are simultaneously and independently optimized using the Non-dominated sorting Genetic Algorithm, the so-called NSGA-II developed by Deb (2001).

The non-dominated sorting procedure employed in the optimization ensures that no solution on the Pareto-front is superior to any other solution on the same front. Each genetic algorithm generation consists of 100 individuals, and the optimization is stopped after 70 generations. The value of crossover and mutation probabilities is 0.7 and 0.15, respectively. Two elite individuals are transmitted from one generation to the next.

The Pareto optimum solutions computed using the ANN-based NSGA-II, are shown in Figure 3-20 forming the Pareto front, which is composed of all the optimum design points obtained from the two-objective optimization. It is a concave curve of the thermal objective function, given by ($1-\eta_{surf}$), vs. the aerodynamic objective function, given by AL. This front represents the competing nature of the two objectives, where any improvement in AL results in deteriorating η_{surf} and vice-versa. This Pareto front allows the designer to make a choice as to which way to go: get a better thermal performance at the expense of a higher aerodynamic loss, or have a compromise between the two.

3.4. Conclusion

The proposed optimization methodology is implemented for the VKI blade, which is a typical first stage high-pressure cooled turbine blade. The cooling scheme placed on its suction surface is adequate for current machining limitations and consists of two staggered rows of axially oriented conically flared cooling holes.

The flow parameters, namely the coolant to mainstream total pressure ratio and static temperature ratio, were used as design variables while the optimization objectives were to improve the adiabatic film cooling effectiveness while reducing the aerodynamic loss represented by the total pressure loss coefficient.

The proposed optimization approach was tested on the VKI blade, and resulted in a 16% increase in film effectiveness without any significant impact on aerodynamic losses (0.2% reduction in the total pressure loss coefficient). This improvement in cooling performance was obtained when assigning equal importance to cooling performance and aerodynamic loss inside the optimization objective function.

The multiple objective optimization allowed for generating the Pareto front where different design choices can be made.

The optimization approach was therefore capable of identifying the aero-thermal flow interactions occurring inside a turbine cascade with film cooling. In effect, the analysis of the optimum design solutions using CFD indicated that the optimization approach detected the opposing effect of the blowing ratio and the coolant temperature on the cooling performance and the aerodynamic loss. Increasing the blowing ratio improved the cooling performance as long as coolant lift-off from the blade surface did not occur. However, this had a detrimental effect on

the aerodynamic loss, which increased with increasing coolant mass flow rate. On the other hand, increasing the coolant temperature improved the aerodynamic loss due to a reduction in thermal dissipation between the coolant and mainstream flows. However, this had detrimental effects on the cooling performance, which decreased with increasing coolant temperature.

No cooling effectiveness data was available for the VKI blade, therefore the CFD model accuracy in predicting the cooling performance could not be established definitively, and was only assumed based on numerical methods principles. This draws the need for an experimental work in the aim to verify two essential parameters:

- The accuracy of the CFD model in predicting the cooling effectiveness and the aerodynamic loss.
- The efficiency of the optimization methodology in identifying the optimum designs.

The above experimental work is executed in the next chapter.

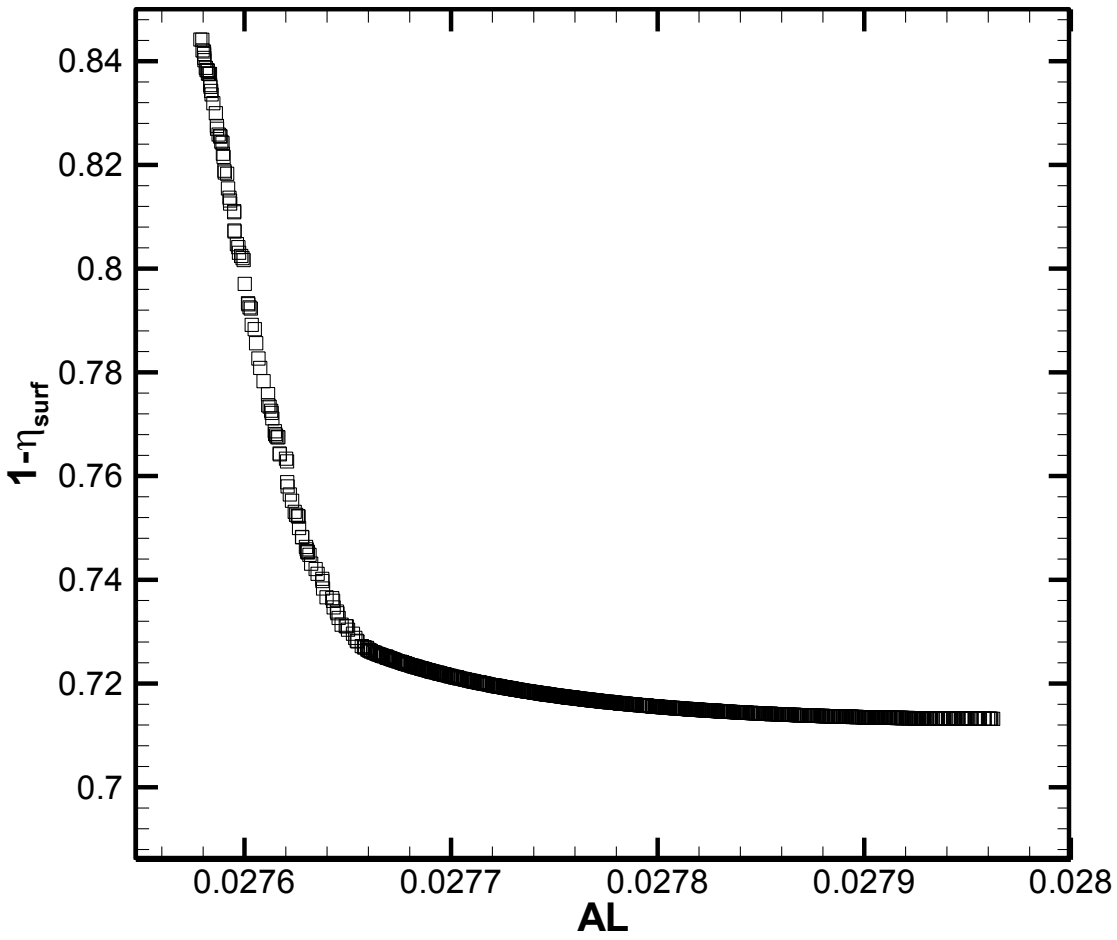

Figure 3-20: Pareto front of optimal solutions obtained with ANN-based NSGA-II results

CHAPTER 4

Experimental Verification of the Film Cooling Optimization on a Vane Suction Surface

The present chapter consists of experimental work that is conducted in the aim to verify two essential parameters for establishing a reliable optimization methodology:

- The accuracy of the CFD model in predicting the cooling effectiveness and the aerodynamic loss.
- The efficiency of the optimization methodology in identifying the optimum designs.

For this purpose, the optimization methodology that was proposed earlier in Chapter 2, and tested in Chapter 3, is applied here on an airfoil similar to the VKI blade. The airfoil is a vane typical of an initial stage of a high-pressure turbine. Consistently with the previous work, the vane experiences film cooling on its suction surface through a double row of cylindrical cooling holes that are axially oriented and disposed in a staggered arrangement.

The present work objectives are achieved by assessing against experimental measurements the accuracy of the CFD model in predicting: the aerodynamic flow field around the vane, the cooling effectiveness distribution on the vane surface, and the optimization objective functions. The experimental work is also employed to assess the accuracy of the optimization methodology in identifying the optimum designs within a selected design space.

4.1. Experimental methodology

The experimental work is conducted in a wind tunnel established at Concordia University and shown in Figure 4-1. Due to space and cost limitations, only subsonic conditions of the mainstream are achieved. Therefore, the VKI cascade operating conditions could not be implemented in the current experimental facility. Instead, a turbine vane cascade, similar to the VKI blade, experiencing subsonic flow conditions, is extracted from the work of Chappell et al. (2010) and implemented in the current facility.

The work presented in the current chapter follows the strategy described herein. First, the available experimental test facility in Concordia University is presented. Then, the work conducted to validate the facility and experimental methodology against the work of Chappell et al. (2010) is explained in details. Subsequently, the CFD model employed in Chapter 3 is re-generated here, and its accuracy and performance are assessed against the experimental measurements. Afterwards, a coolant flow optimization is conducted and the optimum solutions are analyzed via CFD and reproduced experimentally. The agreement in numerical and experimental results establishes the reliability of the present optimization methodology.

The current section presents the experimental wind tunnel facility that is employed throughout the research. The facility was previously developed by the thermal turbomachinery research group, as described in Hassan and Hassan (2012). The experimental methodology employed for film cooling measurements was established previously as well by Hassan and Hassan (2012). The current section describes the details of this experimental facility, the set-up, and methodology employed for film cooling investigations. The data reduction method is also explained. The next section presents the work conducted to validate the experimental set-up and methodology against the data of Chappell et al. (2010).

The wind tunnel is a facility combining mechanical, electronic, and thermography systems.

4.1.1. Mechanical system

The mechanical system comprises the mainstream and coolant air flow supply loops. It also includes flow meters, a heater, pressure gauges, and regulators. The mainstream and coolant flows are drawn from a compressed air tank that has a pressure regulated to 7 bars and a volume of 3.7 m^3. However, the air tank is not large enough to allow heating of the mainstream flow, therefore, the authors have opted to heat the coolant flow instead of the mainstream one. The coolant supply is thus equipped with an air heater that has a maximum capacity of 1.2 kW. A rectangular shaped plenum, sized 40 mm × 20 mm × 20 mm, is employed to ensure a uniform coolant flow prior to supplying it to the vane.

Both mainstream and coolant flow loops are equipped with control valves, pressure regulators, and flow meters. A divergent-convergent nozzle is installed in the mainstream flow path to eliminate any flow fluctuations. A fine grid mesh is placed at the exit of the nozzle to achieve a flow turbulence intensity of 8.5%.

4.1.2. Thermography system

The thermography system consists of a camera, a light source, a light supply, and a frame gripper. The camera is a 2CCD digital (IK-TF7C) Toshiba. It is used to capture images of the colored TLC sheet that is placed on the vane suction side. The images are captured at a rate of 5fps. A NI PCIE-1340 dual frame grabber transfers the captured images from the camera to a workstation. A fiber-optic light source of variable intensity supplies the required light to the TLC covered vane surface. The images captured of the TLC sheet are saved in a Tagged Image File Format (TIFF) with a size of 1024 × 768 pixels. Those images are colored with red, green, and

blue, and are therefore referred to as RGB images. An in-house Matlab code converts the RGB images to a temperature distribution using a calibration process.

4.1.3. Electronic system

The electronic system comprises a workstation and a data acquisition (DAQ) system. The workstation is a Pentium 4 Dell Precision with 3.75 GHz CPU, 3.25 GR of RAM and 250 GB hard drive. An M-series NI DAQ system captures pressure, flow, and temperature signals from all instruments. An in-house Labview code controls the timing of valves opening and closing and allows the recording of the flow properties and captured images.

4.1.4. Test section

The test section is a 2D linear cascade that is manufactured from a low conductivity transparent material to facilitate the imaging process. Side and top views of the test section are shown in Figure 4-2 and Figure 4-3, respectively. The cascade inlet cross section is 96 mm × 51 mm and the exit cross section is 29.5 mm × 51 mm. The cascade consists of one vane disposed in a linear arrangement with a vane pressure side and a vane suction side. The test vane chord length is equal to 72mm, and its pitch to chord ratio is 0.88. The span to chord ratio is 0.88. The vane achieves a flow turning angle of 62.75 degrees. Two staggered rows of axially oriented cylindrical film cooling holes are present on the vane suction surface. The vane is equipped with a total of thirteen holes. The first and second rows of holes are located on the suction side at distances of 15% and 25% of the axial chord, respectively. The vane is shown in Figure 4-3

A total of three vanes are manufactured; one for pressure measurements, one for TLC calibration, and one for film cooling tests. The vane used to measure the flow loading is manufactured with thirteen pressure taps on its surface, and is not equipped with the cooling

holes. The first pressure tap is located at the stagnation point to measure the stagnation pressure. The remainder of the pressure taps is distributed on the vane pressure and suction sides. Pressure tubes are installed through those pressure taps and connected to a pressure transducer. The latter is a DSA3217/16PX-10psid Scanivalve pressure transducer employed to measure the vane surface pressure. The isentropic flow assumption is then employed to calculate the isentropic Mach number distribution.

The vane used to calibrate the TLC sheet for proper temperature measurements has a groove of 50 mm × 50 mm × 0.36 mm on its suction side downstream of the cooling holes. The groove contains a heater (Omega, KH-608/205P) and a TLC sheet. The vane used for the film cooling tests has a groove of 50 mm × 50 mm × 0.20 mm to contain the TLC sheet only. Those grooves are created in order to minimize any flow disturbance resulting from the presence of the TLC sheet on the vane surface. In fact, the grooves allow the TLC sheet to become a part of the vane surface.

All vanes are manufactured from a low conductivity material named Acura 60 using Stero Lithography Rapid Prototyping technique. The thermal conductivity of the vane material is 0.21W/m·K and its thermal diffusivity is $0.13 m^2/s$.

4.1.5. TLC calibration

The TLC sheets used in the current study are narrow banded with a temperature range of [20^oC – 25^oC]. A heater with a maximum power of $0.78 W/cm^2$ supplies a uniform heat flux to the TLC sheet during the calibration process. T-type thermocouples are used to capture the vane surface temperature. The calibration process consists of slightly increasing the power supplied to the

heater for a total of N incremental steps, waiting an appropriate time period to achieve steady state, capturing N RGB images, and recording the corresponding surface temperature.

4.1.6. Data reduction

Resolving the one-dimensional heat conduction equation,

$$\rho c_p \frac{\partial T}{\partial t} = \frac{\partial}{\partial x}\left(k \frac{\partial T}{\partial x} \right) \tag{4-1}$$

while using the boundary conditions shown below,

$$\left.\begin{array}{c} \text{at } t = 0,\ T = T_{initial} \\ \text{at } x = 0,\ h\left(T_w - T_f\right) = -k \dfrac{\partial T}{\partial x} \\ \text{at } x = \infty,\ T = T_\infty = T_{initial} \end{array}\right\} \tag{4-2}$$

and applying the semi-infinite solid assumption, yields the system temperature as a function of the heat transfer coefficient and the thermal properties of the vane material:

$$\frac{T_w - T_{initial}}{T_f - T_{initial}} = 1 - \exp\left(\frac{h^2 \alpha t}{k^2} \right) erfc\left(\frac{h\sqrt{\alpha t}}{k} \right) \tag{4-3}$$

The wall temperature (T_w) and the initial temperature ($T_{initial}$) are measured using the TLC sheet. The mainstream temperature (T_∞) is measured using the thermocouples.

Furthermore, the film temperature is obtained from the cooling effectiveness equation below:

$$T_f = \eta T_c + T_\infty (1 - \eta) \tag{4-4}$$

Equations (4-3) and (4-4) are reduced to one equation in two unknowns h and η as follows:

$$T_w - T_{initial} = \left[1 - \exp\left(\frac{h^2 \alpha t}{k^1}\right) erfc\left(\frac{h\sqrt{\alpha t}}{k}\right)\right] \cdot \left[\eta\left(T_c - T_\infty\right) + T_\infty - T_{initial}\right] \quad (4\text{-}5)$$

A single transient test of 60 seconds is conducted to capture a total of 300 images at a rate of 5Hz. These images are used to solve equation (4-5) by applying the non-linear least square regression method for the two unknowns h and η. Further details concerning the solution methodology is provided by Hassan and Hassan (2012).

Uncertainty analysis is based on 95% confidence level and is conducted using the methodology of Kline and McClintock (1953). The average uncertainties that are estimated for measured temperatures (thermocouples and TLC), flow rate, pressure, thermal diffusivity, and thermal conductivity, are; $\mp$ 2%, $\mp$ 3%, $\mp$ 3%, $\mp$ 2% and $\mp$ 3%, respectively. The corresponding uncertainties in blowing ratio, Mach number, η, and h are; $\mp$ 6%, $\mp$ 5%,$\mp$ 8% and $\mp$ 12% respectively.

4.1.7. Test facility validation

The test facility and methodology are validated against the experimental work of Chappell et al. (2010). In effect, all geometric and flow parameters in the reference work of Chappell et al. (2010) are considered and applied while manufacturing and testing the current test section. Chappell et al. (2010) applied the transient Infra-Red (IR) thermography technique throughout their investigations while the transient TLC technique is used in the present study. Furthermore, Chappell et al. (2010) applied density ratios from 1.73 to 1.92 by employing foreign gases. However, due to space and cost limitations, the density ratio considered in the present study is close to unity. Nonetheless, previous investigations showed that the effect of density ratio on the

cooling performance is limited to cases of low blowing ratios, and is not significant otherwise, Wright et al. (2011).

A pressure scanner is used to scan the pressure distribution around the vane in order to determine the surface isentropic Mach number distribution. The latter is presented in Figure 4-5 and compared to the reference work of Chappell et al. (2010). The agreement between the two studies is deemed to be good on both pressure and suction sides except for the region on the suction side between s/C_x = 50% and s/C_x = 70%. This particular discrepancy between the two experimental datasets is attributed to a slight dissimilarity in surface curvature in this region of the vane. The present agreement in isentropic Mach number distribution around the vane surface is deemed to be good for the purpose of the present study.

The laterally averaged film cooling effectiveness is measured and compared to the values of the reference study for several blowing ratios. The comparisons are presented in Figure 4-6 and exhibit a good agreement between the two measured datasets of film cooling effectiveness. The agreement in the case of BR = 1.2 is good over the entire area downstream of the cooling holes. For BR = 0.9 the agreement deteriorates after $x/D > 30$. In the case of BR = 0.6 the agreement deteriorates after $x/D > 20$. The discrepancies observed between the two datasets of film cooling effectiveness distribution are attributed to the effect of using a unity density ratio in the present study as opposed to density ratios varying from 1.73 to 1.2 in the reference work. In fact, the effect of density ratio is significant at low blowing ratios, and that effect decays with increasing blowing ratio. The previous observations confirm that the current test facility and methodology are suitable for film cooling investigations.

4.2. CFD model

The experimental results obtained in the Concordia wind tunnel are reproduced numerically using the commercial software ANSYS CFX v.12.1. The computational domain that is constructed consists of the mainstream, the plenum, and the cooling holes. The geometric details of the domain are consistent with the present work experimental test section, namely the airfoil geometry, and the cooling hole geometry. Similarly to the present experimental work, only one vane is simulated. The inlet to the CFD domain is placed four and a half chords upstream of the leading edge of the vane, and the exit is placed two chords downstream of the trailing edge.

In accordance with the present experimental work, a stagnation pressure of 116,800 Pa, stagnation temperature of 296K, and a turbulence intensity level of 5% are specified at the inlet boundary to the free-stream along with a flow direction of 0^o. A static pressure of 109,000 Pa is specified at the outlet boundary to match the exit isentropic Mach number of 0.34 as in the present work experiments. The blade, plenum, and cooling tubes walls are defined as adiabatic. No-slip wall boundary conditions are also prescribed at all surfaces.

Periodic boundary conditions are set along the mid-pitch line to model an infinite cascade in the *y* direction. Only one full hole pitch is modeled in the spanwise (z) direction. Periodic boundary conditions are applied at the center of the two adjacent film holes in the second row of holes. This effectively models a blade with an infinite span. The cooling holes are located at 15% and 25% of the axial chord, respectively. The geometry of the simulated CFD domain, blade, and cooling holes is presented in Figure 4-7. The main geometric and flow parameters of the vane cascade are summarized in Table 4-1 and Table 4-2 respectively.

The inlet boundary to the plenum is located at the planar side (parallel to the *x*-axis) of the plenum. The boundary conditions at the inlet of the plenum consist of a total pressure value, a static temperature of 325K, as well as a turbulence intensity level of 1%. No slip wall boundary conditions are applied at the plenum and cooling tubes walls. The plenum inlet total pressure is iteratively adjusted to match the present work experimental blowing ratio.

A multi-block hybrid mesh is constructed in ICEM CFD v12.1. The computational domain is divided into several blocks to allow more control over the grid quality and density. An O-grid is wrapped around the airfoil. An exponential bunching law is used inside the boundary layer. The distance of the first grid node away from the vane surface normalized by the blade chord (*y/C*) is set to $1 \cdot 10^{-4}$. An element growth ratio from the wall of 1.1 is used. The clustering of the elements near the vane surface yields a non-dimensional wall distance (y^+) below unity. An H-mesh is employed for the remaining of the mainstream flow. The entire mainstream is meshed using hexahedral elements. As for the plenum and cooling hole tubes, tetrahedral elements are used with prism layers clustered at the walls of the plenum and cooling hole tubes to obtain a y^+ below unity. Figure 4-8 and Figure 4-9 present the details of the hybrid mesh in the *xy* plane. O-grids are also wrapped around the cooling hole exits to allow a higher level of refinement. And an exponential clustering of elements towards the exit of the holes is used. Details of the clustering around the hole exit is shown in Figure 4-10. The mesh on either side of the cooling hole exit does not match since the plenum side consists of tetrahedral elements and the mainstream side consists of hexahedral elements. A general grid interface connection, provided by CFX, is used between the two overlapping meshes, ANSYS *User Guide*. Details of the computational mesh interface at the exit of the cooling hole are shown in Figure 4-11.

RANS simulations are conducted using the commercial software ANSYS CFX v12.1 to resolve the flow field and obtain the vane surface adiabatic wall temperature distribution. The numerical predictions are compared to the present work experimental data to validate the CFD model. The SST turbulence model is used for turbulence closure. Convergence of the present simulations is established when the following three criteria are met:

- The root mean square of the normalized residual of the mass, momentum, and energy equations is reduced to $10^{-4.}$
- The integral mass and energy imbalances of the entire flow domain fall below 10^{-5}.
- Target values that are being monitored reach a steady solution that is no longer changing with successive iterations.

A single CFD simulation reaches convergence in about 1500 to 2000 iterations Each computation is subdivided into 4 or 6 tasks and performed on the Concordia HP parallel computing cluster which consists of AMD Opteron processors (x86, 64 bit, dual core). Convergence requires typically a total wall clock time of about 4 days.

The present CFD model is used subsequently to predict the aero-thermal cooling performance, which is measured in terms of the adiabatic film cooling effectiveness (η) and the mass-averaged total pressure loss coefficient (AL).

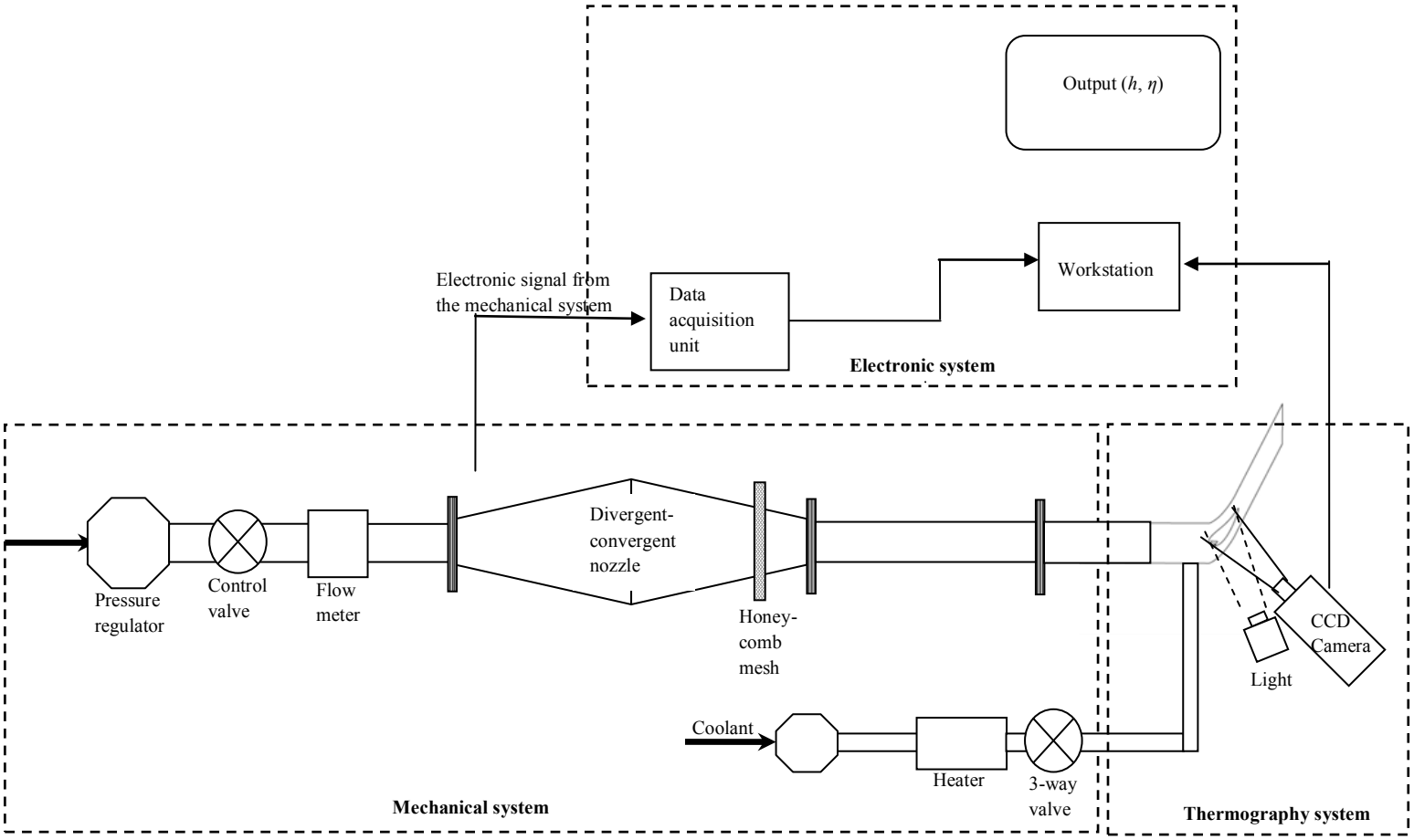

Figure 4-1: Top view schematic of the experimental facility, Hassan and Hassan (2012)

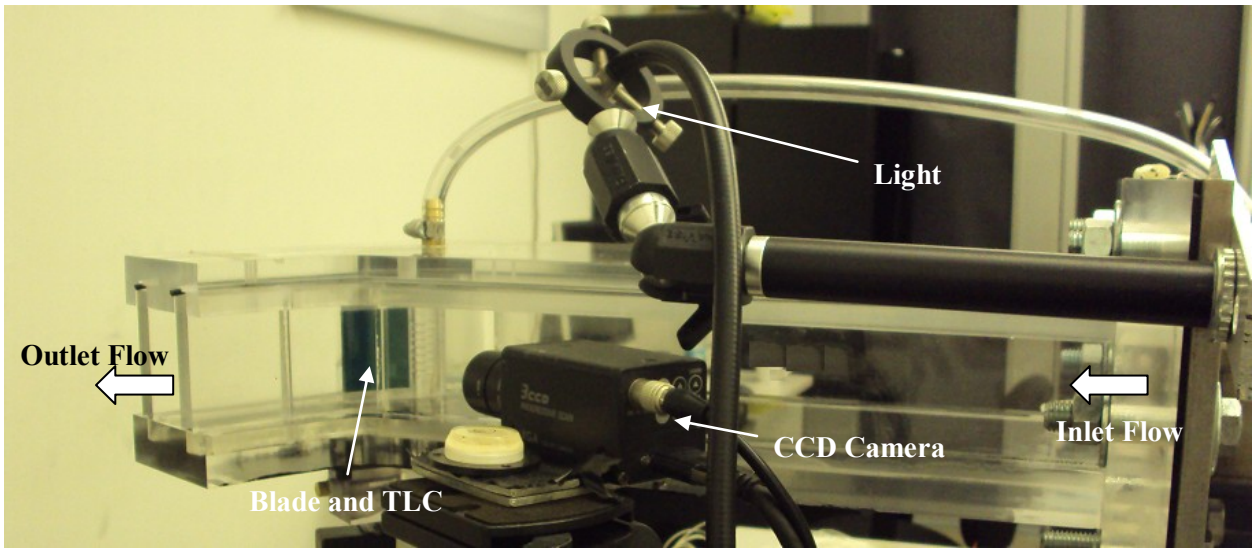

Figure 4-2: Side view of the test section, Elnady et al. (2011)

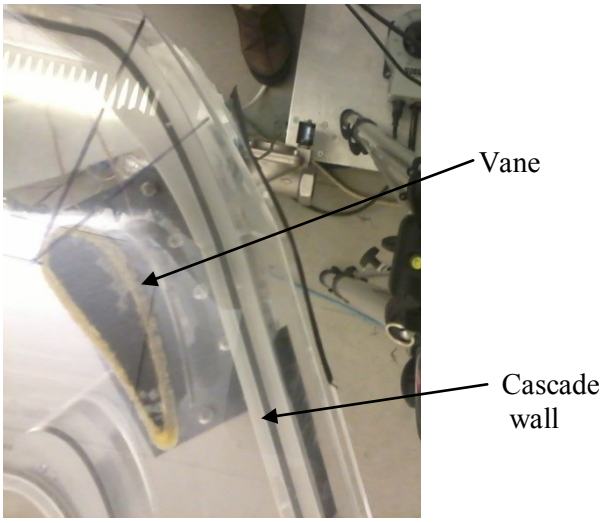

Figure 4-3: Top view of the test section

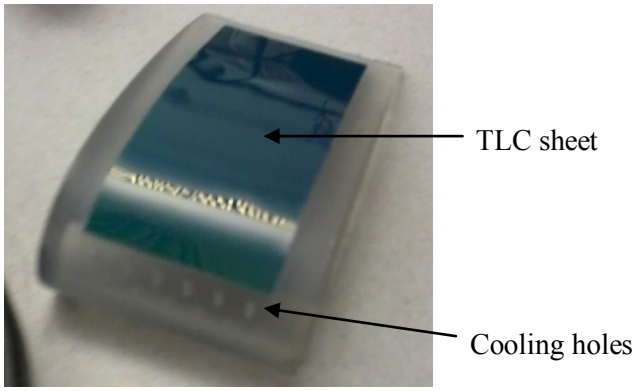

Figure 4-4: Tilted top view of the test vane

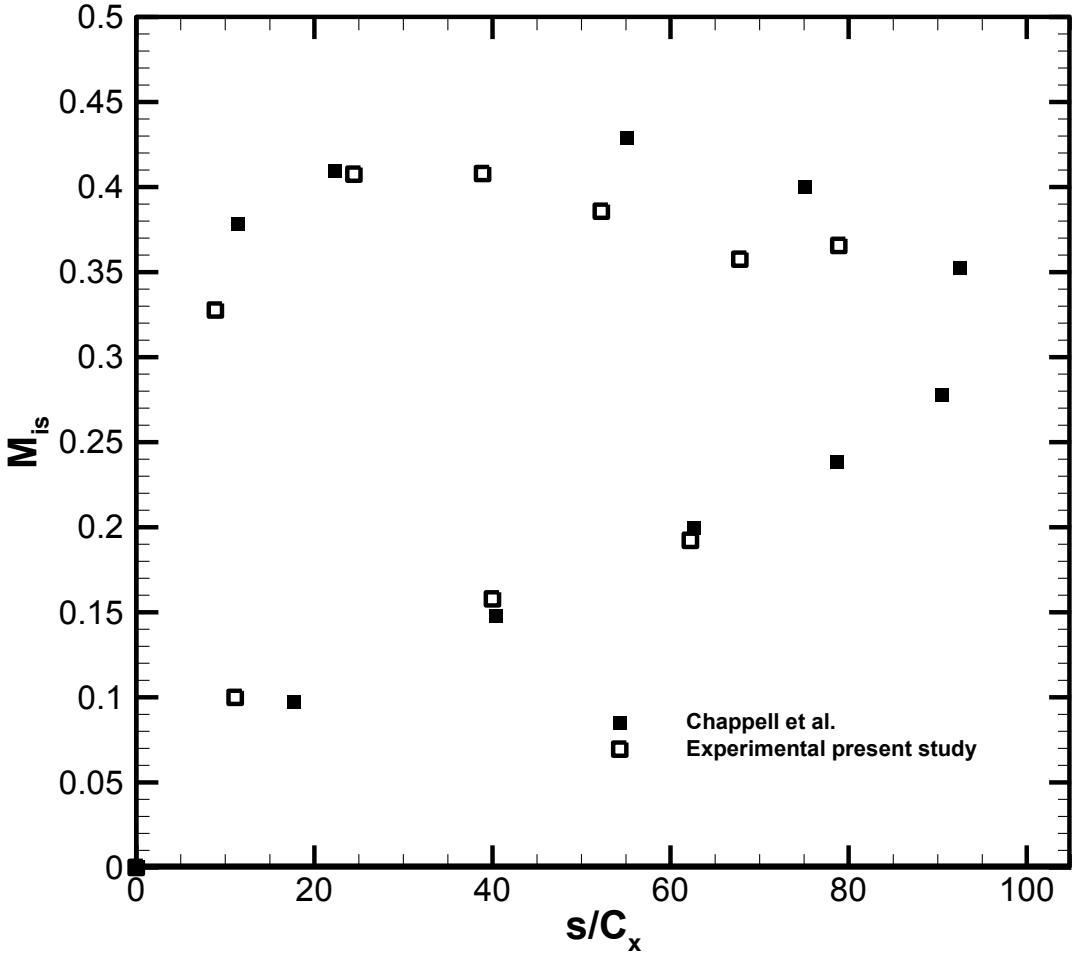

Figure 4-5: Isentropic Mach number distribution at the vane mid-span obtained with the current experimental work and the reference work

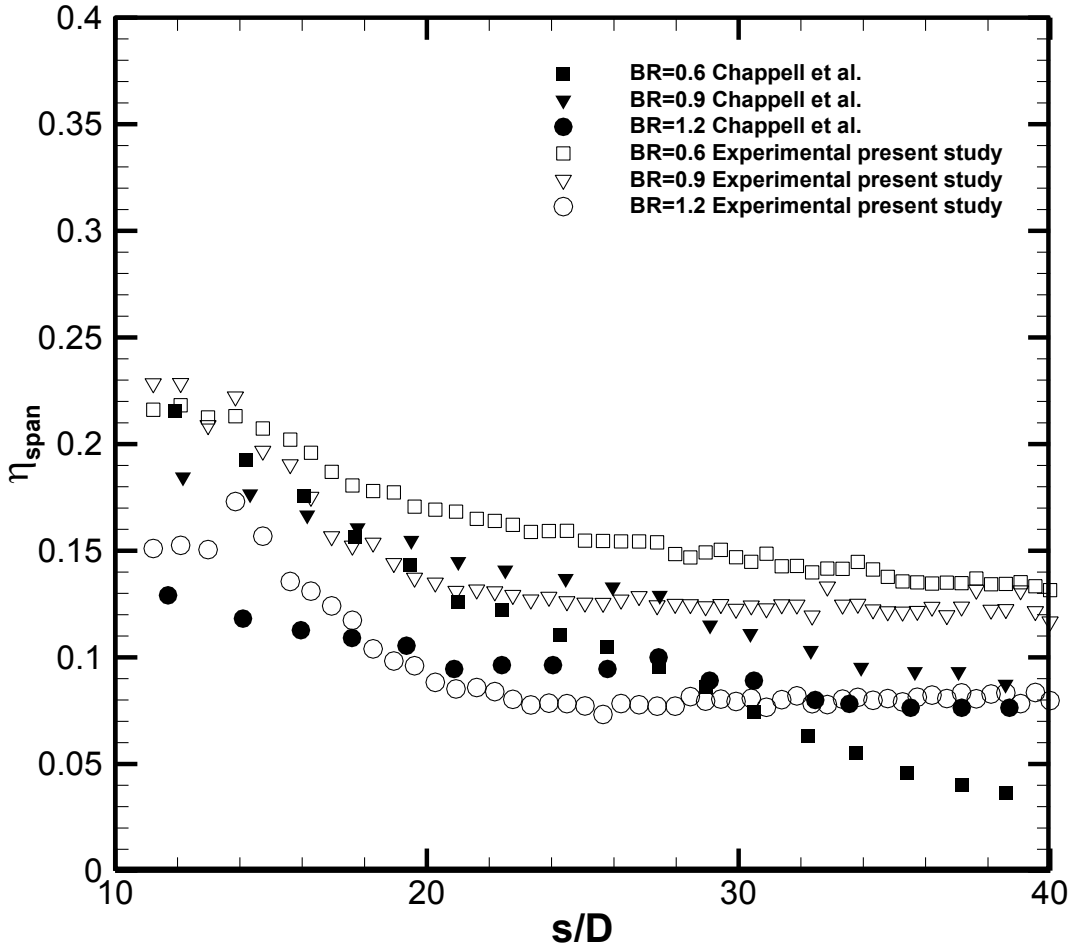

Figure 4-6: Laterally averaged adiabatic effectiveness distribution obtained with the current experimental work and the reference work

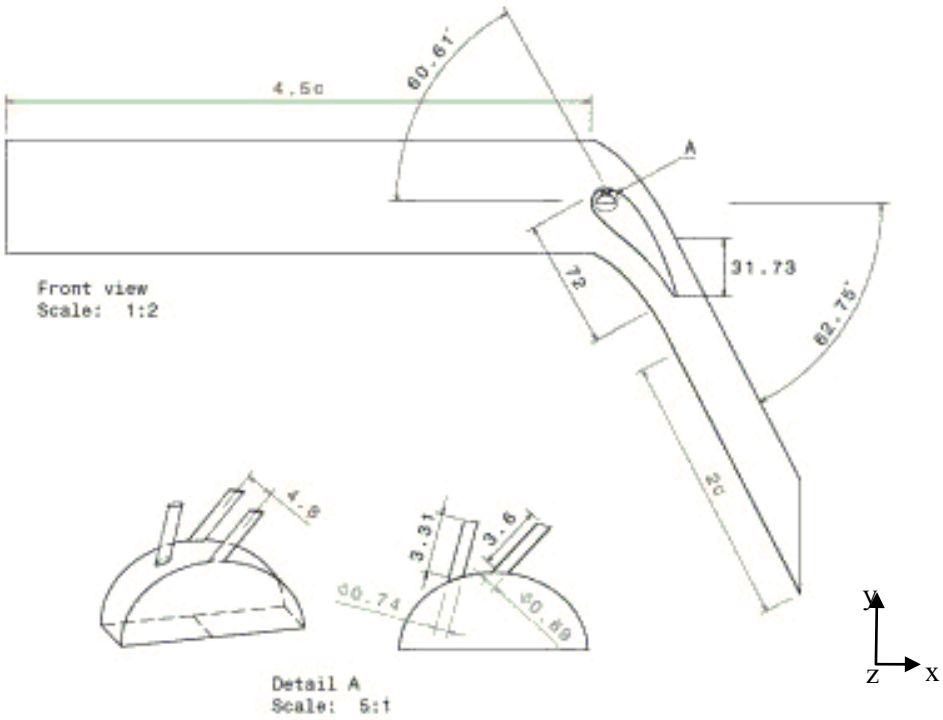

Figure 4-7: 2D details of the vane and the film cooling configuration

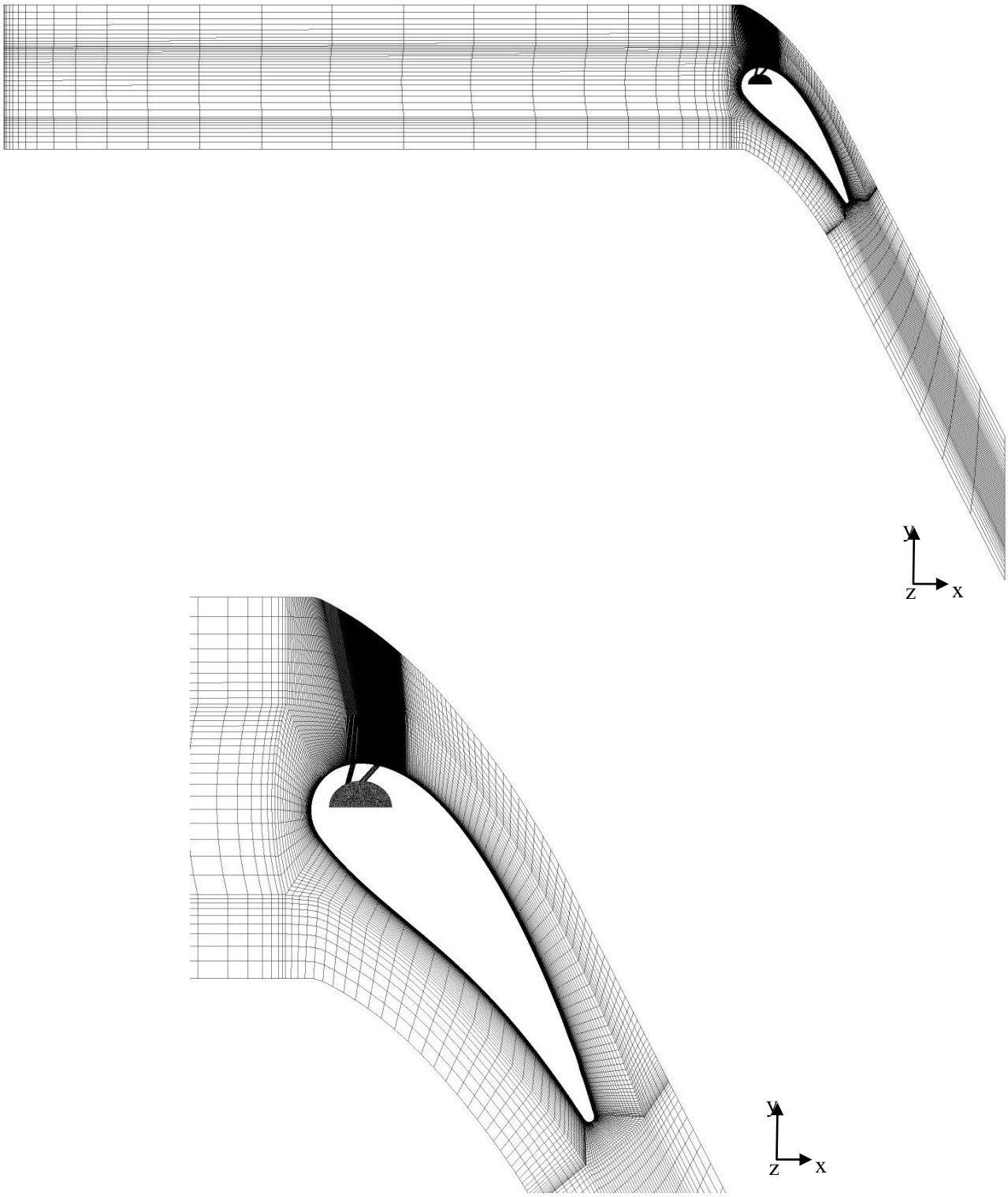

Figure 4-8: Details of the computational grid in the mainstream and around the vane

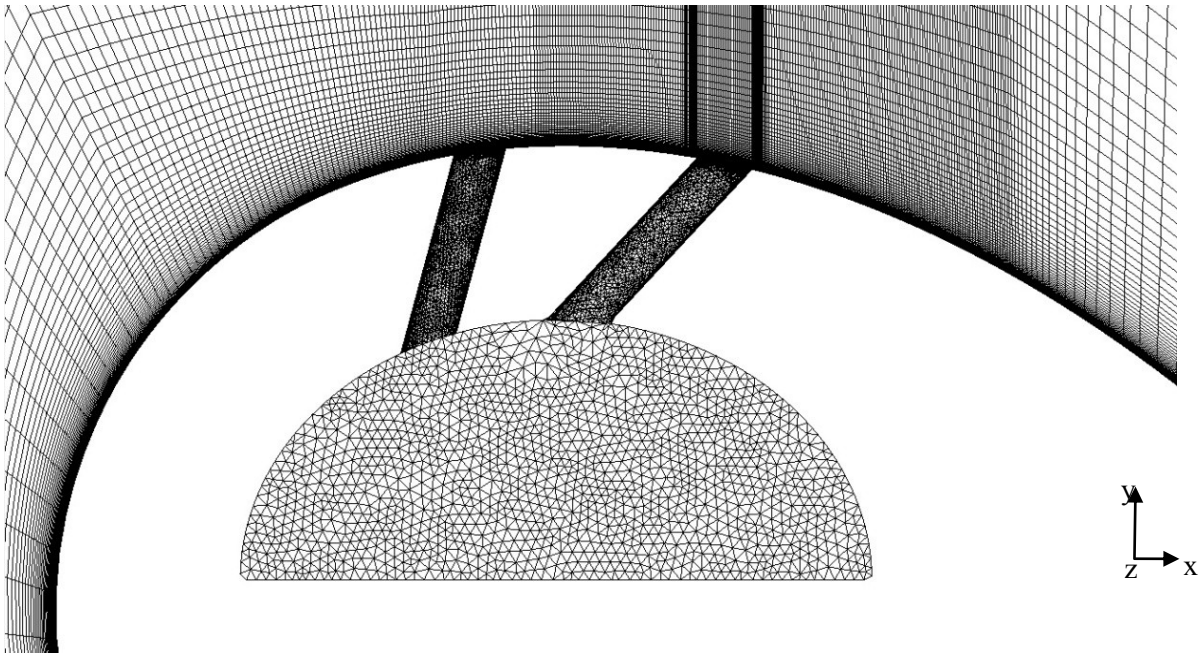

Figure 4-9: Details of the computational grid inside the coolant plenum and at the vane wall

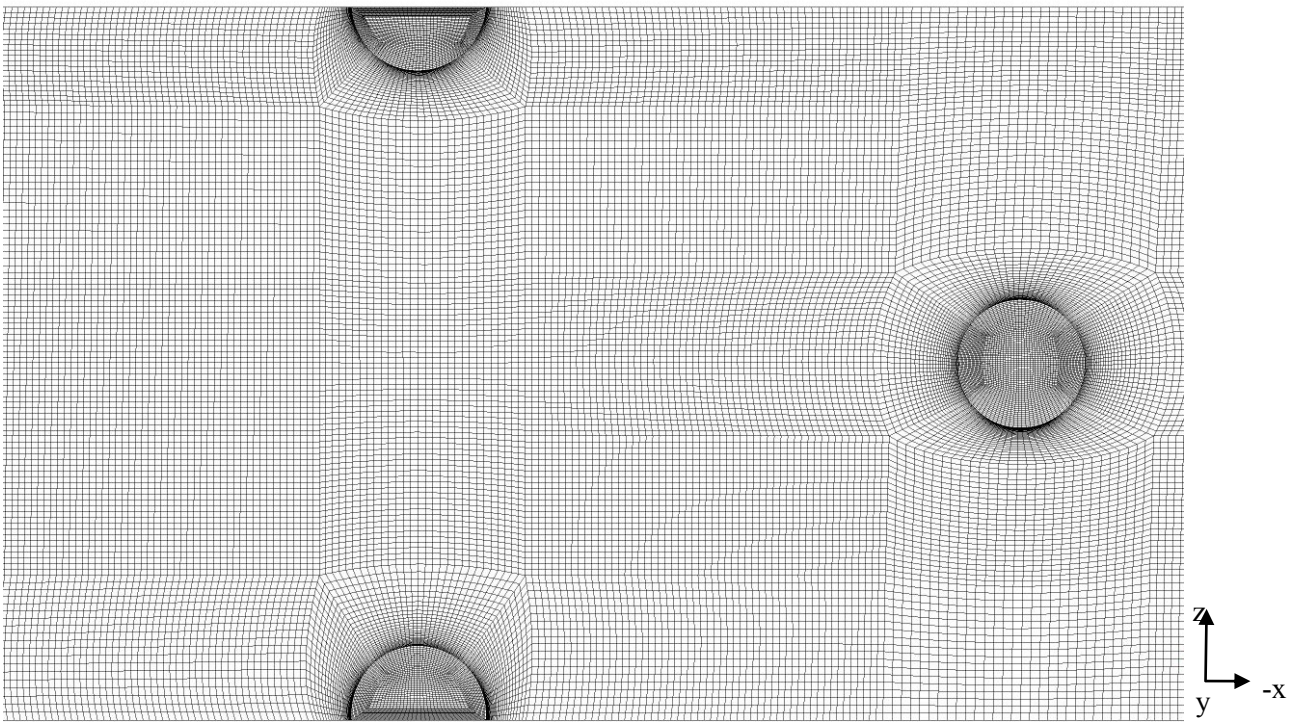

Figure 4-10: Details of the clustering of elements around the holes' exits

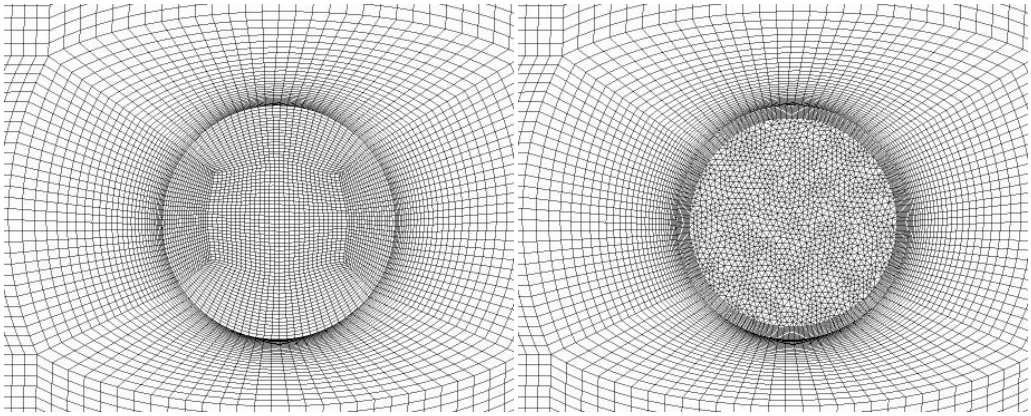

Hexa mesh side **Tetra mesh side**

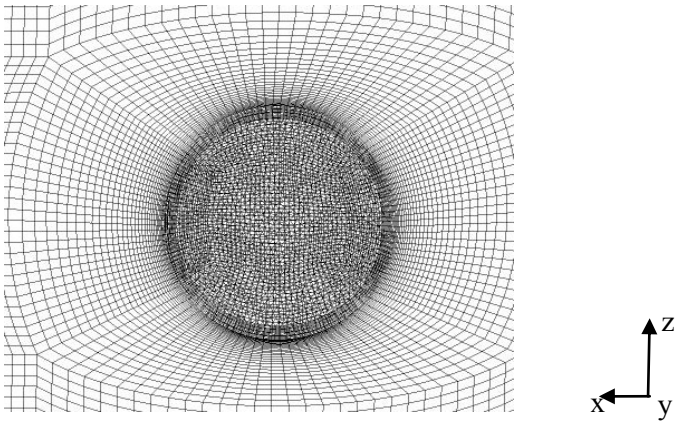

Hexa/tetra mesh interface

Figure 4-11: Close-up on the general grid interface (tetra/hexa) at the hole exit

Table 4-1: Main geometric parameters of the vane cascade

True chord length [mm]	72
Axial chord [mm]	48.5
Span [mm]	63.5
Stagger angle	60.61
Pitch [mm]	63.5
Inlet flow angle	0^{o}
Outlet flow angle	62.75^{o}

Table 4-2: Main flow parameters of the vane cascade

M_{in}	0.13
$p_{e\infty} / p_{0in,\infty}$	0.933
T_{in} [K]	294.1
Tu_{in}	5%
Re_C	$2.61 \cdot 10^5$
$M_{e,is}$	0.34

Prior to the optimization work, assessment work is conducted to confirm the reliability of the CFD model to be used as a tool for computation of the optimization objective function. The same CFD model is used for validation and optimization work.

The vane surface distribution of isentropic Mach number is presented in Figure 4-12. The CFD prediction of isentropic Mach number is obtained with the SST turbulence model and compared with the present work experiments. The isentropic Mach number is plotted versus the non-dimensional curvilinear distance from the leading edge of the first row of holes. The prediction of the isentropic Mach number distribution presents very satisfactory agreement with the present experimental work.

Literature holds many numerical studies that have assessed the accuracy of various turbulence models in predicting film cooling performance. However, no general consensus has yet been reached for a turbulence model that could be applied to all film cooling applications. Previously in Chapter 4, the SST turbulence model was shown to be reliable for predicting the airfoil surface heat transfer coefficient, and consequently assumed to predict accurately the adiabatic film cooling effectiveness. In the present chapter, the capability of two-equation eddy viscosity models in predicting the adiabatic cooling effectiveness is evaluated directly and assessed against experimental data obtained in the test facility of Concordia University. The turbulence models investigated in the present study include the Shear Stress Transport (SST) model, the standard k-ε model, the RNG k-ε, and the k-ω. The cooling performance is found, in fact, very sensitive to turbulence modeling. This is particularly true close to the cooling holes. An accurate depiction of the interaction occurring between the coolant and mainstream flows relies highly on turbulence modeling and clustering of mesh elements through the film cooling hole and around the cooling hole exit.

Figure 4-13 presents the laterally averaged adiabatic cooling effectiveness obtained with four different turbulence models and compares these predictions to the present work experimental data. The comparison is performed at BR = 0.9. The cooling effectiveness is plotted versus the non-dimensional curvilinear distance from the leading edge of the first row of holes. In comparison to our present experimental work the cooling performance is significantly under-predicted with the standard k-ε model. In fact, the model fails to depict the effectiveness trend over the entire surface of the vane. The three remaining models, the standard k-ω, the RNG k-ε, and the SST seem to predict effectiveness magnitudes that are closest to the experimental values. In the near-hole region, i.e. between s/D = 10 and s/D = 30, all three models predict a coolant jet detachment from the vane surface followed by an immediate re-attachment. This does not agree with the experimental data. Furthermore, coolant re-attachment is indicated by a peak effectiveness value in the near-hole region, and the standard k-ω model over-predicts the effectiveness by a maximum of 60% at s/D = 18. The RNG k-ε model over-predicts the effectiveness by a maximum of 46% at s/D = 20. The SST model over-predicts the effectiveness by a maximum of only 28% at s/D = 23. As for the far-field region, i.e. between s/D = 30 and s/D = 40, the standard k-ω and the RNG k-ε provide very similar effectiveness distribution trends. Their effectiveness magnitudes are in close agreement to the experimental one. However, the general trend of the distribution provided by the two models, k-ω and RNG k-ε, does not match the experimental one on the entire vane surface. The SST model, on the other hand, seems to provide the most reasonable agreement with the experimental effectiveness distribution particularly in trend as the decreasing slope of the effectiveness curve is very similar to the experimental one.

Further investigations are conducted at BR = 0 .6 and BR = 1.2, Figure 4-14. The SST provides effectiveness distributions closest in magnitude to the experimental ones particularly at BR = 1.2. At BR = 0.6, between *s/D* = 15 and *s/D* = 40 both models predict the same continuously decreasing trend in very close agreement to the experimental data. However, at BR = 0.6, the SST model predicts a fully attached coolant jet to the vane surface in accordance with the experimental data. The RNG *k-ε* fails to predict the same coolant behavior. In effect, between *s/D* = 11 and *s/D* = 15, the RNG *k-ε* predicts an increasing trend in effectiveness that reaches a peak at *s/D* = 15. This increasing trend is an indication of a slight coolant detachment followed by a re-attachment to the vane surface. The RNG *k-ε* predicts coolant detachment at BR = 0.6 where experimental data clearly indicates that the coolant jet is well behaved and fully attached. An accurate depiction of the coolant behavior at the exit of the hole is crucial when selecting a turbulence model, because the cooling performance of a discrete film-cooling scheme is highly dependent on the behavior of the coolant exiting the hole. The RNG *k-ε* model is therefore deemed inappropriate for predicting the cooling performance of the present film cooling scheme.

The SST model is therefore chosen in the present study because of its superior performance in predicting the effectiveness in the near-hole region and the far field at all investigated blowing ratios. It is found most reliable in predicting the laterally averaged adiabatic film cooling effectiveness trend and is used for all subsequent CFD simulations in the present study.

A mesh sensitivity analysis is performed at BR = 0.9, Figure 4-15. This particular BR is chosen for the grid study because severe lift-off is observed in the CFD results when the mesh density is coarse, as opposed to experiments that show the coolant jet to be well-behaved and fully attached to the vane surface. The grid study reveals that the clustering of the elements around the hole exit is crucial for obtaining a reasonable prediction of the coolant jet ejection out of the cooling hole.

Therefore, an exponential clustering is used around the hole exit, with a minimum node spacing at the hole exit *(x/D)* of 5.10^{-3}. Figure 4-15 compares the adiabatic cooling effectiveness distributions using four different meshes at BR = 0.9. All meshes are identical in topology. The essential differences between all meshes consist of the number of elements in the streamwise *x* direction and around the hole exit, the minimum node spacing at the hole exit, and the minimum node spacing in the vertical direction at the blade surface. The first mesh presented in Figure 4-15 is composed of 4.8 million elements, the second consists of 5.4 million elements, the third amounts to 6.2 million elements, and the last has 7.9 million elements. The study shows that mesh refinement systematically reduces the severity of the jet lift-off as the peak effectiveness is brought further upstream towards the cooling holes. The mesh composed of 5.4 million elements is deemed accurate enough to provide mesh independent numerical results at a reasonable computing time.

The final step towards a fully verified CFD model is to compare the predicted objective functions with the ones that are measured experimentally. Table 4-3 offers a comparison of the aerodynamic loss (*AL*), and the surface averaged effectiveness (η_{surf}) predicted by CFD at BR = 0.3, 0.6, 0.9, and 1.2 against their experimental counterparts. Both *AL* and η_{surf} are normalized with respect to their maximum and minimum values within the design space shown in Table 4-4. This allows a reliable comparison between results obtained experimentally and those obtained numerically. We can see that the CFD simulations provide predictions of *AL* and η_{surf} with a very reasonable accuracy; one that is not over shadowed by the error involved in the discretization of the governing flow equations (10^{-04}). In fact, *AL* predictions are within 20% of experimental data. The η_{surf} predictions are within 34% of the experimental data. The discrepancy between predictions of η_{surf} and experiments increases with increasing blowing ratio.

This is attributed to the turbulence model limitations in resolving the coolant flow when lift-off occurs. Both experiments and CFD provide the same trend in results. At BR = 0.6 both experiments and CFD yield the highest η_{surf}, whereas at BR = 1.2, experiments and CFD yield the lowest η_{surf}. As for AL, it decreases with decreasing BR. The CFD model presented herein is therefore considered reliable enough to provide predictions of the film cooling performance and the aerodynamic loss. It is therefore deemed a reliable tool for estimating the optimization objective functions, namely the cooling function, the aerodynamic function, and the single objective function.

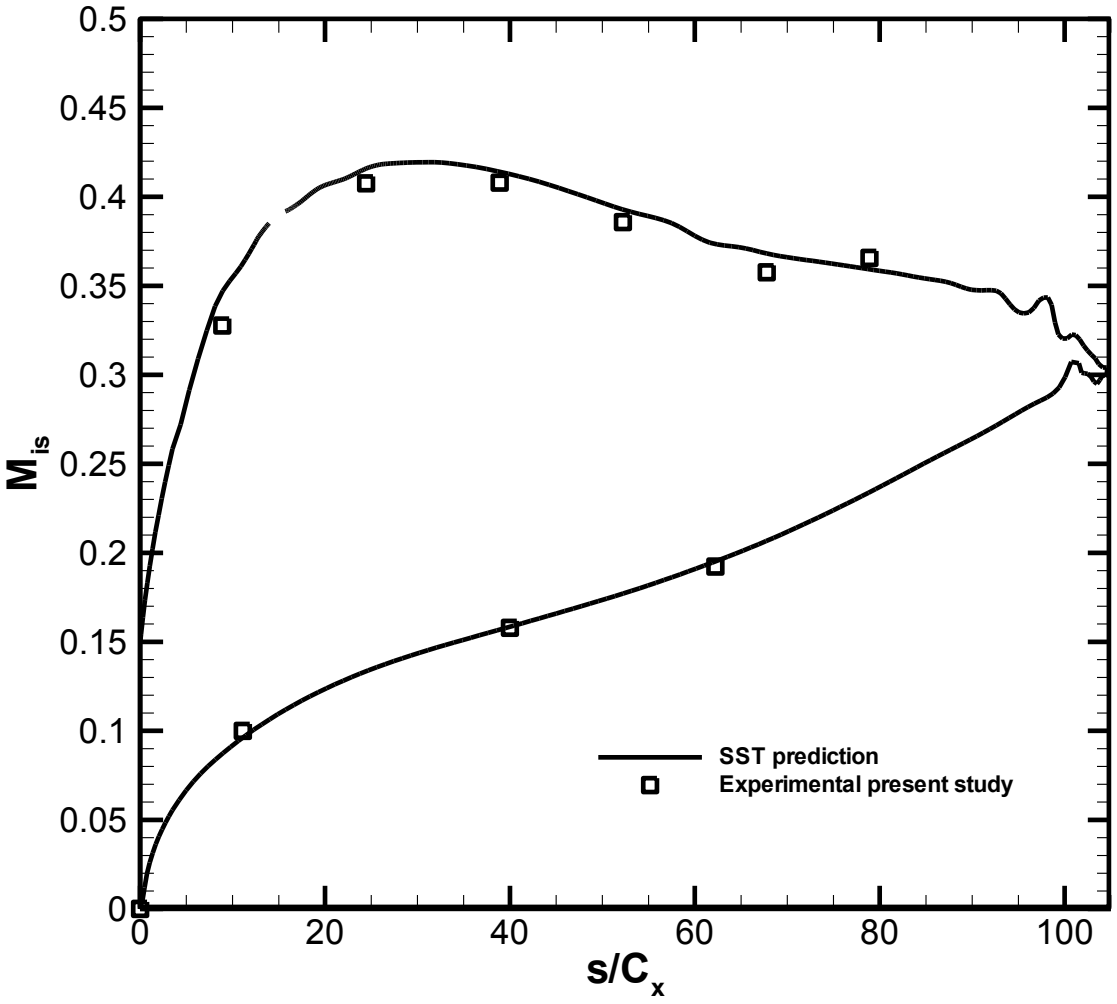

Figure 4-12: Isentropic Mach number distribution at the vane mid-span predicted by CFD using the SST model

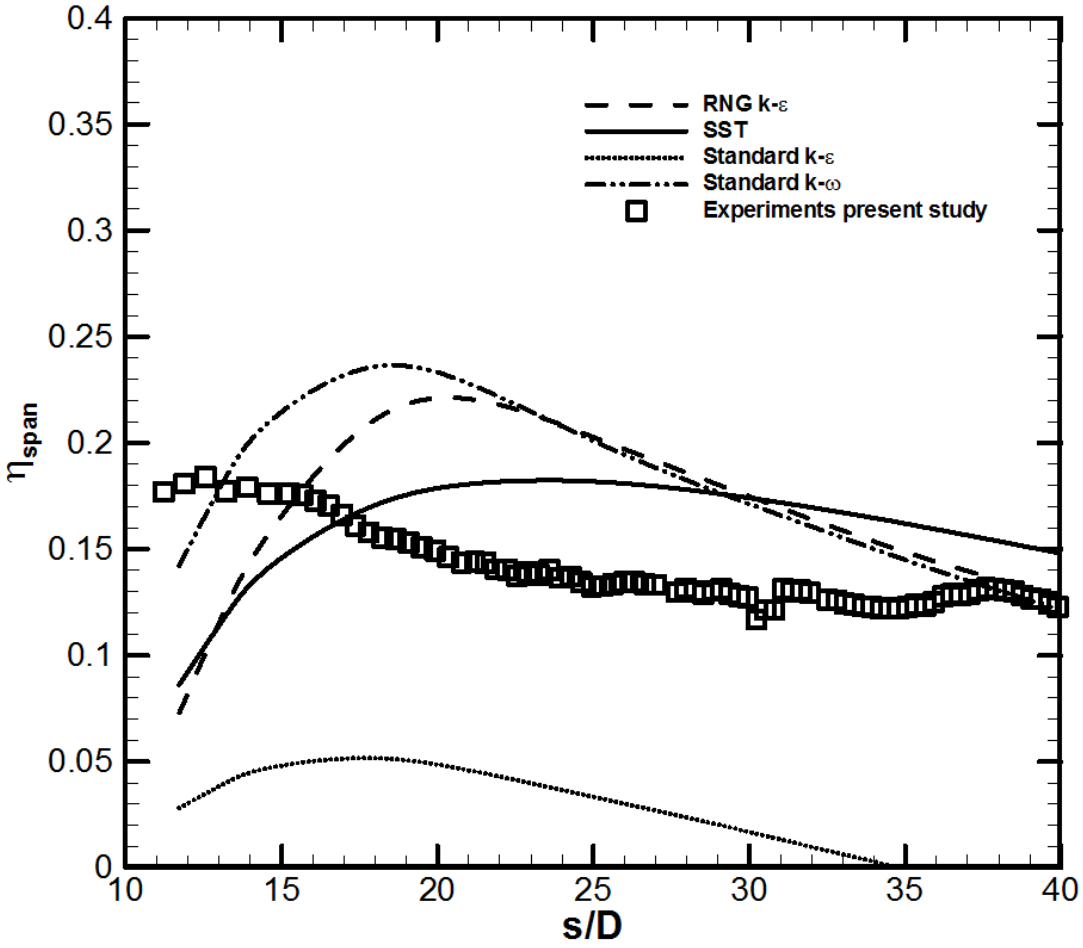

Figure 4-13: Sensitivity of laterally averaged adiabatic cooling effectiveness prediction to turbulence modeling at BR = 0.9

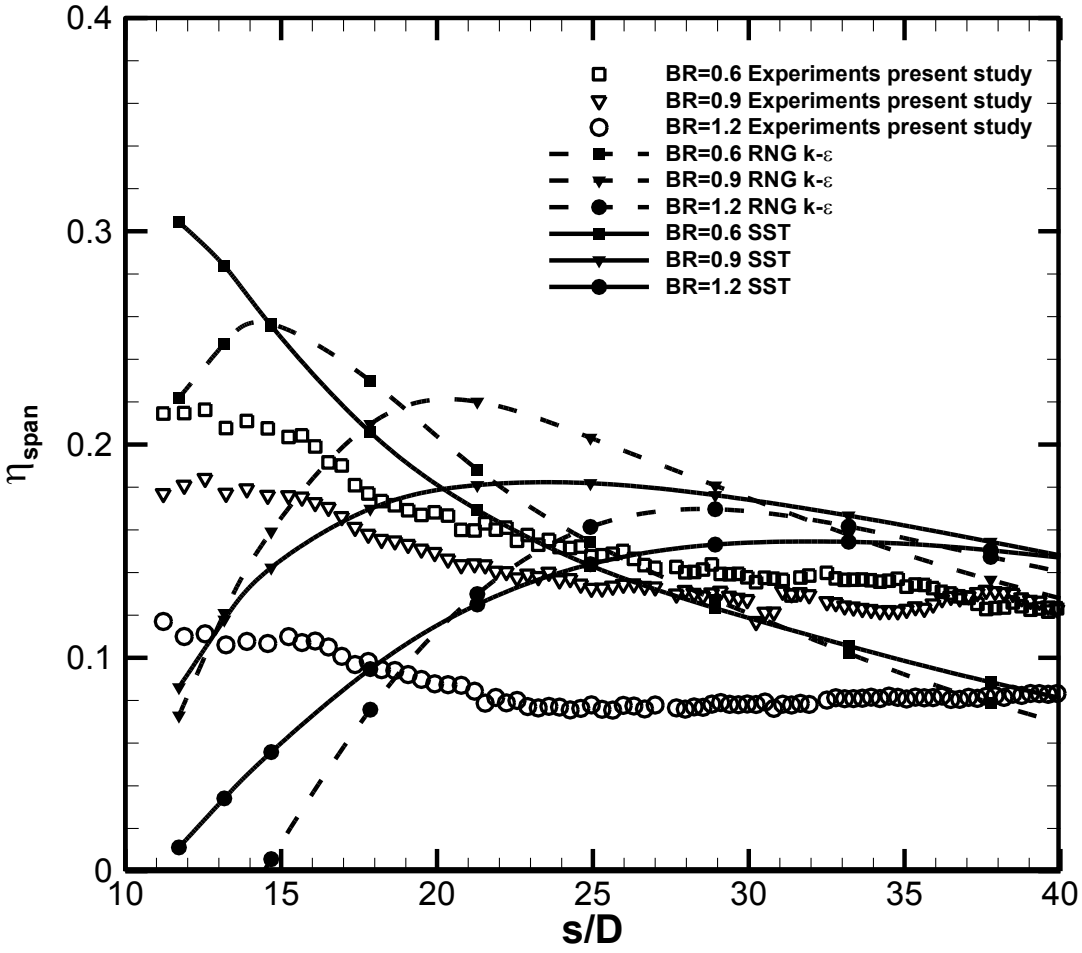

Figure 4-14: Predictions of laterally averaged adiabatic cooling effectiveness at varying BR using RNG *k-ε* and SST models

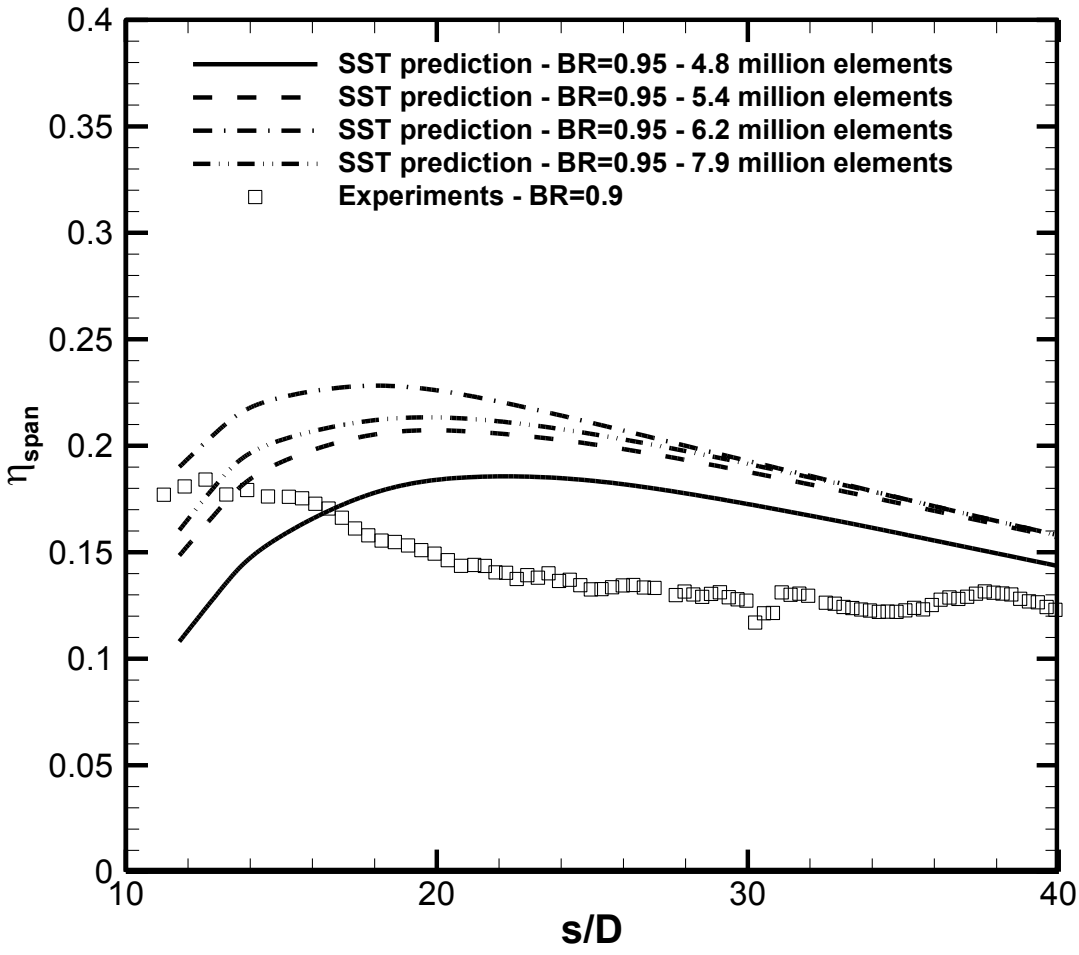

Figure 4-15: Sensitivity of laterally averaged adiabatic effectiveness prediction to mesh refinement

4.3. Multiple objective optimization on the vane suction side

The design space constituted by the lower and upper limits of the design variables is shown in Table 4-4. Ten design candidates are selected by Latin Hypercube Sampling (LHS). Numerical predictions are performed at these ten design candidates and the results are presented in Table 4-5. The table provides the numerical predictions of AL, and η_{surf}. Both are normalized with respect to their maximum and minimum values within the design space. This facilitated the comparison between the numerical and experimental results.

The multiple objective optimization is characterized by two objective functions that are simultaneously and independently optimized using the Non-dominated Sorting Genetic Algorithm, the so-called NSGA-II developed by Deb (2001). The non-dominated sorting procedure employed in the optimization ensures that no solution on the Pareto-front is superior to any other solution on the same front. Each GA generation consists of 100 individuals, and the optimization stopped after 70 generations. The values of crossover and mutation probabilities are 0.7 and 0.15, respectively. Two elite individuals are transmitted from one generation to the next.

The Pareto optimum solutions computed using the ANN-based NSGA-II, are shown Figure 4-16 forming the Pareto front, which is composed of all the optimum design points that could be obtained using the single objective optimization approach. It is a concave curve of the thermal objective function, given by $(1-\eta_{surf})$, vs. the aerodynamic objective function, given by AL. The front represents the competing nature of the two objectives, where any improvement in aerodynamic loss results in deteriorating the film cooling performance and vice-versa. This Pareto front allows the designer to make a choice as to which way to go: get a better thermal performance at the expense of a higher aerodynamic loss, or have a compromise between the two, etc.

The extreme right end of the front corresponding to the point (x = 0.493; y = 0.283) on the Pareto curve is characterized by a minimum (1-η_{surf}) or an otherwise maximum cooling performance, and a maximum AL or an otherwise worst aerodynamic performance. This point can be denoted as the thermal optimum. The point (x = 0.473; y = 0.2880) on the Pareto curve corresponding to the extreme left end is characterized by a minimum AL or an otherwise best aerodynamic performance and a maximum (1-η_{surf}) or an otherwise minimum cooling performance. This point can be denoted as the aerodynamic optimum.

Both thermal and aerodynamic optima can be obtained with a single objective optimization provided the user defined weights are set appropriately.

Table 4-3: Comparison of experimental and CFD objective functions

	Experimental present work		CFD present work	
BR	η_{surf}	***AL***	η_{surf}	***AL***
0.3	0.641	0.333	0.648	0.472
0.6	0.731	0.410	0.833	0.492
0.9	0.544	0.481	0.367	0.508
1.2	0.153	0.618	0.016	0.518

Table 4-4: Design space and design variables

Design variable	Lower bound	Upper bound
$p_{0c}/p_{0\infty}$	0.92	1.07
T_c/T_∞	1.08	1.13

Table 4-5: Initial design points selected by LHS

Design Candidate	Input from LHS		CFD Output		
	$p_{0c}/p_{0\infty}$	T_c/T_∞	η_{surf}	***AL***	**BR**
1	1.062	1.082	0.005	0517	1.117
2	1.032	1.122	0.192	0.508	0.984
3	1.002	1.112	0.637	0.502	0.838
4	0.957	1.107	0.873	0.489	0.587
5	1.017	1.097	0.449	0.505	0.929
6	0.972	1.092	0.767	0.494	0.679
7	1.047	1.102	0.436	0.514	1.040
8	0.942	1.127	0.556	0.479	0.477
9	0.987	1.117	0.771	0.498	0.755
10	0.927	1.087	0.596	0.476	0.397

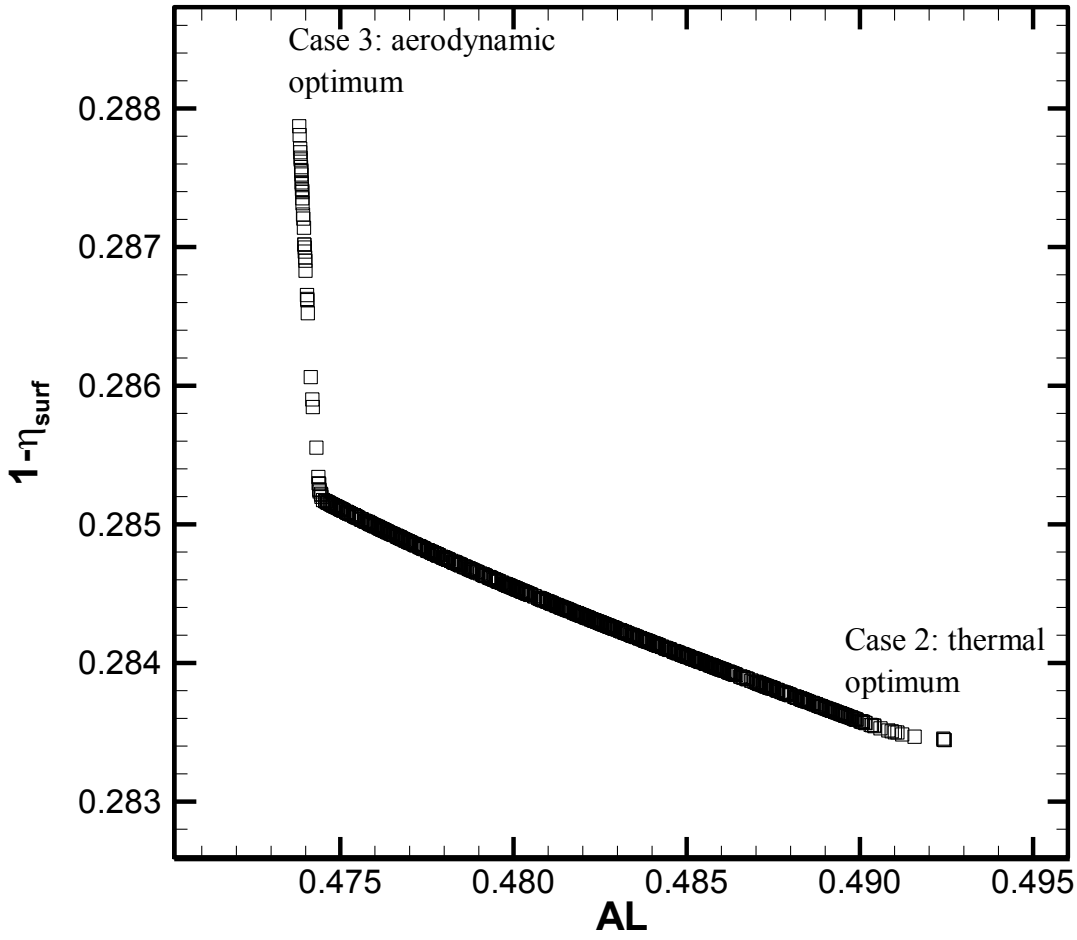

Figure 4-16: Pareto front of optimal solutions obtained with ANN-based NSGA II results

4.4. Single objective optimization on the vane suction side

The aerodynamic and thermal optima identified on the Pareto front are re-produced herein using single objective optimizations. The weighted sum of a three-component optimization function of Equation (2-64) is used. This unique function aims to simultaneously maximize the distribution of the adiabatic film cooling effectiveness (η) and minimize the aerodynamic loss (AL) computed at the cascade exit. Furthermore, for this optimization exercise, the user-defined weight C_2 of Equation (2-64) is set to zero. Hence, the optimization algorithm targets to minimize the resulting objective function:

$$F_{obj}(X) = \left[C_1\left(1-\eta_{surf}\right)+C_3\left(AL\right)\right] \tag{4-6}$$

As seen earlier, X is the vector of design variables, namely $p_{0c} / p_{0\infty}$ and T_c / T_∞. The first term in the objective function allows maximizing the film cooling effectiveness over the vane suction surface. The second term minimizes the aerodynamic loss induced by the film cooling. C_1 and C_3 are user-defined weights ranging from 0 to 1 such that their sum is equal to 1. The weights allow the designer to assign a different "level of importance" to each term of the objective function. Both terms of the objective function are normalized between 0 and 1 with respect to the minimum and maximum values in the design space.

Two separate optimizations are conducted. The difference between each single objective optimization is the design "importance level" appointed to either the thermal or the aerodynamic performance of the cooling scheme. The design importance is assigned via the user-defined weights C_i inside $F_{obj}(X)$. The first optimization is a purely thermal optimization in which the user-defined weights are set to C_1 = 1.0, and C_3 = 0.0. The second optimization is a purely aerodynamic one in which the user-defined weights are set to C_1 = 0.0, and C_3 = 1.0.

A third optimization is conducted as well and denoted as an aero-thermal optimization, in which the user defined weights in the objective function are set to $C_1 = 0.5$, and $C_3 = 0.5$. This assigns equal importance to a maximum cooling performance and a minimum aerodynamic penalty. Three separate ANNs are constructed for the three individual optimizations. All three ANN's are trained with 70% and tested with 30% of the LHS initially-selected design points.

The thermal optimization requires an ANN designed with one hidden layer composed of 2 hidden nodes. The ANN training algorithm is implemented for 5000 iterations before the relative error reaches convergence. The average relative error related to training the ANN is 38% and the average relative error in testing is 32%. The aerodynamic optimization ANN has one hidden layer composed of 1 hidden node only. The training requires 8,000 iterations for convergence. The average relative error related to training the ANN is 0.21% and the average relative error in testing is 0.4%. The aero-thermal optimization requires an ANN composed of one hidden layer with 7 hidden nodes. 14,000 iterations are required for convergence. The average relative error related to training the ANN is 11% and the average relative error in testing is 21%.

The ANN is then coupled to the genetic algorithm to approximate the objective function during the optimization. Each optimization generation consists of 100 individuals. The optimization process converges after about 50 generations. The mutation probability is set to 0.15, whereas the cross over probability is set to 0.7. Two elite individuals are transferred from one generation to the next.

Table 4-6 presents the results of the three single objective optimizations that are conducted, and displays the CFD predictions and experimental measurements of AL and η_{surf} in comparison to the reference case. The experimental test case obtained at BR = 0.9 and $T_c / T_\infty = 1.09$ and shown previously in Table 4-3 is considered as a reference case for the optimization work.

Table 4-6 shows that the thermal optimum is obtained at a blowing ratio of BR = 0.6, and $T_c / T_\infty = 1.13$ which is highest within the design space. In effect, T_c of the reference case is set to 325K whereas T_c of the thermal optimum is equal to 338K. Therefore, an increase of 4% in coolant temperature and a drop of 30% in blowing ratio contribute to increasing the cooling performance η_{surf} by over 100%. With experimental measurements, the improvement in cooling performance is estimated to be 43%. The improvement in cooling performance is thereby over-predicted by the CFD simulations. Furthermore, the thermal optimum results in a lower aerodynamic loss than the reference case. This is attributed to the reduced mixing between the coolant and the mainstream at the exit of the hole as the mass flow rate is reduced. CFD predicts a reduction of about 4% in aerodynamic loss. Experimental measurements reveal a reduction of about 20% in *AL*. Therefore, CFD simulations seem to under-predict the improvement in *AL*.

The aerodynamic optimum has the lowest blowing ratio of all cases. It is obtained at BR = 0.35, and this results in a minimum aerodynamic loss of *AL = 0.4721* as predicted by CFD. In effect, *AL* of the aerodynamic case is 3% lower than that of the thermal optimum as predicted by CFD. With experimental measurement, the reduction in *AL* is almost 13%. This improvement is due to one main factor, a significant reduction in mixing between the coolant and the mainstream due to the reduction in coolant mass flow exiting the cooling holes. However, the improvement in the aerodynamic performance is detrimental to the cooling performance as η_{surf} decreases by about 28% as predicted by CFD. Experimental measurements show that the reduction of 13% in *AL* is accompanied with about 17% reduction in η_{surf}.

Finally, the aero-thermal optimum is obtained for a blowing ratio that is slightly higher than that of the thermal case, BR = 0.65. Consequently, the aero-thermal solution provides a relatively high cooling performance. In effect, η_{surf} is only 12% lower than the thermal optimum as

predicted by CFD. Experimental measurements reveal that η_{surf} is 6% lower than the thermal optimum. As for the aerodynamic loss, CFD predicts an increase of 4% in *AL* with respect to the aerodynamic optimum. Experimental measurements indicate an increase of 23%, thereby re-iterating that CFD seems to under-predict changes in *AL*.

The trend obtained in the variation of cooling performance and aerodynamic penalty is in accordance with the authors' expectations and the experimental data, which enforces the level of confidence in the optimization methodology. In effect, the opposing trend of the blowing ratio and the coolant temperature on the objectives, namely, the cooling effectiveness and the aerodynamic loss is well depicted by the optimization procedure. Furthermore, excellent qualitative agreement is obtained between the optimization results and the experiments. Both experiments and ANN-based optimization identified that the optimum cooling performance is obtained at BR=0.6, whereas the optimum aerodynamic performance is obtained at BR=0.35. Such qualitative agreement allows substantiating the reliability of the optimization methodology in identifying optimum designs within a design space.

Furthermore, there is good qualitative agreement between experimental measurements of the objective functions and the corresponding CFD predictions. A reasonable quantitative agreement between the CFD predicted objective functions and the experimentally measured ones is also observed. This verifies again the accuracy of the numerical model in predicting the aerodynamic and cooling performances of the cooling scheme.

Moreover, Table 4-6 presents the ANN predictions of the objective functions. The ANN prediction for the thermal optimum case is 1- η_{surf} = 0.2834 or η_{surf} = 0.7166, which is within 24% of the CFD prediction. The ANN predicts *AL* = 0.474 for the aerodynamic case, which is within 0.4% of the CFD prediction. As for the aero-thermal optimum point, the ANN predicted

objective function is 0.368, which is within 12% of the CFD prediction. The agreement between ANN and CFD is therefore deemed reasonable. The agreement is best for *AL* of the aerodynamic optimum and worst for η_{surf} of the thermal optimum.

Figure 4-17 presents the laterally averaged adiabatic film cooling effectiveness distribution on the vane suction surface downstream of the cooling holes for the three optimum solutions. Both experimental measurements and numerical predictions of the optimum solutions are presented.

The experimental measurements of the spanwise averaged effectiveness for the thermal optimum and the aero-thermal optimum are almost identical. The thermal optimum presents, however, experimental effectiveness values that are slightly higher (4%) in the region of $s/D = 12$ to $s/D = 15$. The CFD predictions also exhibit effectiveness trends that are almost identical for the thermal and aero-thermal optimums. Similarly to experiments, CFD predicts higher effectiveness for the thermal optimum for $s/D < 15$. For $s/D > 15$, the effectiveness trends are identical, but the thermal optimum has 8% higher effectiveness magnitude than the aero-thermal optimum.

Experimental measurements of the aerodynamic optimum case show an η_{span} distribution that is about 19% higher than that of the thermal optimum in the region between $s/D = 12$ to $s/D = 15$. This is attributed to the reduction in blowing ratio from BR = 0.6 to 0.35 which results in a much better attachment of the coolant to the vane surface immediately downstream of the hole exit. But the effectiveness of the aerodynamic optimum becomes about 20% lower than the thermal optimum for the region beyond $s/D = 20$. A similar trend is observed in the CFD predictions. In effect, for $s/D = 6$ to $s/D = 10$, the aerodynamic optimum yields an effectiveness magnitude that is about 14% higher than the thermal optimum. However, beyond $s/D = 10$, the effectiveness is over 100% lower than the thermal optimum, as the weak coolant jet is over-powered by the mainstream flow further downstream of the cooling holes.

Colored contours of the CFD-predicted non-dimensional coolant temperature $\Theta = (T - T_{\infty,in}) / (T_{c,in} - T_{\infty,in})$ are shown in Figure 4-18 and plotted on an *xy* plane located along the centerline of the coolant jet exiting the first row of film cooling holes. The extent of the coolant penetration into the mainstream can be evaluated through this figure. A higher mass flow rate suggests a higher momentum of the coolant exiting the hole, which leads to further penetration of the coolant in the mainstream. The reference case presents contours of a non-dimensional temperature of unity that extend highest in the vertical direction (*y*) than any other case. The contours reveal the deepest penetration of the coolant into the mainstream. This is immediately attributed to the fact that the reference case has the highest blowing ratio, indicating a higher momentum of the coolant exiting the cooling holes than in any other case. Furthermore, as noted previoulsy in Figure 4-14, there is coolant flow lift-off at BR = 0.9. This is confirmed here as entrainment of the mainstream flow under the coolant jet is visible. The aerodynamic optimum presents the least penetration into the mainstream since it is obtained at the lowest BR of 0.35. In this case, the coolant jet is weak and is rapidly dissipated into the mainstream not far downstream from the cooling holes. The thermal optimum presents a high vertical ejection of the coolant from the cooling holes, however, no mainstream entrainment is observed, thereby indicating a good protection of the vane surface by the coolant flow. Finally, the contours for the aero-thermal optimum, which is obtained at BR = 0.65 that is not much different from the thermal one, indicate a slight mainstream entrainment that is initiated at this particular blowing ratio. This figure demonstrates the direct relationship between increasing blowing ratio and the subsequent increase in coolant penetration. In the present scenario, the optimum blowing ratio is 0.6, at which the cooling performance is highest before the beginning of mainstream entrainment under the coolant.

Figure 4-19 presents colored contours of the adiabatic cooling effectiveness (η) on the vane suction surface. The contours demonstrate the superior performance of the thermal optimum. The thermal optimum case presents the highest η magnitude contours immediately downstream the hole. The contours of η at the holes exits and immediately downstream of them is widest in the z-direction in comparison to the reference case and to all other cases as well. This signifies the best surface lateral coverage is obtained with the thermal optimum. Furthermore, the thermal optimum exhibits substantial η contours of values higher than 0.3 (red) that persist all the way to s/D = 14.6. The thermal optimum coolant trace lasts the longest on the vane surface. Again, these high magnitude η contours indicate a very strong lateral spreading of the coolant as they are widest in the z direction. The η distribution described above translates into an overall better cooling performance.

The aerodynamic optimum case presents a short but thick trace of coolant at the cooling hole exits and immediately downstream of them. This wide trace of η has a magnitude higher than 0.3 but persists only to about s/D = 5, at which point the η magnitude decreases quickly. The coolant trace for the first row of holes vanishes by s/D = 6.3 indicating the dissipation of the weak coolant trace into the mainstream and leaving an unprotected vane surface.

The aero-thermal optimum does not present any coolant lift-off. However, the reduction in cooling performance with respect to the thermal optimum is very well visible, as the coolant trace at the cooling hole exit is thinner in the z direction. This is directly attributed to the increase in blowing ratio.

Finally, coolant lift-off is clearly depicted in the reference case. In effect, the trace of coolant at the hole exit is very thin and relatively non-existent. The trace re-appears around s/D=3.7 as the

coolant jet is being pushed downwards by the mainstream flow and begins to re-attach to the vane surface.

Figure 4-20 presents local total pressure loss coefficient (C_p) profiles measured at two different *zy* planes downstream of the vane trailing edge; namely one fourth axial chord length, and one axial chord length. The C_p profiles are presented for the thermal, aero-thermal, and aerodynamic optimums, as well as the reference case. The figure indicates that increasing coolant mass flow rate increases the stagnation pressure losses. The highest C_p peak magnitudes are observed for the reference case; BR = 0.9. These are followed very closely by the thermal and aero-thermal optimums, which are obtained at BR = 0.6 and BR = 0.65 respectively. The lowest C_p peak magnitudes are obtained for the aerodynamic optimum which has the lowest blowing ratio of 0.35. Furthermore, the profiles indicate that the sensitivity of the aerodynamic loss to changes in blowing ratio is higher in the lower ranges of BR.

C_p data is supported by profiles of non-dimensional turbulence kinetic energy (k/U_∞^2) at one fourth axial chord length, and one axial chord length downstream of the vane trailing edge; Figure 4-21. The turbulence kinetic energy profiles match very closely the C_p profiles, indicating once more, that the aerodynamic penalty is minimum at the lowest blowing ratio and maximum at the highest within a specified design space.

Figure 4-22 presents the non-dimensional turbulence kinetic energy (k/U_∞^2) contours at three different *yz* planes located downstream of the second row of cooling holes, namely at s/D = 12, s/D = 13, and s/D = 18. The contours exhibit somewhat circular forms of high turbulence kinetic energy at the centre-lines of the coolant flow exiting the first and second rows of holes. This elevated (k/U_∞^2) region varies in shape and intensity from one case to another.

At s/D = 11.72, the reference case presents a region of elevated k/U_∞^2 that has a circular form. At s/D = 13.17, the circular shape seems to reduce in size, its edges tend to fade into the mainstream, as the k/U_∞^2 also reduces to around 0.06. At s/D = 17.86, k/U_∞^2 is lowered to around 0.02. The cicular shape is almost dissipated into the mainstream. This behavior is directly attributed to the higher blowing ratio of 0.9, at which the aerodynamic case is obtained. In effect, the coolant is lifted-off the surface and is penetrated into the mainstream. The large k/U_∞^2 is responsible of the higher AL obtained with the reference case.

The thermal optimum presents a rectangular shaped region of elevated turbulence kinetic energy (k/U_∞^2 = 0.11) at the centre-line of the first row of holes. Further downstream, at s/D = 13.17, the rectangular shape seems to elongate in the lateral z-direction. The magnitude of k/U_∞^2 is reduced to around 0.09. Then, at s/D = 17.86, the rectangular shape dissipates, the magnitude of k/U_∞^2 reduces to 0.03.The rectangular shape of high k/U_∞^2 is a result of the strong coolant coverage obtained with the thermal optimum, and the fact that the coolant is completely attached to the vane surface

The aero-thermal optimum presents a very similar behavior of k/U_∞^2 to the thermal optimum. This is direclty related to the fact that the blowing ratios are very similar, and consequently the resulting aerodynamic penalty.

The aerodynamic optimum presents a very similar behavior to the thermal case as well. However, the rectangular shapes are much smaller, as the blowing ratio is lower (BR = 0.35) and a much smaller flow rate of coolant is exiting the holes. The weaker k/U_∞^2 is responsible of the lower AL obtained with the aerodynamic optimum.

The contours of turbulence kinetic energy and profiles of total pressure loss coefficients allow validating the improvement in aerodynamic performance recorded as the coolant mass flow rate is decreased. This supports predictions of the aerodynamic loss.

Table 4-6: Single objective optimization results

	Design Weights		**GA output ANN-based**		**ANN output**	**CFD output**			**Experimental output**	
	C_1	C_3	$p_{0c}/p_{0\infty}$	T_c / T_∞	F_{obj}	**BR**	η_{surf}	AL	η_{surf}	AL
Reference case	N/A	N/A	1.027	1.098	N/A	0.90	0.367	0.509	0.544	0.481
Thermal optimum	1.0	0.0	0.958	1.130	$1-\eta_{surf} = 0.283453$	0.60	0.945	0.489	0.777	0.386
Aerodynamic optimum	0.0	1.0	0.920	1.130	$AL = 0.473954$	0.35	0.648	0.472	0.641	0.333
Aero-thermal optimum	0.5	0.5	0.967	1.098	$0.5(1-\eta_{surf}) + 0.5AL=0.368$	0.65	0.833	0.492	0.731	0.410

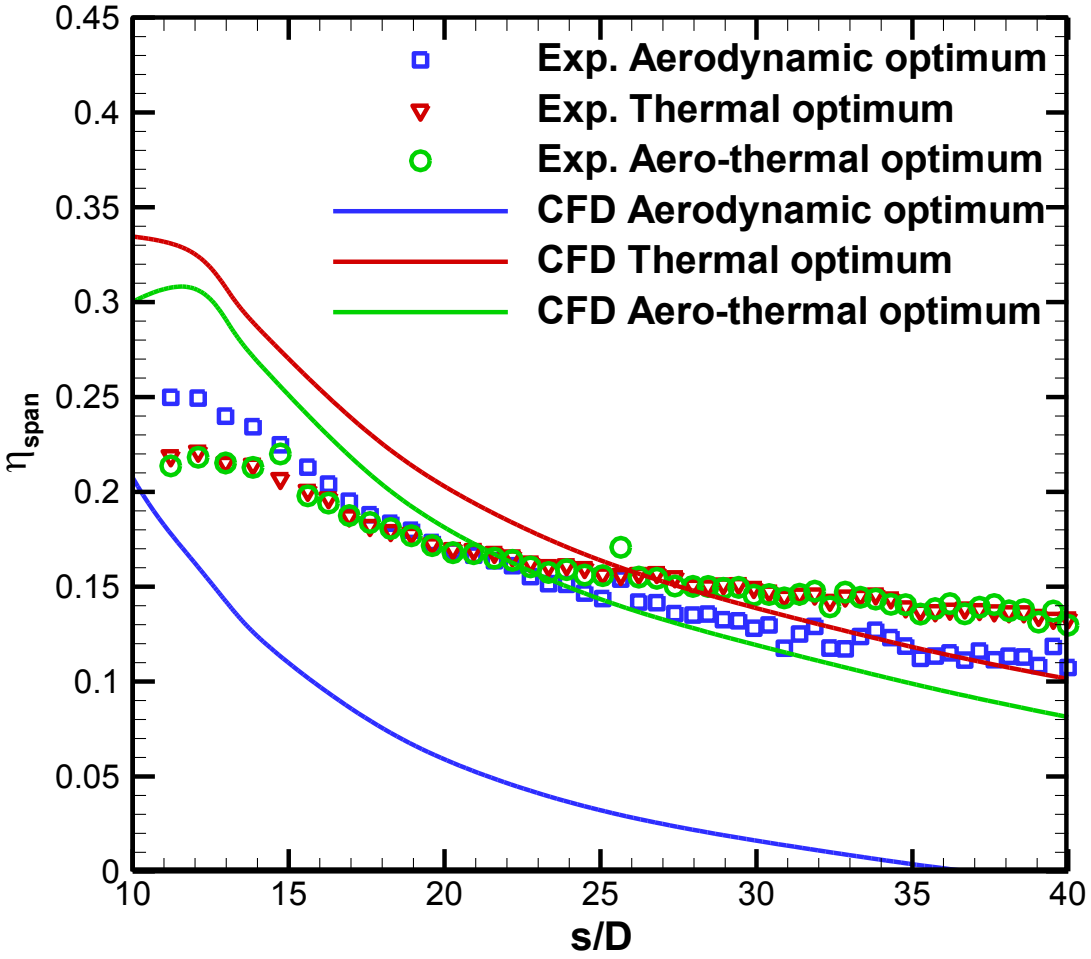

Figure 4-17: Laterally averaged adiabatic cooling effectiveness for the three single objective optimum solutions

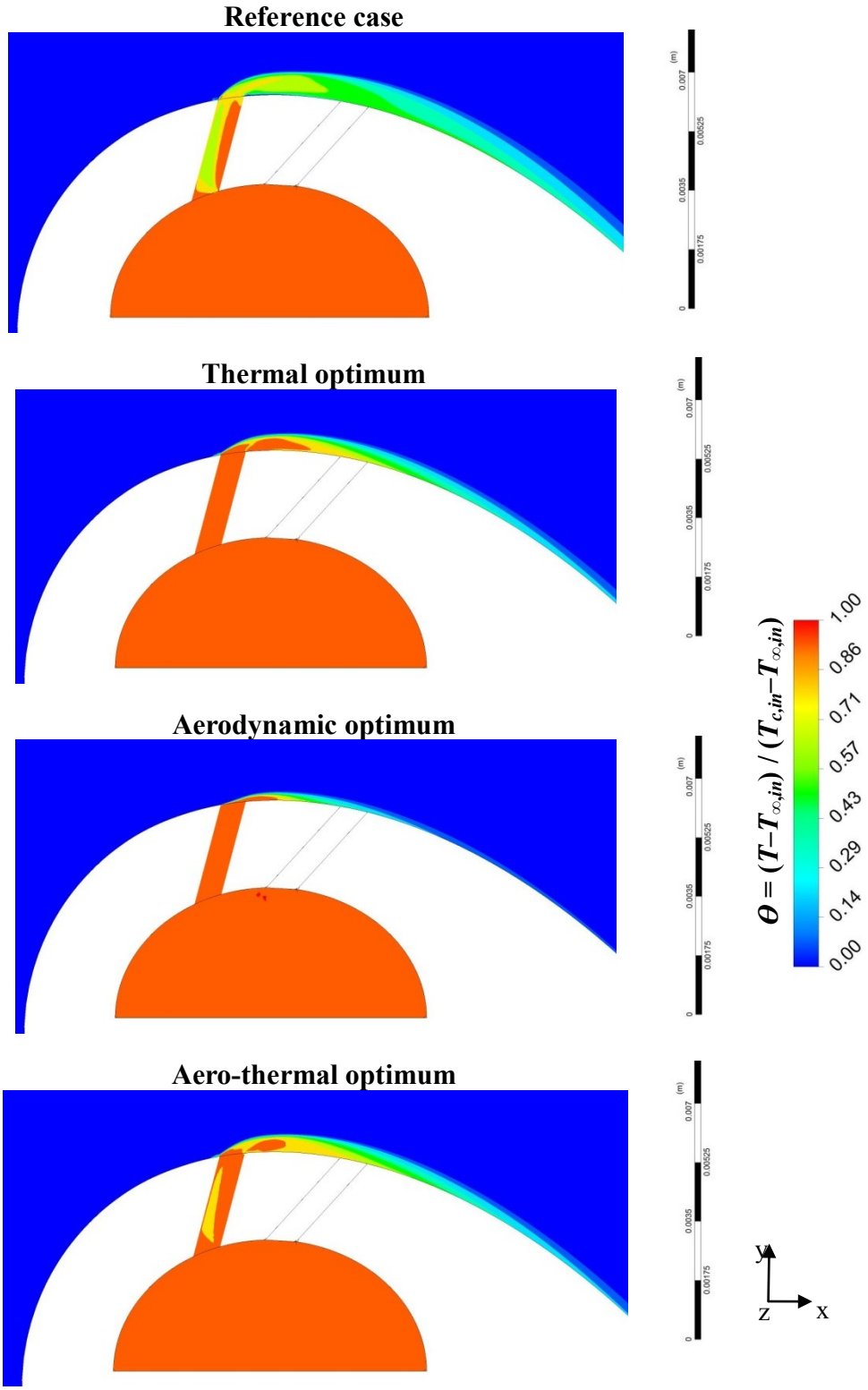

Figure 4-18: Non-dimensional temperature contours on an *xy* plane along the centerline of first row of cooling holes

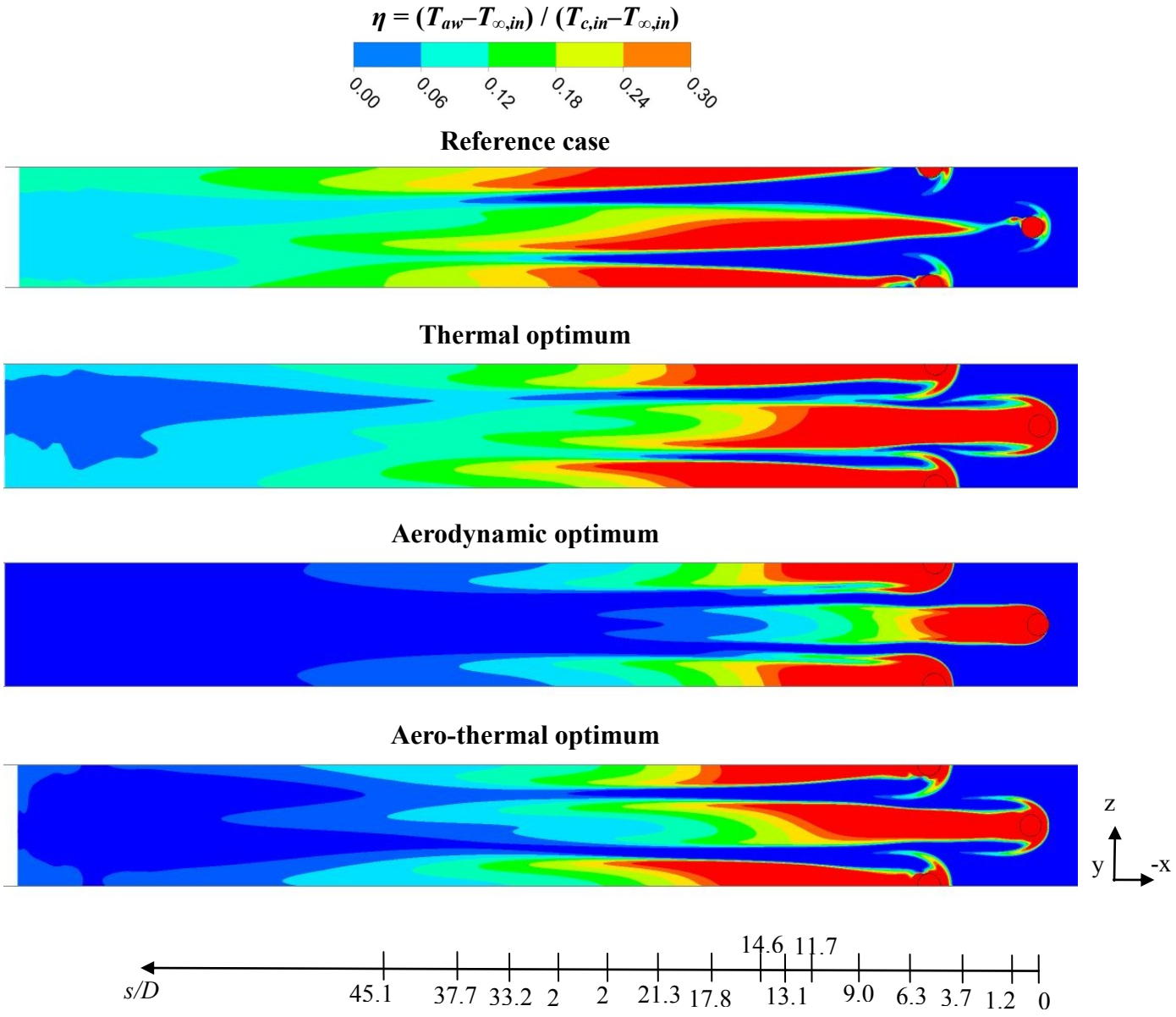

Figure 4-19: Adiabatic film cooling effectiveness contours on the vane suction surface

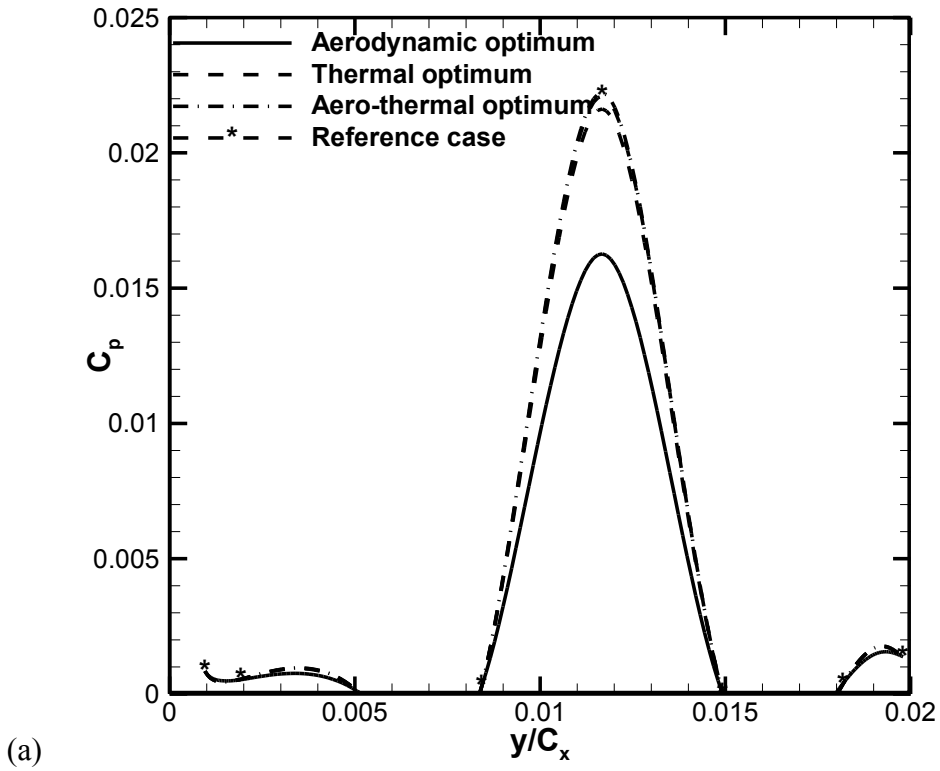

(a)

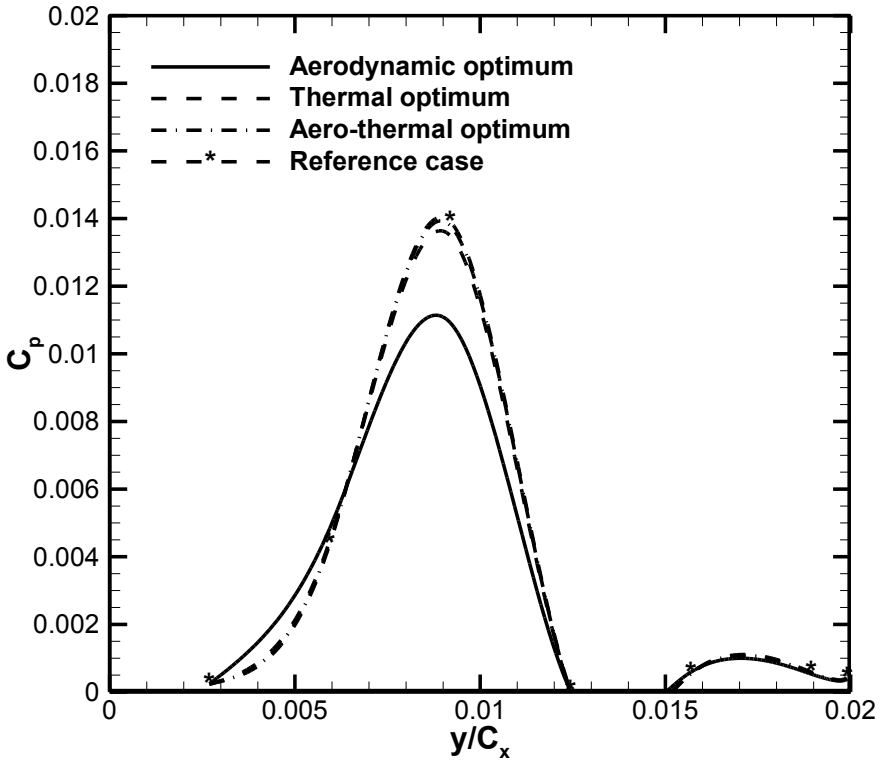

(b)

Figure 4-20: Local pressure loss coefficient profiles (a) at one fourth axial chord downstream (b) at one axial chord downstream from vane trailing edge

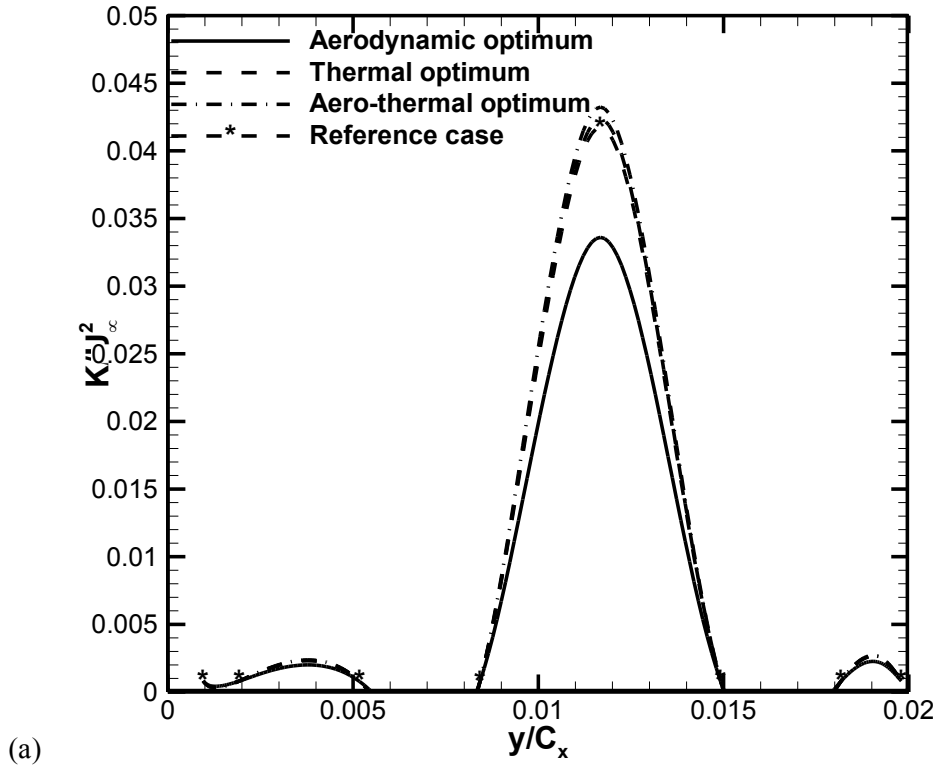

(a)

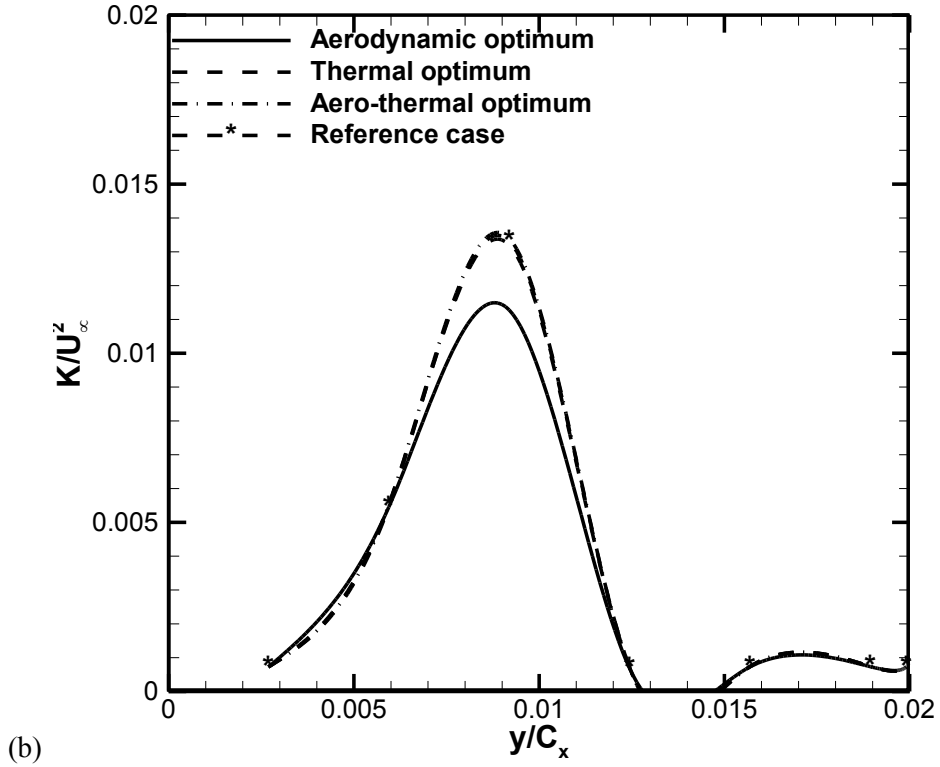

(b)

Figure 4-21: Local non-dimensional turbulence kinetic energy profiles (k/U_∞^2) (a) at one fourth axial chord downstream (b) at one axial chord downstream from vane trailing edge

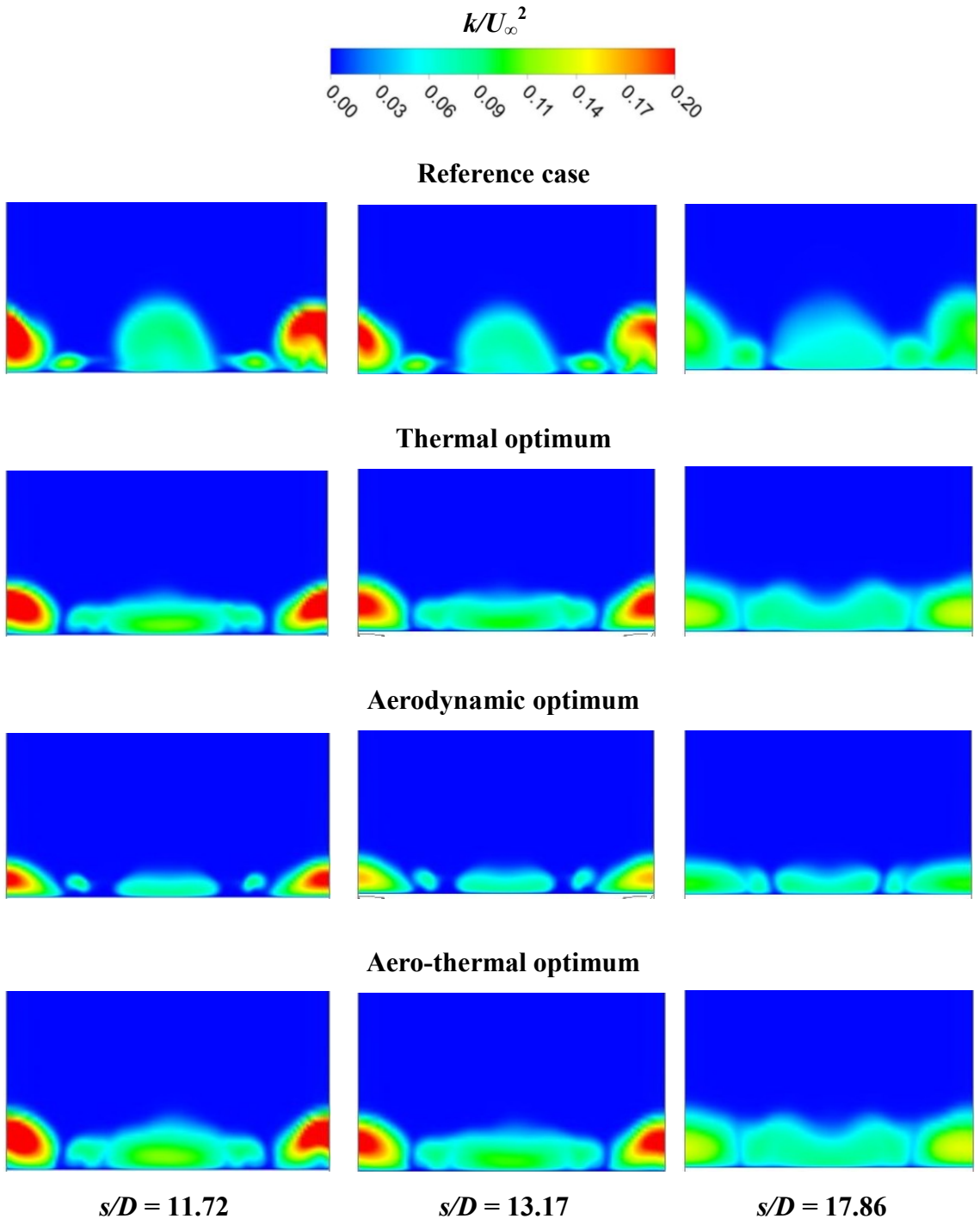

Figure 4-22: Non-dimensional turbulence kinetic energy (k/U_∞^2) contours on three *yz* planes downstream of the cooling hole

4.5. Conclusion

The proposed aero-thermal optimization methodology is applied to a turbine vane that is typical of first stage high-pressure turbines. Consistently with the previous work, governing coolant flow parameters were used as optimization design variables, namely, the coolant to mainstream total pressure ratio and the coolant to mainstream static temperature ratio. The optimization objectives consisted in improving the adiabatic film cooling effectiveness while reducing the aerodynamic loss represented by the total pressure loss coefficient.

The present chapter work demonstrated the potential of the optimization approach as an efficient and reliable design tool for film cooling in gas turbine applications. This was achieved by experimentally verifying the accuracy of the CFD model in predicting the objective functions. In effect, the prediction of the isentropic Mach number distribution was first assessed against experimental data for a nominal blowing ratio of 0.9, and the agreement was deemed very good. Then, the CFD prediction of the spanwise averaged effectiveness distribution downstream the cooling holes was assessed against experimental measurements for three different blowing ratios, 0.6, 0.9, and 1.2. Several turbulence models were tested, and the best agreement was recorded with the SST model. Independence of the CFD results from mesh size was also established. At BR = 0.9, initial separation of the coolant from the airfoil surface was recorded with CFD. At BR = 1.2, complete coolant flow lift-off from the airfoil surface was established for both experiments and CFD. This was observed experimentally and numerically with a drastic drop in effectiveness values. Finally, predictions of the objective functions, namely the surface average of the effectiveness and the aerodynamic loss was assessed against experimental data and agreement was found to be acceptable. The predictions of η_{surf} were within 34% of the experiments, and predictions of AL were within 20% of experimental data.

Furthermore, the accuracy of the optimization methodology in identifying the optimum designs within a specific design space was substantiated against experimental data as well. Experiments were conducted to reproduce the reference case, and the aerodynamic, thermal, and aero-thermal optimum solutions. Results indicated that CFD tends to over-predict changes in cooling effectiveness and under-predict changes in aerodynamic loss. The agreement between predicted and measured data was very acceptable.

Moreover, a purely thermal optimization generated a thermal optimum case that yielded over 100% increase in surface averaged effectiveness with respect to the reference case, according to CFD predictions. The improvement in cooling performance was accompanied with a minor improvement in the aerodynamic penalty as the aerodynamic loss decreased by 4% with respect to the reference case due to the reduction in coolant mass flow rate. The aerodynamic optimum was obtained at the lowest blowing ratio of all cases and yielded an aerodynamic loss 3% lower than the thermal case, according to CFD predictions. The improvement was attributed to a significant reduction in mixing between the coolant and the mainstream. The improvement in aerodynamic penalty was detrimental, however, to the cooling performance, which decreased by 28% with respect to the thermal optimum. Finally, an aero-thermal optimum was obtained for a blowing ratio that was slightly higher than that of the thermal case. The cooling performance obtained with the aero-thermal optimum was lower than the thermal optimum. Similarly, the aerodynamic performance of the aero-thermal optimum was worse than that of the aerodynamic optimum.

Since the optimization methodology was substantiated against experiments, it can now be employed to optimize film cooling hole shape. Therefore, Chapter 5 consists in expanding the current design space to include governing film hole geometric design variables.

CHAPTER 5

Film Cooling Shape Optimization on a Vane Suction Surface

In this chapter, the optimization methodology that was validated earlier is applied on the vane suction side to optimize the geometric shape of the film cooling hole. As detailed previously, three geometric design variables are considered, the film cooling hole lateral injection angle or compound angle CA, the film cooling hole conical expansion angle β, and the ratio of non-expanded portion of the cooling tube length to the hole diameter L_c / D. The objective of the present optimization work remains the same as earlier, maximizing the surface average adiabatic film cooling effectiveness while minimizing the corresponding aerodynamic loss.

5.1. CFD model

The geometry of the simulated CFD domain remains the same as in Chapter 4. It consists of a single vane, with two staggered rows of cooling holes on its suction side. The details of the CFD domain and cooling holes are presented in Figure 4-7. The main geometric and flow parameters of the vane cascade are summarized in Table 4-1 and Table 4-2 respectively.

As the SST model was proven accurate enough to provide predictions of the cooling effectiveness and the aerodynamic loss, it is used in the present work.

The computational grid topology and size remain the same as in Chapter 4. The details of the mesh are shown earlier in Figure 4-8, Figure 4-9, Figure 4-10, and Figure 4-11. Mesh independent results were obtained and presented earlier in Figure 4-15.

The coolant flow governing parameters remain constant throughout the present optimization investigation. They are derived from the optimization work of Chapter 4 and yield the optimum thermal solution of the earlier chapter presented in Table 4-6. The blowing ratio is therefore kept constant at 0.6, which allows a fully attached coolant flow to the vane surface. The coolant temperature is maximum as $T_c / T_\infty = 1.13$.

5.2. Multiple objective shape optimization of film cooling on the vane side

The design space constituted by the lower and upper limits of the design variables is shown in Table 5-1. The design space allows the hole to vary from an axial cylindrical hole to a compounded conically flared hole. Ten design candidates equally spaced inside the design space are selected by Latin Hypercube Sampling (LHS). Numerical predictions are performed at these ten design candidates and the results are presented in Table 5-2. The table provides the numerical predictions of the aerodynamic loss AL, and the cooling performance η_{surf}. Both are normalized with respect to their maximum and minimum values within the design space.

The current multiple objective optimization is similar to the ones conducted previously. It is characterized by two objective functions that are simultaneously and independently optimized using the NSGA-II, Deb (2001). Each GA generation is composed of 80 individuals, and the optimization is stopped after 60 generations. The values of crossover and mutation probabilities are 0.7 and 0.15, respectively. Two elite individuals are transmitted from one generation to the next.

The Pareto optimum solutions computed using the ANN-based NSGA-II, are shown in Figure 5-1 forming the Pareto front, which is a concave curve of the thermal objective function, given by $(1-\eta_{surf})$, vs. the aerodynamic objective function, given by AL.

The extreme right end of the front corresponding to the point ($x = 0.484$; $y = 0.279$) on the Pareto curve is characterized by a minimum $(1-\eta_{surf})$ or an otherwise maximum cooling performance, and a maximum AL or an otherwise worst aerodynamic performance. This point can be denoted as the thermal optimum. The point ($x = 0.421$; $y = 0.395$) on the Pareto curve corresponding to the extreme left end is characterized by a minimum AL or an otherwise best aerodynamic performance and a maximum $(1-\eta_{surf})$ or an otherwise minimum cooling performance. This point can be denoted as the aerodynamic optimum.

Both thermal and aerodynamic optima can be obtained with a single objective optimization provided the user defined weights are set appropriately.

Table 5-1: Design space and design variables of the shape optimization

Design variable	Lower bound	Upper bound
L_c / D	1.5	2.5
β	0^o	15^o
CA	0^o	90^o

Table 5-2: Initial design candidates selected by LHS for the shape optimization

Design Candidate	Input from LHS			CFD Output	
	L_c / D	β	CA	η_{surf}	AL
1	1.85	9.7	85.5	0.585	0.536
2	2.05	6.75	40.5	0.524	0.520
3	1.55	2.25	13.5	0.231	0.539
4	2.35	5.25	67.5	0.369	0.532
5	2.45	12.75	76.5	0.598	0.495
6	1.95	8.25	49.5	0.225	0.502
7	1.65	3.75	58.5	0.390	0.533
8	2.15	0.75	31.5	0.077	0.547
9	1.75	11.25	4.5	0.668	0.488
10	2.25	14.25	22.5	0.627	0.476

Table 5-3: Single objective shape optimization results

	Design weights		GA output (ANN based)			CFD output	
	C_1	C_3	CA	β	L_c / D	η_{surf}	AL
Cylindrical holes	N/A	N/A	0	0	N/A	0.162	0.553
Thermal optimum	1.0	0.0	83.0	14.8	1.51	0.790	0.429
Aerodynamic optimum	0.0	1.0	0.0	15.0	1.51	0.370	0.416

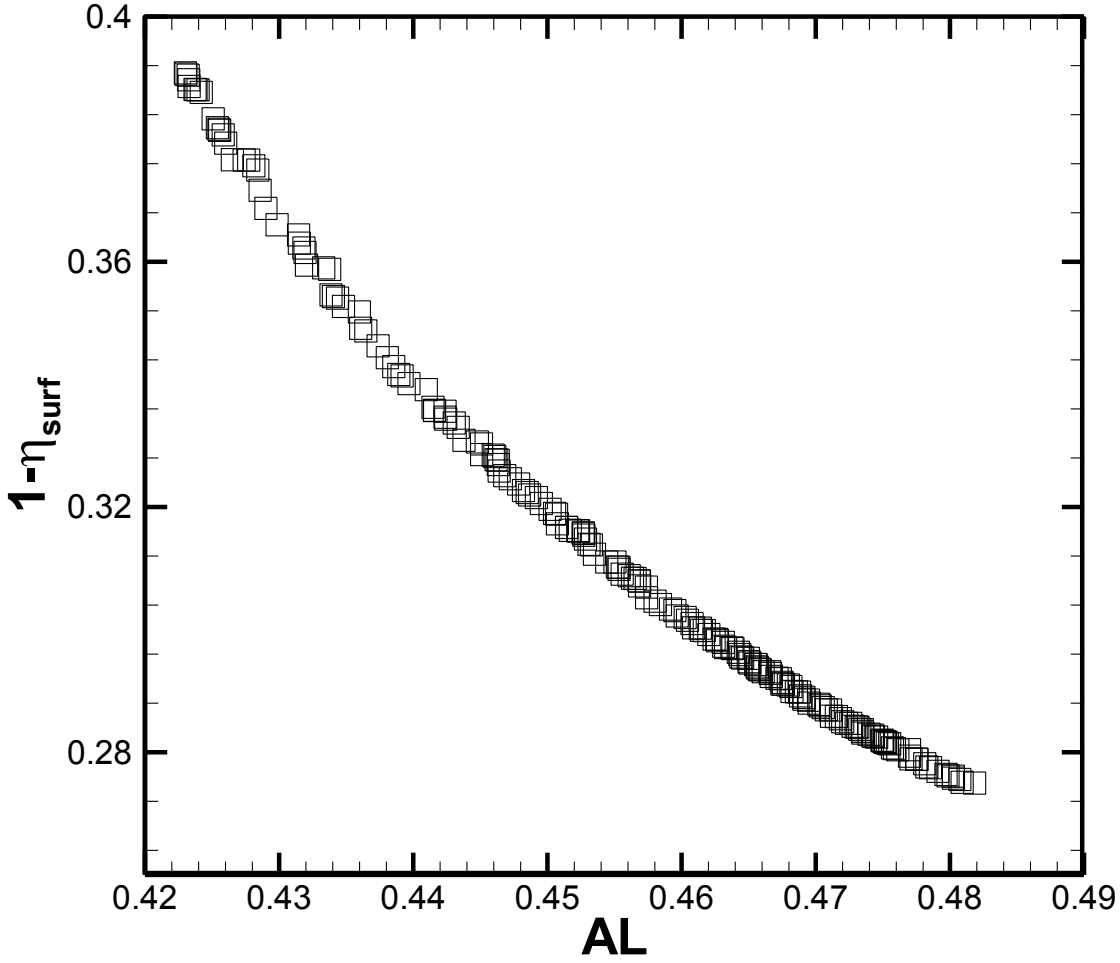

Figure 5-1: Pareto front of optimal solutions obtained with ANN-based NSGA-II results

5.3. Single objective shape optimization of film cooling on the vane suction side

The aerodynamic and thermal optima identified on the Pareto front are re-produced herein using single objective optimizations. Equation (4-6) is employed as an objective function and is a weighted sum of two-components, one designed to maximize η_{surf} and the other to minimize AL.

In the present case, X is the vector of the geometric design variables, namely CA, β, and L_c / D. Two separate optimizations are conducted. The difference between each single objective optimization is the design "importance level" appointed to either the thermal or the aerodynamic performance of the cooling scheme. The first optimization is a purely thermal optimization in which the user-defined weights are set to $C_1 = 1.0$, and $C_3 = 0.0$. The second optimization is a purely aerodynamic one in which the user-defined weights are set to $C_1 = 0.0$, and $C_3 = 1.0$.

Two separate ANNs are constructed for the two individual optimizations. Both ANN's are trained with 70% and tested with 30% of the LHS initially-selected design candidates.

The ANN for the aerodynamic optimization is designed with one hidden layer of 4 hidden nodes. The training requires about 2500 iterations for the average relative error to reach convergence. The ANN is coupled to the genetic algorithm to approximate the objective function during the optimization. Each optimization generation consists of 170 individuals. The optimization process is converged after about 27 generations. The mutation probability is set to 0.15, whereas the cross over probability is set to 0.7. Two elite individuals are transferred from one generation to the next. Four database enrichments are required to reach the aerodynamic optimum solution.

The evolution of the ANN predicted objective function (AL) with database enrichment is plotted in Figure 5-2. It is compared to the CFD predicted function. Both predictions exhibit a similar decreasing trend with database enrichment as the algorithm aims to minimize the function. The

ANN over-predicts the objective function by about 5% on average with respect to the CFD predictions. The final database enrichment yields a 1.5% error between ANN and CFD predictions.

The evolution of ANN testing and training relative average errors with database enrichment is presented next in Figure 5-3. Both errors exhibit the same trend in evolution, however, the test error is about 60% higher than the training error. The last database enrichment yields a testing error of 2.5%. As the error difference between the ANN and CFD predictions of *AL* is lower than the final testing error of 2.5%, the optimization is deemed complete, and the final solution is considered as the optimum aerodynamic solution.

The thermal optimization requires an ANN designed with one hidden layer composed of 7 hidden nodes. The ANN training algorithm is run for 300 iterations before the relative error reaches convergence.

The ANN is then coupled to the genetic algorithm to approximate the thermal objective function, $(1-\eta_{surf})$, during the optimization. Each optimization generation is composed of 270 individuals. The optimization process converges after about 27 generations. The mutation probability is set to 0.15, whereas the cross over probability is set to 0.7. Two elite individuals are transferred from one generation to the next. Four database enrichments are required to reach the thermal optimum solution.

The evolution of the ANN predicted thermal objective function with database enrichment is plotted in Figure 5-4. It is compared to the CFD predicted function. Both predictions exhibit a similar decreasing trend with respect to database enrichment. The ANN over-predicts the objective function by about 21% on average with respect to the CFD predictions. The final

database enrichment yields 23% error between ANN and CFD predictions.

The evolution of ANN testing and training relative average errors with database enrichment is presented next in Figure 5-5. Both errors exhibit similar trends in evolution. There is about 30% difference between the two errors. The last database enrichment yields a testing error of about 17%. Comparing the latter with the error difference between ANN and CFD predictions at the last database enrichment cycle indicates that the optimization may be deemed complete. The final solution is therefore considered the optimum thermal solution.

The evolution of the hole exit area with ANN database enrichments during the aerodynamic optimization is presented in Figure 5-6. The figure demonstrates how the optimizer directs its search towards a non-compounded hole with a maximum conical expansion. Meanwhile, the non-diffused length of the hole tube is driven to a minimum.

The hole exit area obtained at every ANN database enrichment during the thermal optimization is shown in Figure 5-7. The thermal optimum is attained with increasing compound angle and increasing conical expansion. The non-diffused length of the hole is minimum at the last database enrichment.

The change in the hole exit shape during single objective optimizations illustrates the optimizer capability in detecting the optimum solution location by the first database enrichment cycle only. This is clearly visible in Figure 5-8 and Figure 5-89 where evolution of the geometric variables with database enrichment cycles is presented. Further enrichment cycles beyond the first one allow for convergence of the optimizer towards the final solution within a much localized area of the design space. In effect, at the first database enrichment, β and CA are within 1^{o} on average from the final optimum solution. L_c / D is within 30% on average of the final optimum solution.

Table 5-3 presents the results of the two single objective optimizations and the corresponding CFD predictions of η_{surf} and AL. The objectives are normalized with their minimum and maximum values within the current design space, Table 5-1. The optimum solutions are evaluated against the cylindrical cooling hole. Both optimum solutions are widely expanded holes (high β and low L_c / D) and exhibit improvements in aerodynamic and cooling performances with respect to the cylindrical hole.

The aerodynamic optimum yields a 25% reduction in aerodynamic penalty relative to the cylindrical hole. The aerodynamic optimum hole consists of a maximum conical expansion of 15^o, a minimum cylindrical hole length of $1.5D$, and is axially oriented, or in the direction of the mainstream flow. Comparing CA behavior of Figure 5-8 with the one of AL, described in

Figure 5-2, indicates that an axial injection is crucial for a minimum AL. In fact, the figure demonstrates that CA remains in the vicinity of 1^o throughout all optimization cycles. The benefits of an axial injection on AL may be attributed to the well-behaved coolant flow exiting the film hole and a minimized mainstream-coolant interaction. This is particularly true for the present scenario where the coolant flow, which has already been diffused though the conical expansion, exits the film hole in a direction parallel to that of the mainstream. The latter is under subsonic conditions, and interaction between the two flows is minimum. On the other hand, L_c / D seems to have most impact on AL. A drop from a maximum ($L_c / D = 2.5$) to minimum ($L_c / D = 1.5$) value within the design space during the second database enrichment cycle results in about a 12% reduction in AL. This may be attributed to the increased length of the expanded portion of the hole, which acts as a diffuser, slows the coolant flow, and minimizes viscous dissipation of the coolant.

The thermal optimum yields a significant improvement in cooling performance with respect to the cylindrical hole. The improvement is over 100%. The thermal optimum hole has a high conical expansion of 14.8°, and a minimum non-expanded hole length of 1.51*D*. It is characterized by a high compound angle of 83° with respect to the mainstream flow direction.

Comparing Figure 5-9 to Figure 5-4 indicates that here the compound angle has the most impact on η_{surf}. In fact, an increase in CA from 65° to 83° during the first database enrichment allows a 23% reduction in the thermal objective function (1- η_{surf}). This indicates that a compound angle may enhance cooling performance; the benefits of the compound angle on cooling performance will be detailed next. β remains around its maximum value within the design space and L_c / D remains around its minimum value yielding a wide exit hole area. This maximum conical expansion for a low velocity coolant allows the best possible lateral coverage of the vane surface and a strong coolant attachment.

The optimization results indicate that under subsonic mainstream flow conditions, and for a low speed coolant velocity, the benefits of expanding the hole exit are two folds:

- Expanding the hole exit diffuses the coolant flow, allowing a reduction in viscous dissipation and therefore minimizing the aerodynamic loss.
- Expanding the hole exit reduces penetration of coolant into the mainstream and entrainment of the latter under the coolant flow. This minimized penetration results in a better behaved flow that exhibits stronger attachment to the vane surface and wider lateral coverage, therefore inducing a higher cooling performance.

Figure 5-10 presents the laterally averaged adiabatic film cooling effectiveness distribution on the vane suction surface downstream of the cooling holes for the thermal optimum solution. It

compares the thermal optimum performance to that of the cylindrical hole, the 10 LHS candidates that were sampled at equal distance within the design space, and the aerodynamic optimum. The thermal optimum presents an improvement in η_{span} of about 60% with respect to the cylindrical hole. Its performance is superior to any other solution within the design space. It is also 23% better than the aerodynamic optimum.

Colored contours of the CFD-predicted non-dimensional coolant temperature $\Theta = (T - T_{\infty,in}) / (T_{c,in} - T_{\infty,in})$ are shown in Figure 5-11 and plotted on an *xy* plane located along the centerline of the coolant jet exiting the two rows of film cooling holes. The extent of the coolant penetration into the mainstream can be evaluated through this figure. The contours demonstrate that the cylindrical holes result in the deepest coolant penetration into the mainstream. The thermal optimum presents the least penetration into the mainstream. However, contours of $\Theta = 1$ (red color) are most prominent in this case. They also extend further downstream the cooling holes on the vane surface. This demonstrates good attachemnt of the coolant flow to the vane surface, and a superior cooling performance. The aerodynamic optimum presents coolant penetration further into the mainstream than the thermal optimum. This is attributed to the axial injection of the highly expanded holes and deteriorates the cooling performance. Furthermore, the aerodynamic optimum coolant jet has lower temperature, (i.e. temperature closer to the local mainstream temperature), contributing to a lower cooling performance than the thermal optimum. Furthermore, even though the aerodynamic optimum yields further coolant penetration into the mainstream than the thermal optimum, the coolant velocity is lower. The coolant is therefore overpowered by the mainstream flow, which pushes it further towards the vane surface, ensuring protection of the vane surface and adequate coverage nonetheless. A coolant circulation inside the diffuser portion of the expanded holes can also be seen in Figure 5-11. Coolant

circulation is more prominent inside the aerodynamic optimum diffuser and is attributed to the high opening angle of the diffuser portion of the hole.

This figure demonstrates the benefits of a conical expansion and a compound angle on the cooling performance as follows:

- Applying a conical expansion to a cylindrical hole may reduce the coolant penetration into the mainstream and provide better coolant attachment to the airfoil surface.
- Applying a compound angle to an overly expanded hole may reduce coolant penetration even further and provide stronger coolant attachment to the surface. The compound angle also reduces coolant flow circulation inside the diffuser portion of the hole. The outcome is an enhancement in coolant velocity and temperature resulting in a superior cooling perfromance.

Figure 5-12 presents colored contours of the adiabatic cooling effectiveness (η) on the vane suction surface. The figure verifies the superiority of the thermal optimum solution in two ways. Firstly, the thermal optimum is practically the only solution presenting magnitudes of $\eta = 1$ immediately downstream the hole. The contours of elevated η are widest in the z-direction implying the best coolant coverage in the lateral direction. Secondly, the thermal optimum exhibits elevated η contours that persist longer in the downstream direction on the vane surface. Contours of $\eta = 0.7$ persist all the way to $s / D = 11$. Whereas, they only last until $s / D = 5$ for the aerodynamic optimum and $s / D = 3.7$ for the cylindrical holes.

Comparing the η contours of the aerodynamic optimum to those of the cylindrical hole clearly confirms that applying a conical expansion to a cylindrical hole improves the lateral coverage of the coolant in the mainstream. In effect, the coolant trace of the aerodynamic optimum is much

wider in z direction than the cylindrical holes. The conical expansion also diffuses the coolant significantly. In fact, traces of $\eta = 1$ are visible for the cylindrical holes but are completely absent in the case of the aerodynamic optimum. Most contours of the aerodynamic optimum exhibit $\eta = 0.7$, which extend further downstream on the vane surface than the cylindrical holes case. This supports the improvement in cooling performance observed with the aerodynamic optimum in comparison to the cylindrical holes.

Figure 5-13 presents local total pressure loss coefficient (C_p) profiles measured at a zy plane located one axial chord downstream of the vane trailing edge. The C_p profiles are presented for the aerodynamic optimum solution, the thermal optimum solution, and the cylindrical holes. The highest C_p peak magnitude is observed for the cylindrical holes. The lowest peak is obtained for the aerodynamic optimum. The aerodynamic optimum yields a reduction of about 20% in peak C_p in comparison with the cylindrical holes. This validates the findings for AL. The aerodynamic optimum is followed closely by the thermal optimum which produces a peak C_p that is only 4% higher than the aerodynamic optimum.

Analysis of the velocity field of the coolant flow at the hole exit reveals that the aerodynamic optimum geometry produces a lower velocity coolant flow exiting the hole in comparison with the cylindrical holes. In effect, the coolant velocity normalized by the mainstream local velocity at the injection location is plotted at the exit of the first row of holes in Figure 5-14. The reduction in coolant velocity is attributed to the conical expansion that diffuses the coolant flow, thereby reducing the magnitudes of its velocity and temperature in comparison to the cylindrical holes. Noting that in the present scenario, the local mainstream flow temperature is lower than the coolant temperature at the plenum inlet. Furthermore, the local mainstream flow velocity is subsonic, and the local Mach number at the injection location of the first row of holes is 0.35.

Therefore, a reduction in average coolant flow velocity at the hole exit minimizes the total pressure loss occuring as the coolant penetrates the mainstream. The accompanying reduction in coolant flow temperature minimizes the thermal dissipation occuring between the mainstream and the coolant flow, as the latter exits the cooling hole. This generates an aerodynamic optimum design with a lower aerodynamic penalty than the cylindrical holes.

The thermal optimum geometry is a conically expanded hole that is very similar to the aerodynamic optimum hole geometry, but with an added compound angle of 83^o. It can be seen that the compound angle increases the average coolant velocity at the hole exit and changes the distribution of the velocity field. This increases the cooling effectiveness values and provides a better lateral spreading of the coolant onto the vane surface, respectively. Therefore, the addition of the compound angle results in a superior cooling perfomance. However, the enhancement in average coolant velocity at the hole exit is accompanied with an increase in the total pressure loss coefficient. The compound angle has therefore detrimental effects on the aerodynamic loss, which is higher in the case of the thermal optimum design with respect to the aerodynamic optimum.

The results above indicate that a high compound angle is necessary for a high cooling performance. One would expect that the optimum cooling performance be obtained at a compound angle of 90^o instead of 83^o. In order to answer such doubts, an investigation of the sensitivity of η_{span} to varying CA was performed. Figure 5-15 presents η_{span} distributions over the vane suction surface downstream the cooling holes for the thermal optimum solution, and three other design candidates with varying compound angle, namely, CA = 0^o, 45^o, and 90^o. The two remaining design variables, L_c / D and β were kept unchanged during the investigation. The figure demonstrates that the thermal optimum obtained with CA = 83^o provides the highest η_{span}

values immediately downstream the cooling holes, i.e. between s/D = 5 and s/D = 15. Beyond s / D = 15, a compound angle of CA = 90^{o} results in the highest values of effectiveness. Therefore, the thermal optimum provides the best cooling performance in the near-field to the cooling holes which corresponds to the objective of the present optimization.

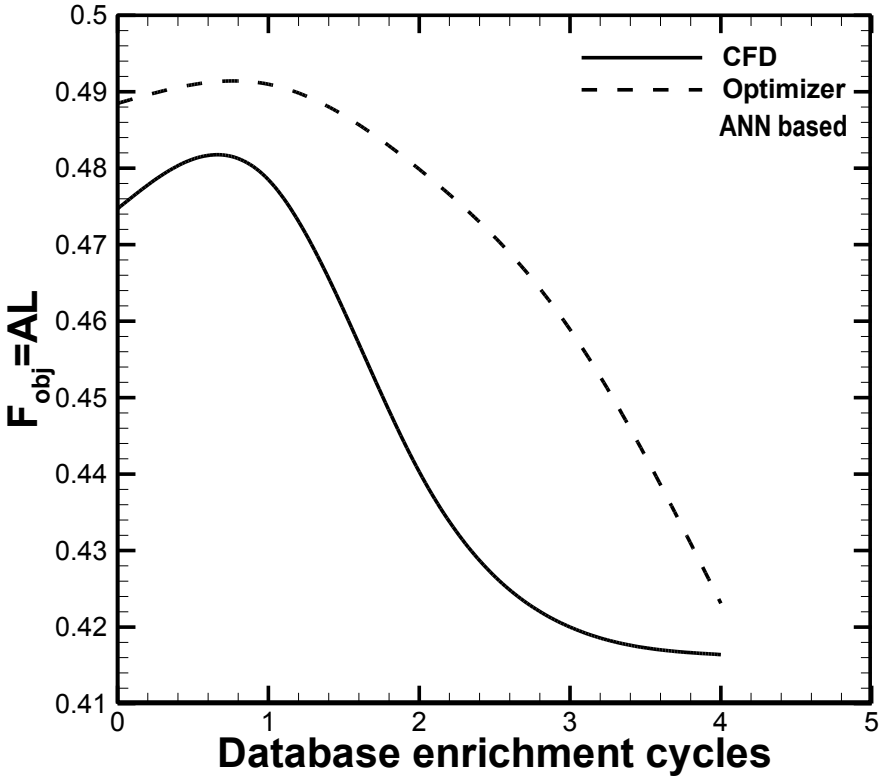

Figure 5-2: Evolution of the aerodynamic objective function with database enrichment

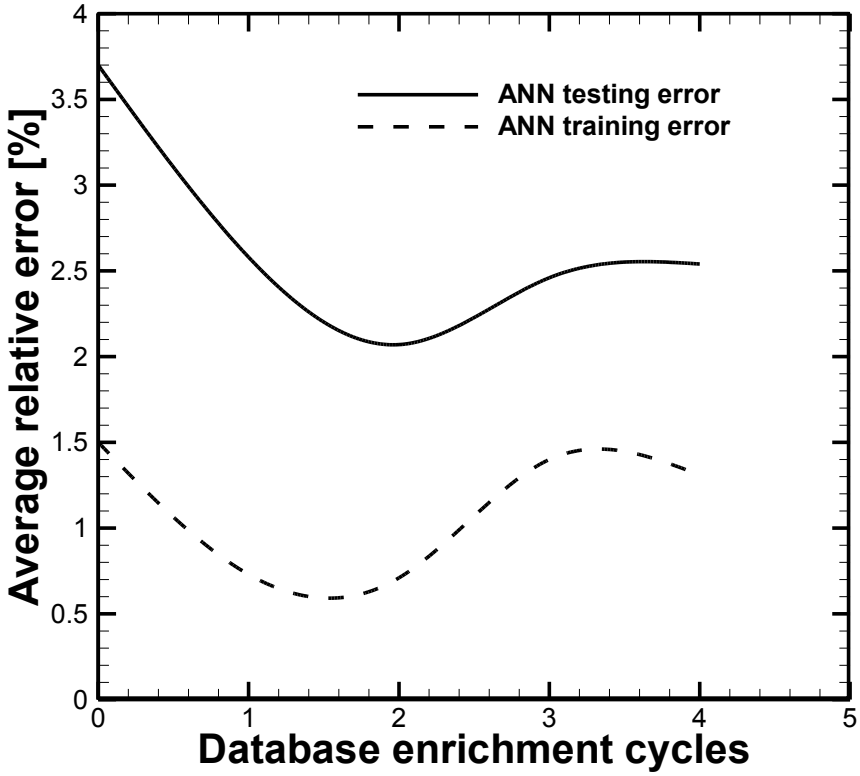

Figure 5-3: Evolution of the ANN testing and training errors with database enrichment during the aerodynamic optimization

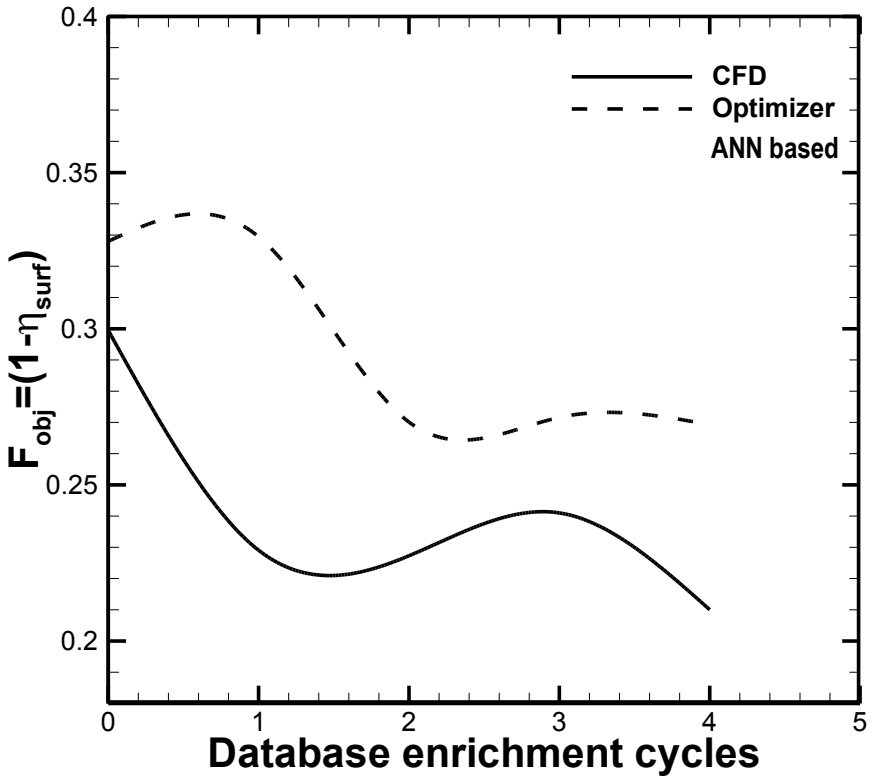

Figure 5-4: Evolution of the thermal objective function with database enrichment

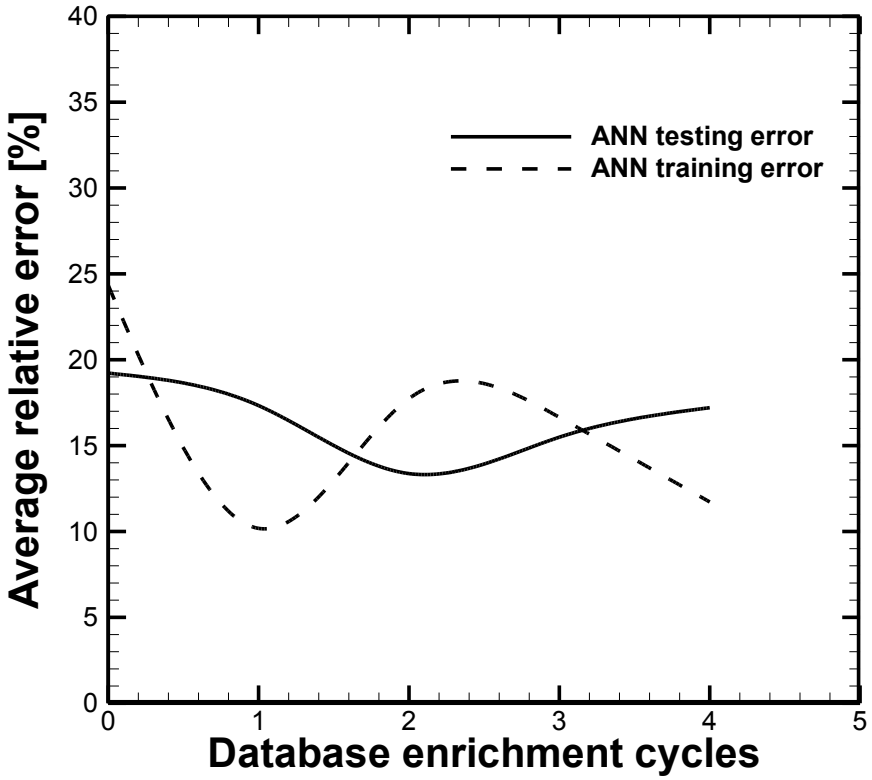

Figure 5-5: Evolution of the ANN testing and training errors with database enrichment during the thermal optimization

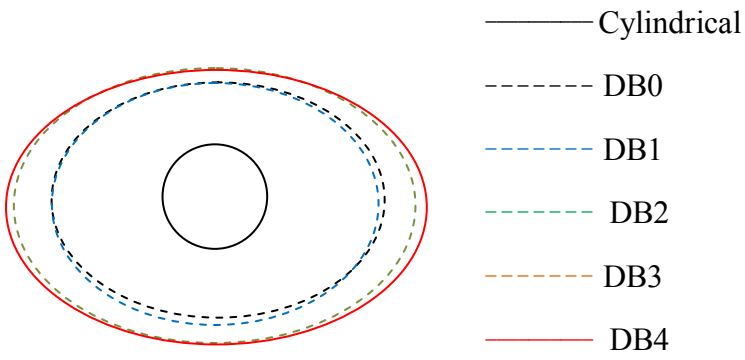

Figure 5-6: Evolution of hole exit shape with database enrichment during the aerodynamic optimization

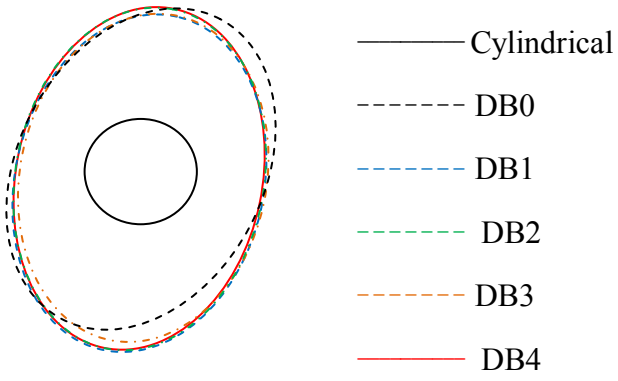

Figure 5-7: Evolution of hole exit shape with database enrichment during the thermal optimization

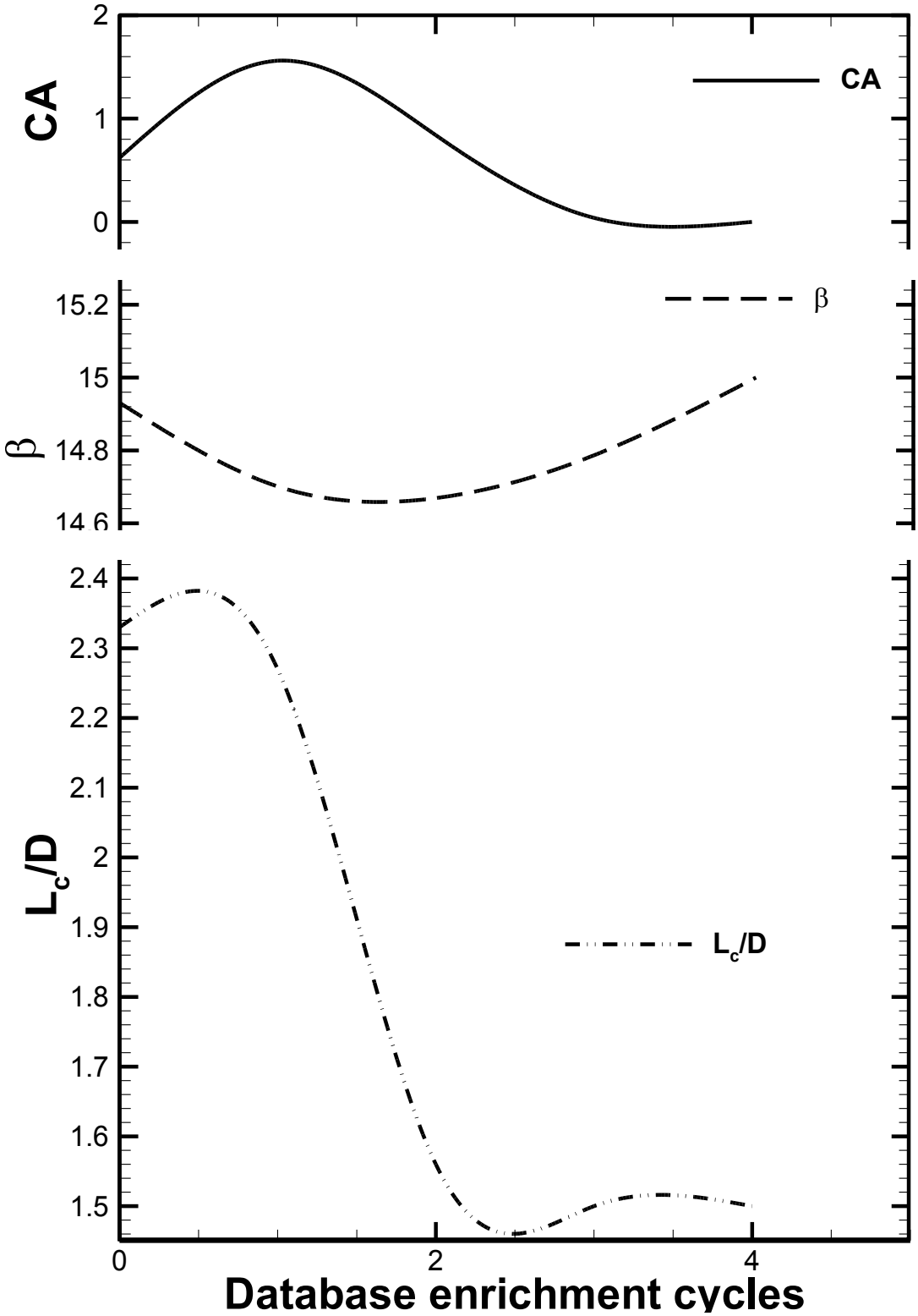

Figure 5-8: Evolution of geometric design variables with database enrichment during the aerodynamic optimization

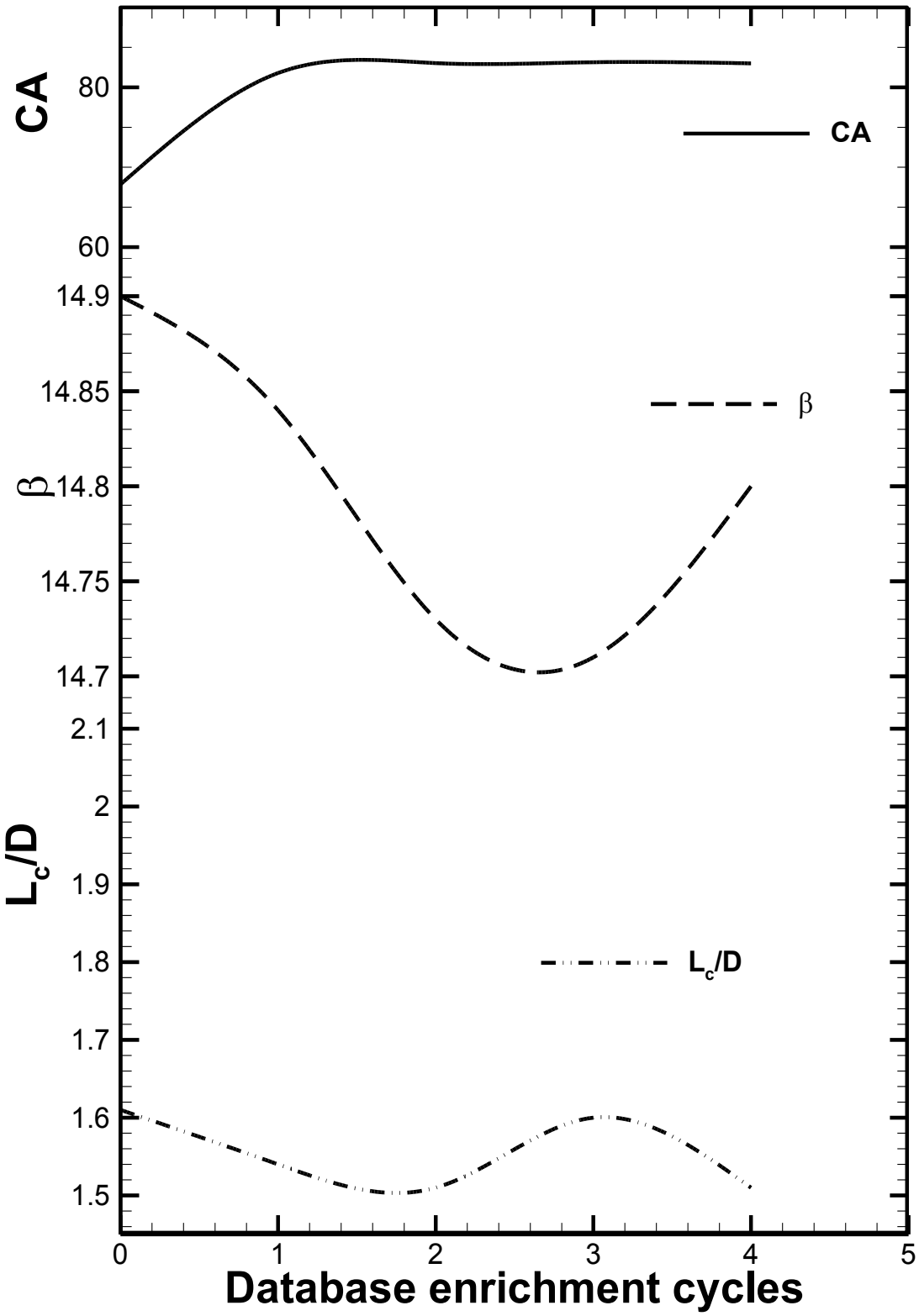

Figure 5-9: Evolution of geometric design variables with database enrichment during the thermal optimization

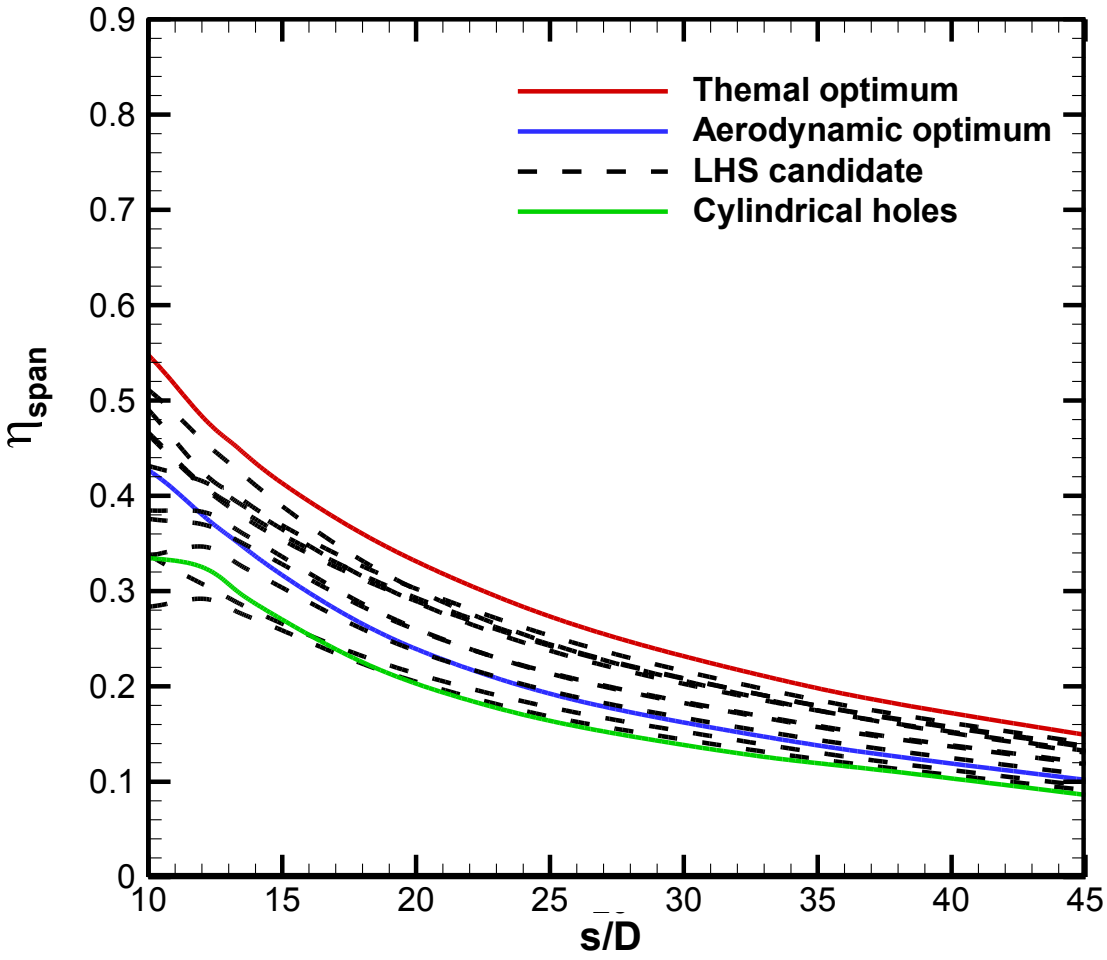

Figure 5-10: Laterally averaged adiabatic cooling effectiveness for the shape single objective optimum solutions

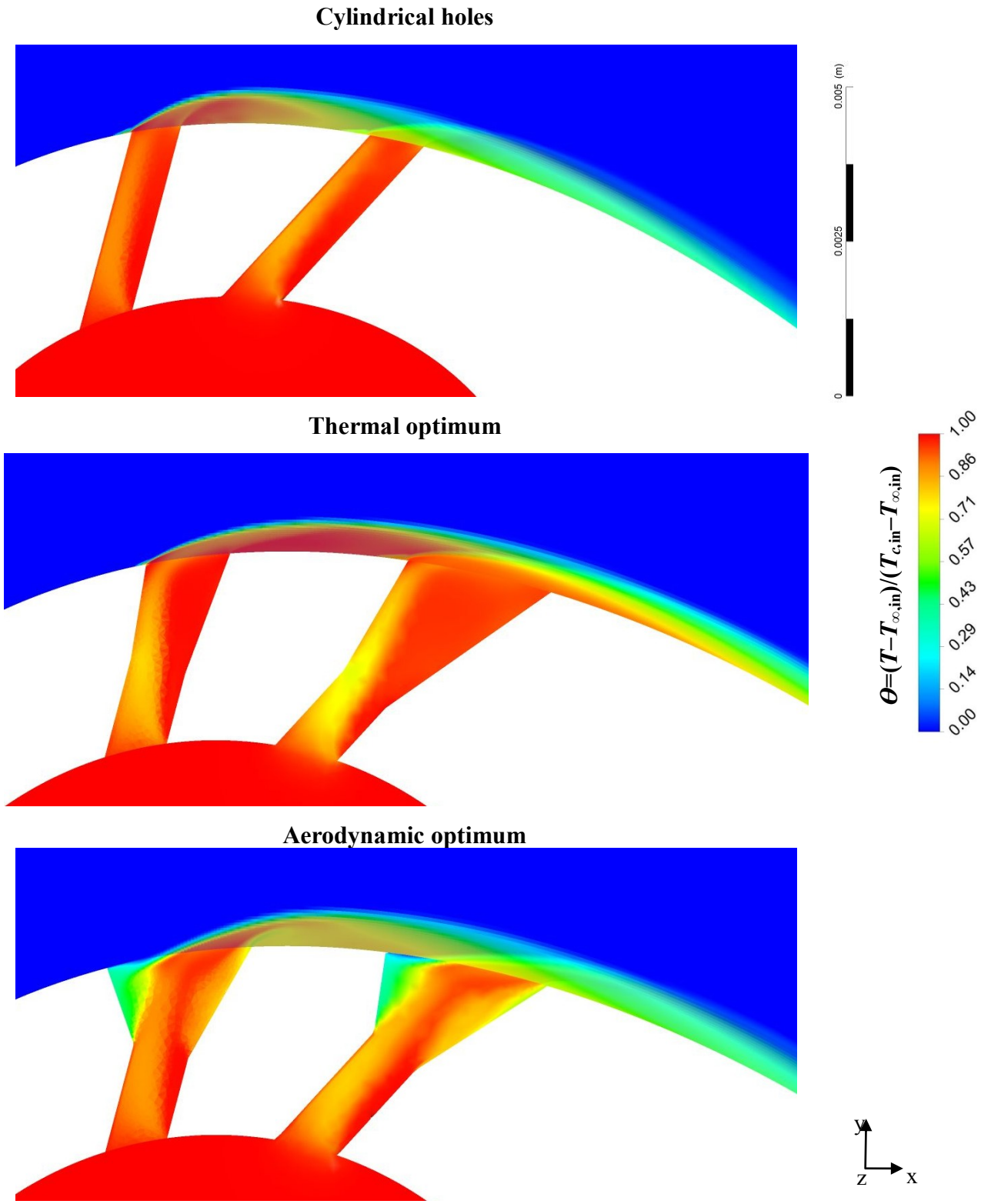

Figure 5-11: Non-dimensional temperature contours on *xy* planes located along the centrelines of the first and second rows of holes

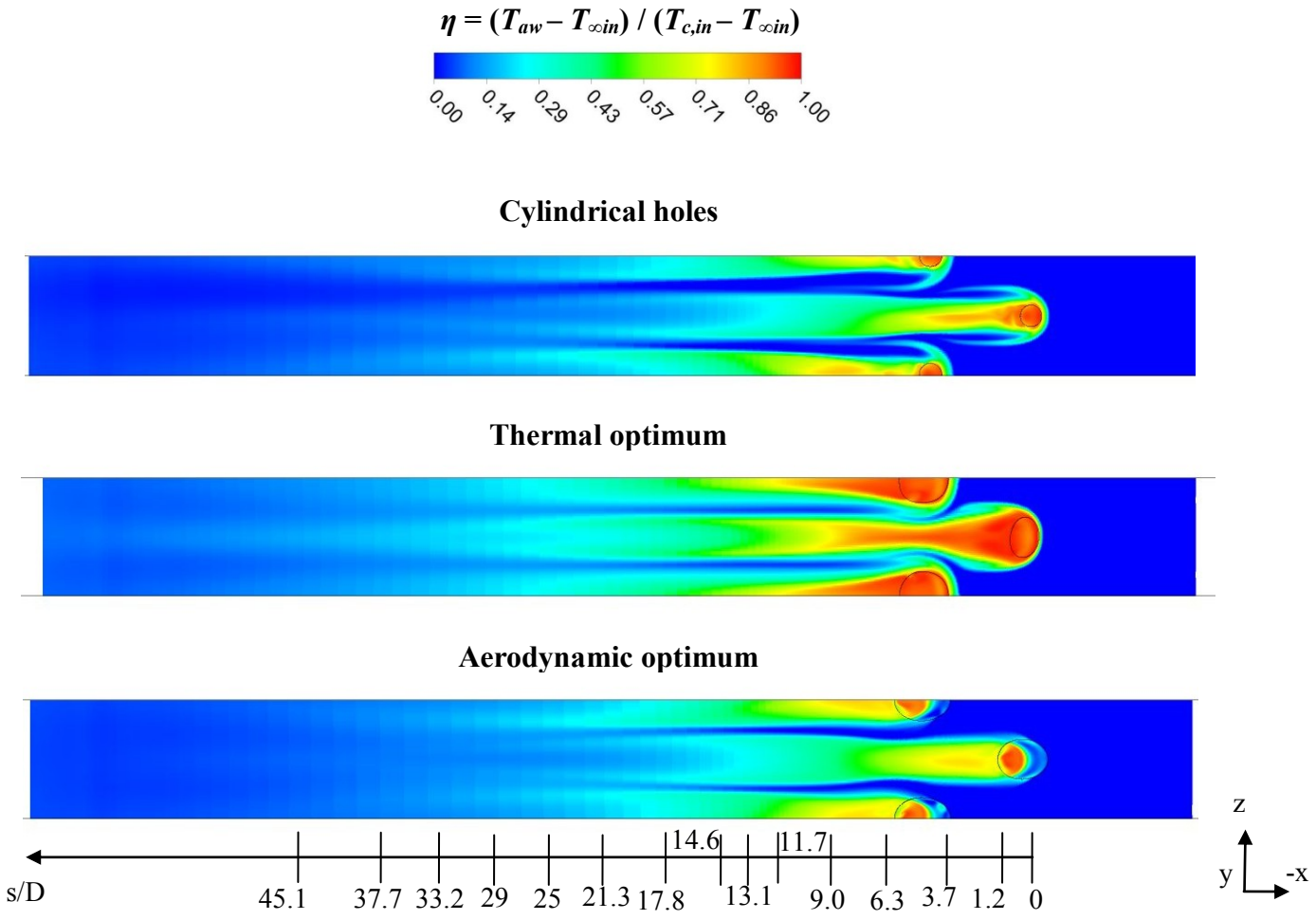

Figure 5-12: Adiabatic film cooling effectiveness contours on the vane suction surface

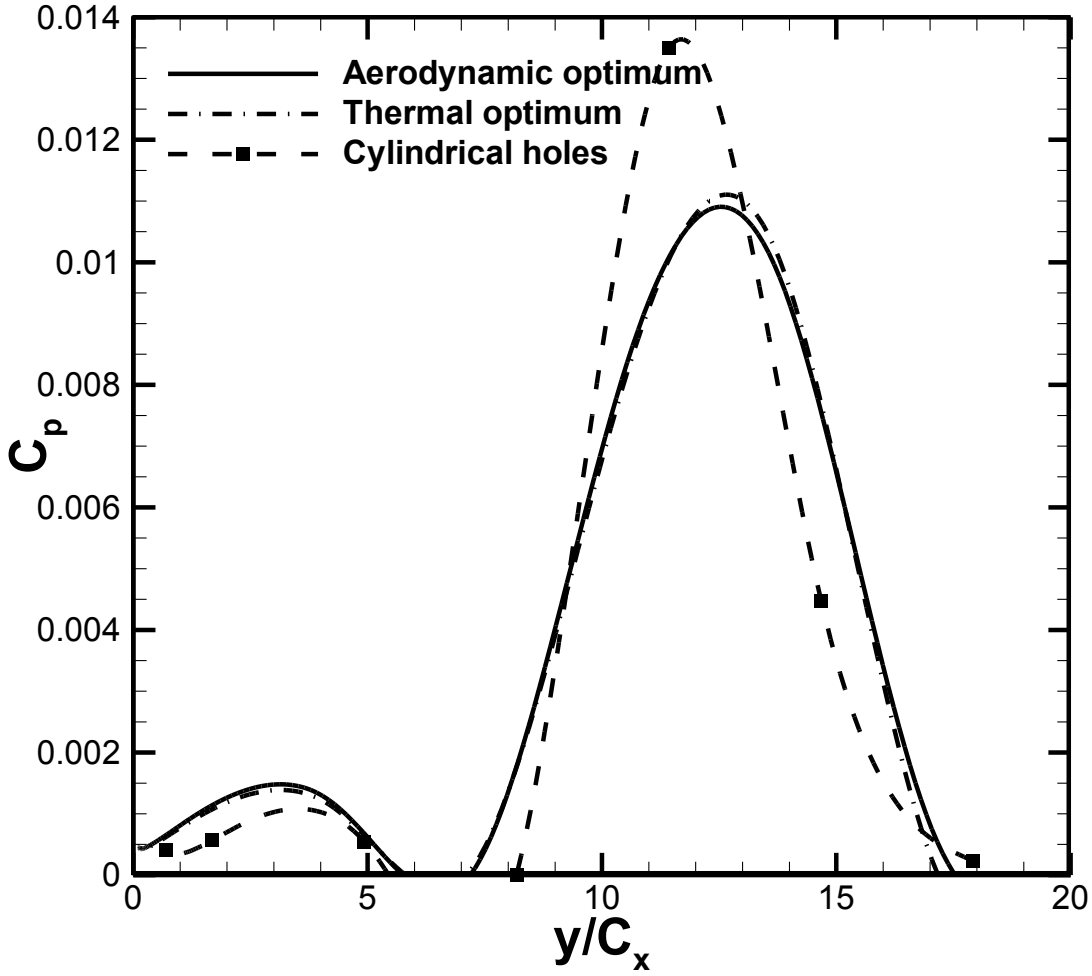

Figure 5-13: Local pressure loss coefficient profiles at one axial chord downstream of the vane trailing edge

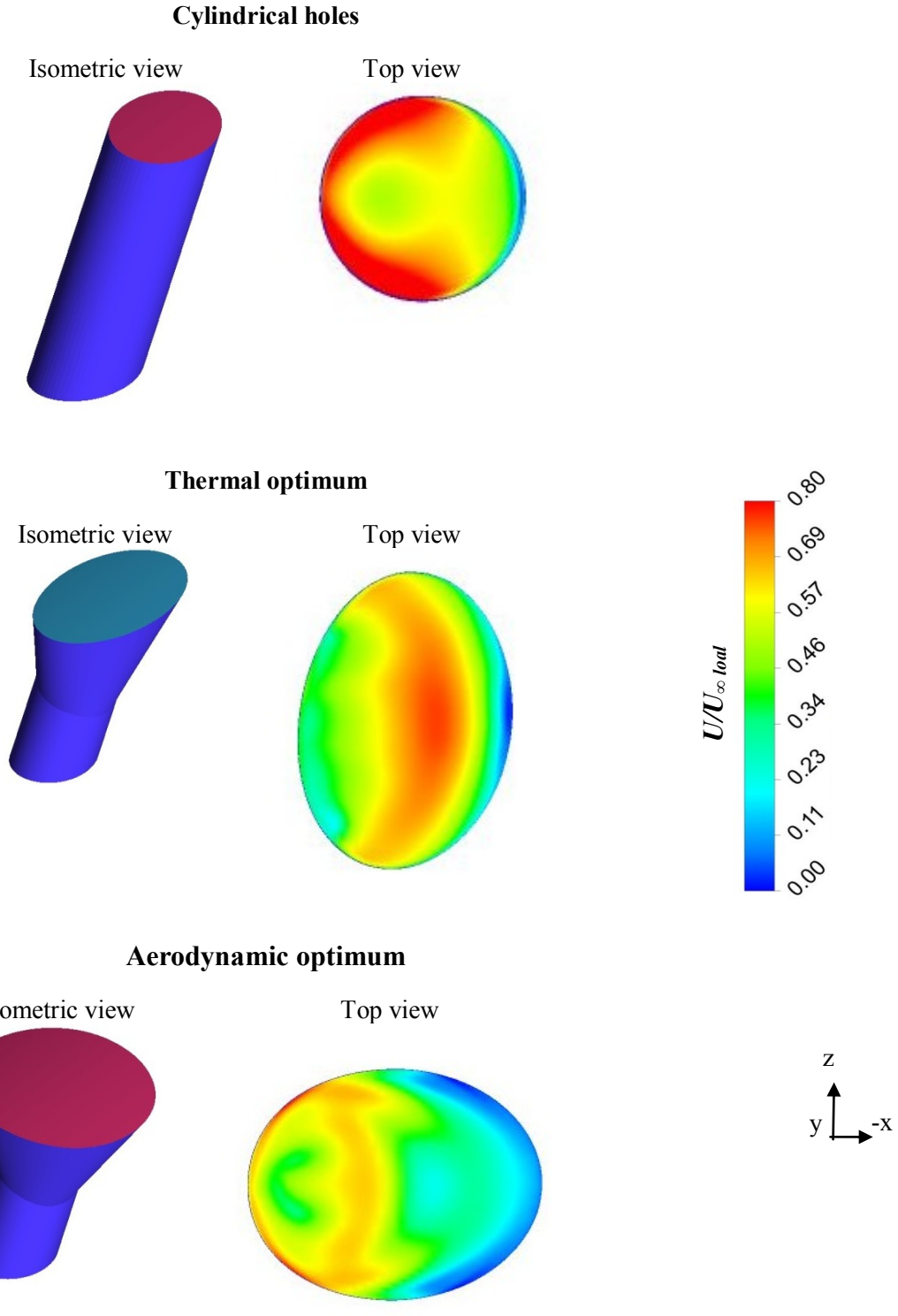

Figure 5-14: Non-dimensional velocity field at the hole exit

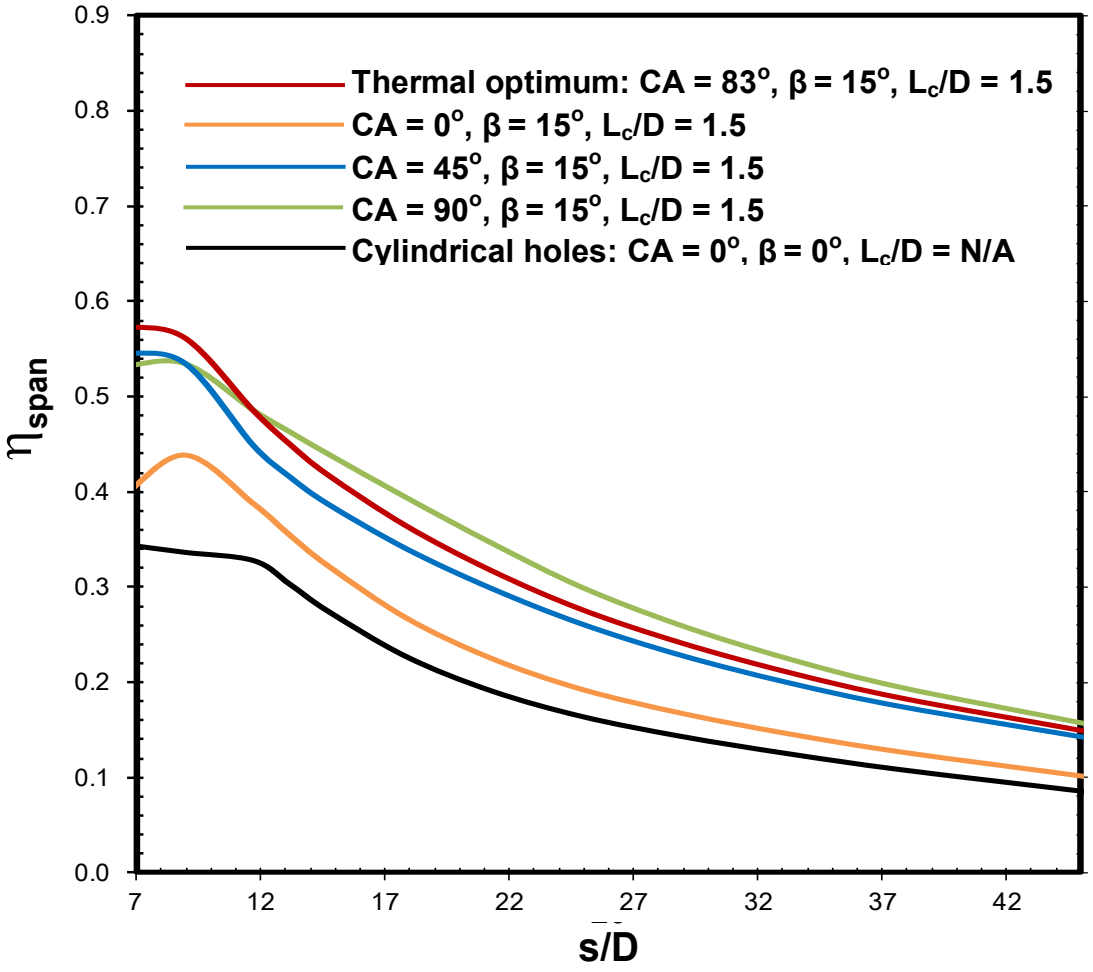

Figure 5-15: Sensitivity of η_{span} to the compound angle

5.4. Discrete film cooling aero-thermal design guidelines

The optimization methodology has revealed novel guidelines for a successful aero-thermal design of discrete film cooling holes. The guidelines established in the present study represent fundamental results for discrete film cooling on the gill region of a turbine airfoil suction surface under subsonic flow conditions. The findings may be summarized as follows:

- Increasing the conical expansion angle β reduces the aerodynamic loss and improves the cooling performance simultaneously. However, too large of an expansion angle may result in a flow re-circulation region inside the expanded portion of the hole, due to the high opening angle of the diffuser, thereby deteriorating the cooling performance.
- Applying a compound angle to an overly expanded hole improves the cooling performance even further. In effect, it was shown that a compound angle may reduce the coolant flow circulation in the diffuser portion, reduce the coolant penetration into the mainstream, and enhance the average coolant velocity at the hole exit. Two dimensional velocity streamlines over the hole exit of the first row of holes allow visualizing coolant flow re-circulation occurring inside the hole expanded portion (or the diffuser), Figure 5-16. The figure demonstrates that rotating the hole exit laterally from 0^o to 83^o eliminates flow re-circulation, which results in better coolant attachment to the vane surface and better lateral spreading therefore, higher cooling performance.
- The compound angle, however, increases the aerodynamic loss as indicated in Table 5-3 and Figure 5-13. Enhancing the average coolant velocity at the hole exit, as shown in Figure 5-14, acts to increase the total pressure loss coefficient and therefore the aerodynamic loss. An axial injection has precedence for minimizing the aerodynamic loss of a shaped hole as it minimizes the coolant mainstream mixing.

- L_c / D allows controlling the diffuser length. Increasing the diffuser length, or reducing L_c / D, may improve the cooling performance and reduce the aerodynamic loss simultaneously. In effect, Figure 5-17 presents the non-dimensional velocity field at the hole exit of the first row of holes for the aerodynamic optimum solution (obtained after the fourth database enrichment or DB = 4) and an optimum candidate obtained at the first optimization cycle, meaning when DB = 0. The optimum candidate at DB = 0 has L_c / D = 2.33, β = 14.93, and CA = 0.62. The difference between the optimum candidate at DB=0 and the global optimum solution at DB = 4 is the L_c / D value. The figure demonstrates that a lower L_c / D, in fact, increases coolant flow diffusion through the expanded exit, and lowers the average coolant flow velocity at the hole exit. This reduces the total pressure loss coefficient and minimizes coolant mainstream interaction therefore minimizing the aerodynamic penalty. Figure 5-18 presents colored contours of the cooling effectiveness over the vane suction surface and demonstrates the beneficial effect of reducing L_c / D onto the cooling performance. It can be seen that reducing L_c / D from 2.33 to 1.5 results in an improved lateral spreading of the coolant over the vane surface, and therefore an enhanced cooling performance. The aerodynamic optimum candidate and aerodynamic optimum solution are compared as well to thermal optimum design. This highlights the previously observed effect of adding a compound angle to an expanded hole, which consists of increasing the cooling effectiveness values, and enhancing the lateral spreading of the coolant, therefore providing a superior cooling performance overall.

Thermal optimum
CA = 83°

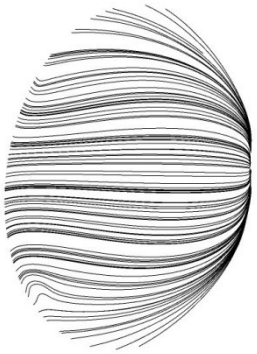

Aerodynamic optimum
CA = 0°

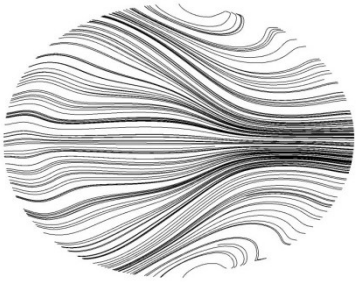

Figure 5-16: Velocity 2D streamlines at the hole exit of the first row of holes

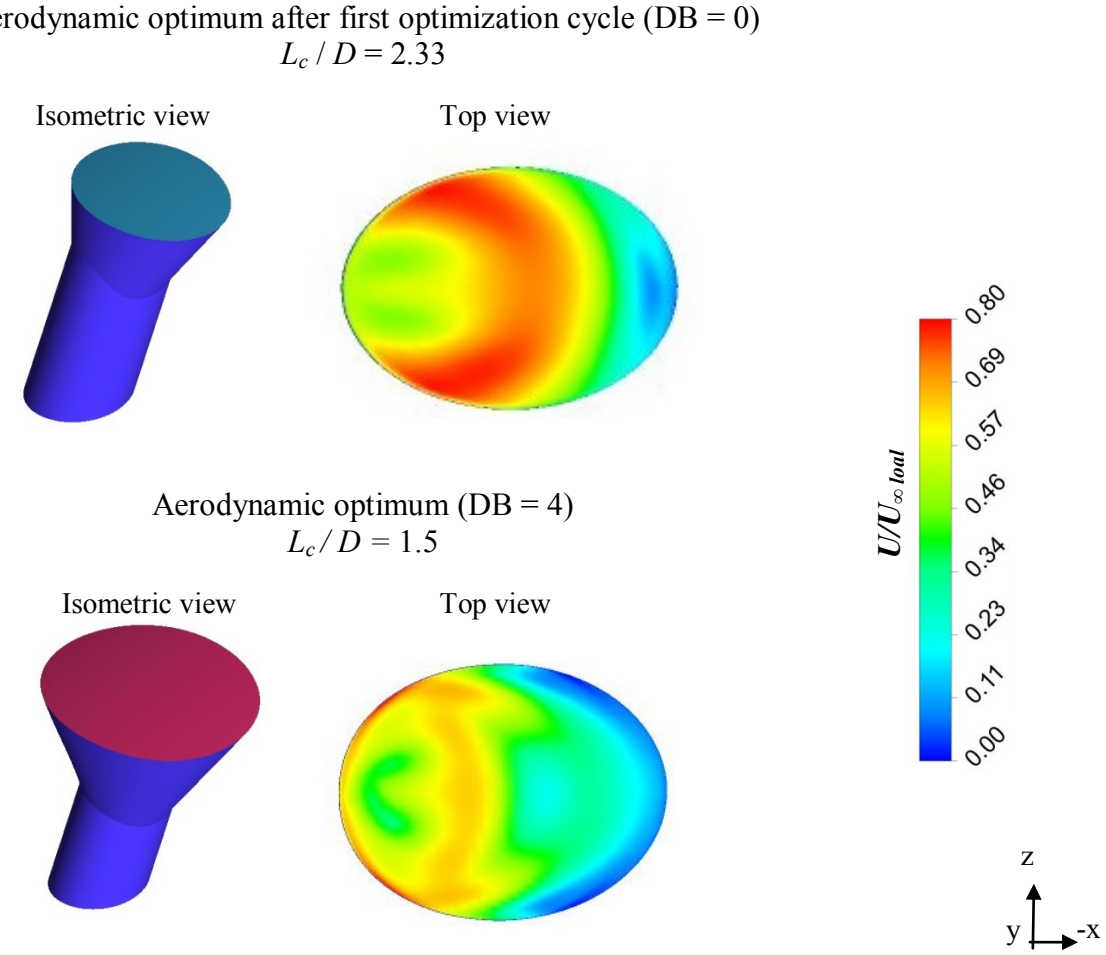

Figure 5-17: Effect of L_c / D on the aerodynamic penalty

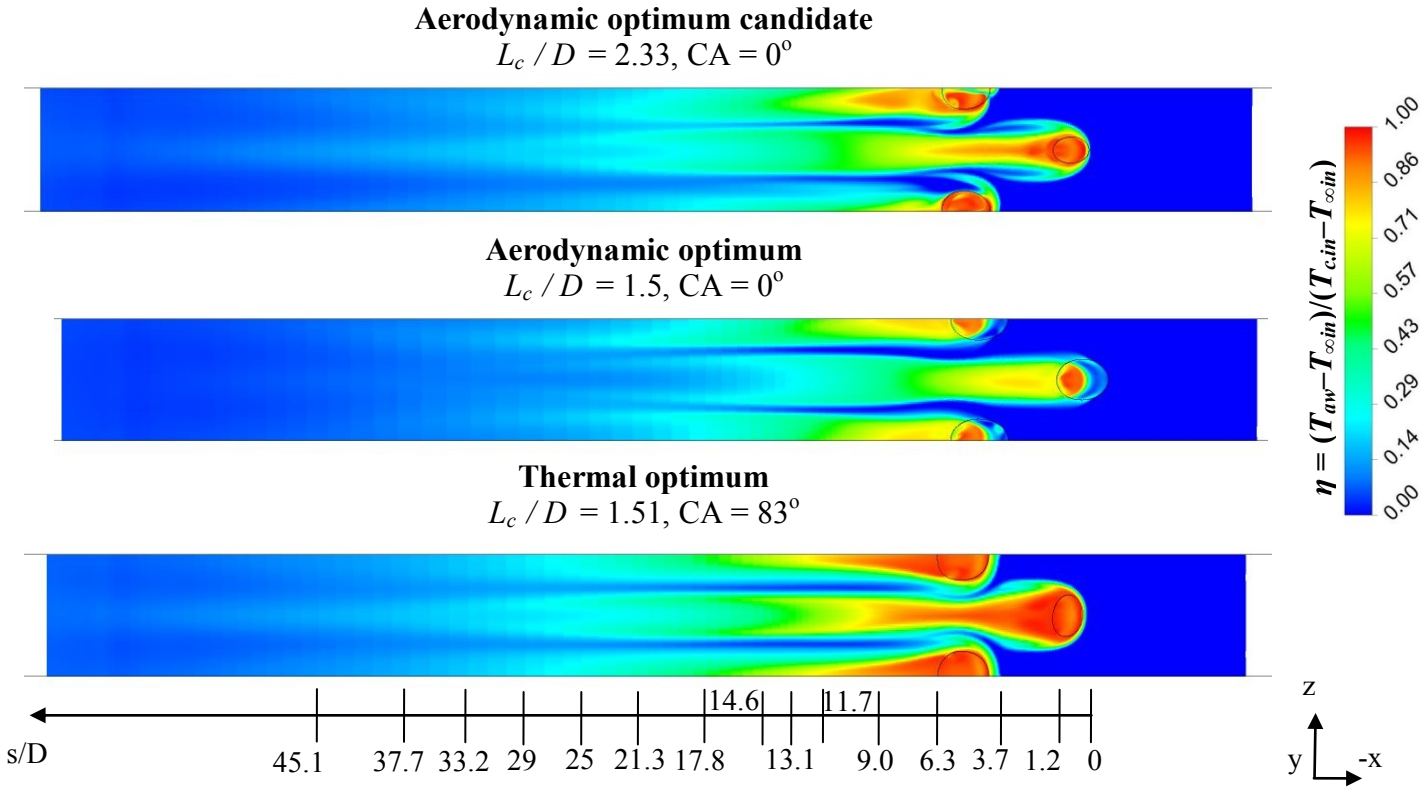

Figure 5-18: Effect of L_c / D on the cooling performance

5.5. Conclusion

The aero-thermal optimization approach presented in earlier chapters is implemented here for the governing geometric parameters employed to define the film hole shape. The design variables consist of the compound angle, the conical expansion angle, and the length to diameter ratio of the non-expanded portion of the hole tube. The optimization objectives remain the same as earlier optimizations and consist of improving the adiabatic film cooling effectiveness while reducing the aerodynamic loss.

A multiple objective optimization allowed generating the Pareto front which encompassed all possible design approaches. The thermal optimum and the aerodynamic optimum corresponded to the two extreme ends of the Pareto front and were generated using a single objective optimization approach.

A purely thermal optimization resulted in a thermal optimum case that yielded over 100% increase in surface averaged adiabatic film effectiveness with respect to the cylindrical reference case according to CFD predictions. The improvement in cooling performance was accompanied with a 22% reduction in aerodynamic penalty with respect to the reference case. This is due to the diffusion of the coolant flow through the expanded hole, which is then released into low velocity mainstream flow. The aerodynamic optimum yielded an aerodynamic loss that was an additional 3% lower than the thermal optimum. The improvement is attributed to a significant reduction in mixing between the coolant and the mainstream due to an axial injection of the coolant. The improvement in aerodynamic penalty is detrimental, however, to the cooling performance which decreased by 53% with respect to the thermal optimum.

The optimization approach allowed defining clear film hole design guidelines for an optimum aero-thermal performance. The current findings are appropriate to discrete suction side film

cooling on a turbine vane under subsonic flow conditions. Furthermore, the optimization methodology is confirmed as a fundamental design tool for aero-thermal performance of film holes in turbomachinery applications.

CHAPTER 6

Conclusion

6.1. Summary of the present findings

Three dimensional aero-thermal optimization of discrete film cooling on the suction surface of a turbine airfoil is presented in this thesis. Film cooling flow is a complex three-dimensional jet in cross-flow/wall bounded shear layer phenomenon that is governed by heat and viscous dissipation in a small dimensional scale. A numerical model was implemented to predict the cooling performance for a film cooled high pressure turbine blade and assessed against experimental measurements. Good qualitative agreement between the CFD prediction and the experiments was obtained.

Furthermore, the ANN proved to be an effective tool for providing low-fidelity predictions of the thermal and aerodynamic performances of a double row of film cooling holes on a high pressure turbine blade. Combined with the genetic algorithm, both numerical tools form a solid automated optimization method for film cooling in turbomachinery applications. Below is a summary of the most significant findings of the present study:

- Proper formulation of the objective function is crucial for the success of the optimization method and allows implementing either single objective or multiple objective optimization approaches. The two complement one another, and analysis of the extremes of a Pareto front provides the basis of a fundamental investigation.

- The aerodynamic and thermal performances of a cooling scheme constitute the direct result of a specific combination of film hole geometry, coolant flow condition, mainstream flow condition, and location of the film cooling scheme.
- Assessment of the accuracy of eddy-viscosity two equation turbulence models is necessary. A turbulence model that can accurately predict the airfoil surface heat transfer coefficient may be capable of accurately predicting the adiabatic cooling effectiveness. However, the opposite is not true.
- The optimization of the coolant flow parameters identified that for an optimum cooling performance the blowing ratio is the maximum possible before inducing coolant separation from the blade surface. On the other hand, the optimum aerodynamic performance was obtained at the minimum blowing ratio. In the case of a high mainstream temperature and a low coolant temperature, the lowest coolant temperature resulted in the optimum cooling performance, whereas a minimum difference between mainstream and coolant static temperatures yielded an optimum aerodynamic performance. Analysis of the Pareto curve extremes revealed that an optimum cooling performance is attributed to a high coolant momentum and a strong attachment to the flow surface at low coolant temperature. An optimum aerodynamic performance is attributed to a minimum viscous and thermal dissipation resulting from a reduction in the interaction between the mainstream and the coolant.
- The aero-thermal optimum on the VKI blade generated a 16% increase in film effectiveness without any significant impact on aerodynamic losses (0.2% reduction in the total pressure loss coefficient).

- The thermal optimum solution on a turbine vane increased the cooling performance by over a 100% with respect to the reference case. The aerodynamic optimum reduced the aerodynamic loss by about 4% with respect to the thermal optimum.
- The shape optimization of the film hole geometry revealed that the optimum thermal design is a widely expanded cone that is highly compounded with respect to the mainstream flow direction. The optimum thermal performance is attributed to strong coolant attachment to the vane surface and wide lateral coverage due to the adequate expansion of the hole exit. It is also attributed to the enhancement in coolant temperature and velocity to maximize film cooling effectiveness values. The optimum aerodynamic design is widely expanded cone that is oriented in the same direction as the mainstream flow. The optimum aerodynamic performance is attributed to a well behaved flow injected parallel to the mainstream flow. The enhanced aerodynamic performance is also a result of the diffusion of the coolant through the expanded hole, resulting in low momentum flow, and a reduced average coolant flow velocity at the hole exit. This contributes to reducing the total pressure loss resulting from the injection of coolant. It also yields a reduced coolant-mainstream interaction, and a lower viscous dissipation of the coolant.
- The optimum thermal hole shape increased the cooling performance by over 100%, whereas the optimum aerodynamic hole shape reduced the aerodynamic loss by about 26% with respect to the reference cylindrical holes.

6.2. Validity of the optimization results

The present research comprises a few parameters differing from current film cooling design available in industry:

- The turbine airfoil investigated in the present work is placed in a linear cascade under subsonic flow conditions as opposed to transonic flow conditions through rotors and stators of first stage high pressure turbines.
- The present work coolant temperature is higher than the mainstream temperature as opposed to temperature ratios (T_c / T_∞) approximating 0.3 in current turbine engines.
- A unity density ratio is observed in the present study as opposed to much higher density ratios approaching 2.5 in current engines.
- Current blowing ratio values are allowed to go as low as 0.3 and as high as 1.2 whereas usual values in gas turbine engines may vary from 0.8 to 5, depending on engine applications.

Despite the above discrepancies with the design norms in current industrial film cooling applications, the present research remains valid as it constitutes an optimization methodology that identified general design guidelines. Such fundamental guidelines may be employed to achieve optimum aerodynamic or thermal performances depending on the designer objectives. These design guidelines are:

- An increase in coolant blowing ratio always results in improved cooling performance as long as coolant separation from the airfoil surface does not occur.
- A reduction in blowing ratio always results in improved aerodynamic performance as the latter is dependent on minimizing coolant viscous dissipation.
- Minimizing the difference in static temperature between the coolant and mainstream flows allows reducing the aerodynamic loss by reducing the corresponding thermal dissipation. The opposite is true for enhancing the cooling performance.

- Expanding conically the hole exit provides stronger coolant attachment and wider lateral spreading over the airfoil surface. It also diffuses the coolant flow and minimizes the aerodynamic loss.
- Applying a compound angle to a conically expanded hole achieves enhancement in cooling effectiveness; it reduces coolant penetration into the mainstream, minimizes coolant circulation inside the diffuser, and enhances coolant velocity and temperature.
- Increasing the length of the conical diffuser portion of the hole allows reducing the aerodynamic loss as it allows diffusion of the coolant flow, and increases cooling effectiveness as it provides better lateral spreading of the coolant.

6.3. Contributions of the present research and future work

The contributions of the present work to the current state of the art available in literature may be summarized as follows:

1. A numerical model was implemented for the prediction of the cooling performance and the corresponding aerodynamic penalty in a high pressure turbine film cooled blade cascade. The model was verified and assessed against experimental measurements.
2. An optimization methodology is proposed and verified experimentally. The success of the methodology procedure is dependent on three main ingredients, a properly formulated objective function, a minimum number of design variables, and an experimentally verified CFD model. The accuracy of the optimization in predicting an optimum aero-thermal design is substantiated experimentally in terms of trend and absolute value.

3. The present methodology is first in literature to combine the genetic algorithm with an artificial neural network and implement this formed optimizer to film cooling applications on a turbine airfoil suction surface.

4. The optimizer was successful in identifying the aero-thermal flow interactions occurring in film cooling gas turbine applications. It identified the opposing effect of blowing ratio and coolant temperature on film cooling performance and aerodynamic loss, and was able to detect the detrimental effect of coolant flow lift-off on the cooling performance.

5. The optimizer was successful in generating novel design guidelines for an optimum aero-thermal performance. The design guidelines were explained in terms of fluid mechanics and heat transfer principles. The design directions can be applied to film cooling turbomachinery applications.

6. The advantage of the present optimization methodology is the substantial reduction in the number of CFD flow simulations necessary to optimize a given film cooling scheme. In fact, the current shape optimization procedure required a minimum number of 10 initially LHS-selected design candidates for three design variables. Only four database enrichment cycles were required to reach the optimum solution. The methodology necessitated a total of 14 CFD simulations only.

7. Traditionally, film cooling research consists in lengthy parametric investigations. Here, the analysis of CFD simulations of the optimum design candidates resulting from the database enrichment cycles allowed conducting a fundamental investigation of the effect of the design variables on the cooling performance and the aerodynamic loss. This minimized the number of CFD flow simulations required.

The present work may be the basis for the following future work:

- The optimum thermal and aerodynamic hole shapes may be validated in the experimental facility of Concordia University.
- The optimization methodology may be applied to more universal problems such as to include both mainstream and coolant flow conditions simultaneously with film hole geometry, and location.
- The manufacturing constraints may be added as constraints to the optimization function.
- The optimization methodology may be implemented under engine-like conditions.

Bibliography

Al-Hamadi, A.K., Jubran, B.A. and Theodoridis, G., Turbulence Intensity Effects on Film Cooling and Heat Transfer from Compound Angle Holes with Particular Application to Gas Turbine Blade, *Energy Conversion and Management,* 39, No. 14:1449-1457, 1998.

Amer, A.A., Jubran, B.A. and Hamdan, M.A., Comparison of Different Two-Equation Turbulence Models for Prediction of Film Cooling from Two Rows of Holes. *Numerical Heat Transfer, Part A: Application: An Internation Journal of Computation and Methodology,* 1992.

ANSYS *ANSYS CFX 12.0 User's Guide*.

Arabnia, M. and Ghaly, W., A Strategy for Multi-Point Shape Optimization of Turbine Stages in Three-Dimensional Flow, *Proceedings of the ASME Turbo Expo,* 2009.

Baldauf, S. and Scheurlm, M., CFD Based Sensitivity Study of Flow Parameters for Engine Like Film Cooling Conditions, *Proceedings of the International Gas Turbine and Aeroengine Congress & Exhibition,* 1996.

Bunker, R.S., A Review of Shaped Hole Turbine Film Cooling Technology, *Journal of Heat Transfer,* 2005.

Camci, C. 1985, *An Experimental and Theoretical Study Film Cooling on a Gas Turbine Blade*, Katholieke Universiteit Leuven.

Camci, C. and Arts, T., Short Duration Measurements and Numerical Simulation of Heat Transfer Along the Suction Side of a Film-Cooled Gas Turbine Blade, *Journal of Engineering for Gas Turbines and Power,* 991-999, 1985.

Chappell, J., Ligrani, P., Sreekanth, S., Lucas, T. and Vlasic, E., Aerodynamic Performance of Suction-Side Gill Region Film Cooling, *Journal of Turbomachinery,* 132:031020-1-11, 2010.

Charbonnier, D., Ott, P., Jonsson, M., Kobke, T. and Cottier, F., Comparison of Numerical Investigations with Measured Heat Transfer Performance of a Film Cooled Turbine Vane, 2008.

Chen, P., Hung, M. and Ding, P., Film Cooling Performance on Curved Wall with Compound Hole Configuration, *Annals New York Academy of Sciences,* 353-360, 2001.

Cho, H.H., Rhee, D.H. and Kim, B.G., Enhancement of Film Cooling Performance Using a Shaped Film Cooling Hole with Compound Angle Injection, *JSME International Journal,* 44:99-110, 2001.

Choi, D., A Navier-Stokes Analysis of Film Cooling in a Turbine Blade, *the American Institute of Aeronautics and Astronautics,* 1993.

Colban, W.F., Thole, K.A. and Bogard, D., A Film Cooling Correlation for Shaped Holes on a Flat-Plate Surface, *Journal of Turbomachinery,* 2011.

Consigny, H. and Richards, B.E., Short Duration Measurements of Heat-Transfer Rate to a Gas Turbine Rotor Blade, *Journal of Engineering for Power,* 104:1982.

Deb, K. 2001, *Multi-Objective Optimization using Evolutionary Algorithms,* John Wiley and Sons.

Dennis, B.H., Dulikravich, G.S. and Han, Z.-., Constrained Shape Optimization of Airfoil Cascades using a Navier-Stokes Solver and a Genetic/SQP Algorithm, *Proceedings of the ASME Turbo Expo,* 1999.

Durbin, P.A., On the k-epsilon Stagnation Anomaly, *International Journal of Heat and Fluid Flow,* 1996.

Elnady, T., Saleh, W., Hassan, I., Kadem, L., Lucas, T., Experimental Investigation of Louver Cooling Scheme on Gas Turbine Vane Pressure Side, *Proceedings of the 14th International Heat Transfer Conference*, 2010

Ferguson, J.D., Walters, D.K. and Leylek, J.H., Performance of Turbulence Models and Near-Wall Treatments in Discrete Jet Film Cooling Simulations, 1998.

Gao, Z., Narzary, D.P. and Han, J.-., Film Cooling on a Gas Turbine Blade Pressure Side or Suction Side with Axial Shaped Holes, *International Journal of Heat and Mass Transfer,* 2007.

Garg, V.K., Modeling of film-coolant flow characteristics at the exit of shower-head holes, *International Journal of Heat and Fluid Flow,* 2001.

Garg, V.K. and Abhari, R.S., Comparison of predicted and experimental Nusselt number for a film-cooled rotating blade, *International Journal of Heat and Fluid Flow,* 18:452-460, 1997.

Garg, V.K. and Ameri, A.A., Comparison of Two-Equation Turbulence Models for Prediction of Heat Transfer on Film Cooled Turbine Blade, *Numerical Heat Transfer, Part A: Applications: An International Journal of Computation and Methodology,* 32:4:347-371, 1997.

Garg, V.K. and Gaugler, R.E., Effect of Coolant Temperature and Mass Flow on Film Cooling of Turbine Blades, *International Journal of Heat Mass Transfer,* 1996a.

Garg, V.K. and Gaugler, R.E., Leading Edge Film Cooling Effects on Turbine Blade Heat Transfer, *Numerical Heat Transfer, Part A: Applications: An International Journal of Computation and Methodology,* 30:2:165-187, 1996b.

Garg, V.K. and Rigby, D.L., Heat transfer on a film cooled blade – effect of flow physics, *International Journal of Heat and Fluid Flow,* 1999.

Ghorab, M.G. and Hassan, I.G., An Experimental Investigation of a New Hybrid Film Cooling Scheme, *International Journal of Heat and Mass Transfer,* 53:4994-5007, 2010.

Gritsch, M., Colban, W., Schar, H. and Dobbeling, K., Effect of Hole Geometry on the Thermal Performance of Fan-Shaped Film Cooling Holes, *Journal of Turbomachinery,* 2005.

Gritsch, M., Schulz, A. and Wittig, S., Film Cooling Holes with Expanded Exits: Near Hole Heat Transfer Coefficients, *International Journal of Heat Fluid Flow,* 2000.

Gritsch, M., Schulz, A. and Wittig, S., Adiabatic Wall Effectiveness Measurements of Film Cooling Holes with Expanded Exits, *Journal of Turbomachinery,* 1998.

Hall, E.J., Topp, D.A. and Delaney, R.A., Aerodynamic / Heat Transfer Analysis of Discrete Site Film-Cooled Turbine Airfoils, 1994.

Harrison, K.L. and Bogard, D.G., Comparison of RANS turbulence models for prediction of film cooling performance, 2008.

Hartsel, J.E., Prediction of Effects of Mass-Transfer Cooling on The Blade-Row Efficiency of Turbine Airfoils, 72-11,1972.

Hassan, O. and Hassan, I., Experimental Investigations of the Film Cooling Performance of a Micro-Tangential-Jet Scheme on a Gas Turbine Vane, Part I: Effectiveness, 2012.

Jackson, D.J., Lee, K.L., Ligrani, P.M. and Johnson, P.D., Transonic Aerodynamic Losses Due to Turbine Airfoil Suction Surface Film Cooling, *Journal of Turbomachinery,* 122:317-327, 2000.

Kline, S.J. and McClintock, F.A., Describing Uncertainties in Single-Sample Experiments, *ASME Mechanical Engineering,* 75:3-8, 1953.

Kusterer, k., Elyas, A., Bohn, D., Sugimoto, T., Tanaka, R. and Kazari, M., The Nekomimi Cooling Technology: Cooling Holes with Ears for High-Efficient Film Cooling, *Proceedings of the ASME TurboExpo,* Vancouver, Canada, 2010.

Launder, B.E. and Spalding, D.B., The Numerical Computation of Turbulent Flows, *Computer Methods in Applied Mechanics and Engineering,* 3:269-289, 1974.

Lee, K.L., Kim, S.M. and Kim, K.Y., Multi-Objective Optimization of a Row of Film Cooling Holes Using an Evolutionary Algorithm and Surrogate Modeling, *Numerical Heat Transfer, Part A: Application: An Internation Journal of Computation and Methodology,* 63:8:623-641, 2013.

Lee, K.D. and Kim, K.Y., Surrogate Based Optimization of a Laidback Fan-Shaped Hole for Film Cooling, *International Journal of Heat and Fluid Flow,* 32:226-238, 2011.

Lee, K.D. and Kim, K.Y., Shape Optimization of a Fan-Shaped Hole to Enhance Film-Cooling Effectiveness, *International Journal of Heat and Mass Transfer,* 53:2996-3005, 2010.

Lee, K.D. and Kim, K.Y., Optimization of a Cylindrical Film Cooling Hole Using Surrogate Modeling, *Numerical Heat Transfer,* 2009.

Lee, K.D., Kim, S.M. and Kim, K.Y., Multi-Objective Optimization of Film-Cooling Holes Considering Heat Transfer and Aerodynamic Loss, 2011.

Lee, K.D., Kim, S.M. and Kim, K.Y., Numerical Analysis of Film-Cooling Performance and Optimization for a Novel Shaped Film-Cooling Hole , GT2012-68529,2010.

Leylek, J.H. and Zerkle, R.D., Discrete-Jet Film Cooling: A Comparison of Computational Results with Experiments, *Journal of Turbomachinery,* 116:358-368, 1994.

Mayhew, J.E., Baughn, J.W. and Byerley, A.R., The Effect of Freestream Turbulence on Film Cooling Adiabatic Effectiveness, *International Journal of Heat and Fluid Flow,* 24:669-679, 2003.

Medic, G. and Durbin, P.A., Toward Improved Film Cooling Prediction, *Journal of Turbomachinery,* 2002a.

Medic, G. and Durbin, P.A., Toward Improved Prediction of Heat Transfer on Turbine Blades, *Journal of Turbomachinery,* 124:2002b.

Mehendale, A.B., Ekkad, S.V. and Han, J.C., Mainstream Turbulence Effect on Film Effectiveness and Heat Transfer Coefficient of a Gas Turbine Blade with Air and CO2 Film Injection, *International Journal of Heat and Mass Transfer,* 37 No.17:2707-2714, 1994.

Mengistu, T. and Ghaly, W., Gas Turbine Blade Design Using Multi-Objective Optimization and Dual Geometry Representation, 2008.

Mengistu, T. and Ghaly, W., Single and Multipoint Shape Optimization of Gas Turbine Blade Cascades, *AIAA,* 2004.

Mengistu, T. and Ghaly, W., Global Optimization Methods for the Aerodynamic Shape Design of Transonic Cascades, *Online,* 2003.

Menter, F.R., Two-Equation Eddy-Visosity Turbulence Models for Engineering Applications, *AIAA Journal,* 32:1994.

Menter, F.R., Langtry, R., Volker, S., Transition Modelling for General Purpose CFD codes, *Journal of Flow Turbulence and Combustion*, 77, Issue 1-4, pp 277-303, 2006.

Nadali, H.N., Karlsson, M., Kinell, M. and Utriainen, E., CFD Based Sensitivity Analysis of Influencing Flow Parameters for Cylindircal and Shaped Holes in a Gas Turbine Vane, *Proceedings of the ASME TurboExpo,* GT2012-69023, Copenhagen, Denmark, 2012.

Nguyen, C.Q., Johnson, P.L., Bernier, B.C., Ho, S.H. and Kapat, J.S., Comparison of FIlm Effectiveness and Cooling Uniformity of Conical and Cylindrical-Shaped Film Hole With Coolant-Exit Temperature Correction, *Journal of Thermal Science and Engineering Application,* 3:031011-1 -9, 2011.

Oyama, A., Liou, M.-. and Obyashi, A., Transonic Axial-Flow Blade Shape Optimization Using Evolutionary Algorithm and Three-Dimensional Navier-Stokes Solver, *Journal of Propulsion and Power,* 612-619, 2004.

Sarkar, S. and Bose, T.K., Comparison of Different Turbulence Models for Prediction of Slot-Film Cooling: Flow and Temperature Field, *Numerical Heat Transfer, Part B,* 1995.

Saumweber, C. and Schulz, A., Effect of Geometry Variations on the Cooling Performance of Fan-Shaped Cooling Holes, 2008.

Silieti, M., Divo, E.B. and Kassab, A.J., The Effect of Conjugate Heat Transfer on Film Cooling Effectiveness, *Numerical Heat Transfer, Part B: Fundamentals: An International Journal of Computation and Methodology,* 56:335–350, 2009a.

Silieti, M., Kassab, A.J. and Divo, E., Film cooling effectiveness: Comparison of adiabatic and conjugate heat transfer CFD models, *International Journal of Thermal Sciences,* 48:2237-2248, 2009b.

Sinha, A.K., Bogard, D.G. and Crawford, M.E., Film cooling effectiveness downstream of a single row of holes with variable density ratio, *Journal of Turbomachinery,* 113:442-449, 1991.

Taslim, M.E. and Khanicheh, A., Film Effectiveness Downstream of a Row of Compound Angle Film Holes, *Journal of Heat Transfer,* 2005.

Thole, K.A., Gritsch, M., Schulz, A. and Wittig, S., Flowfield Measurements for Film Cooling Holes with Expanded Exits, *Journal of Turbomachinery,* 1998.

Walter, D.K. and Leylek, J.H., Computational Study of Film Cooling Effectiveness on a Low Speed Airfoil Cascade - Part II: Discussion of Physics, *ASME 2002 Design Engineering Technical Conferences and Computer and Information in Engineering Conference,* 2002.

Walter, D.K. and Leylek, J.H., Impact of Film-Cooling Jets on Turbine Aerodynamic Losses, *Journal of Turbomachinery,* 122:537-546, 2000.

Walters, D.K. and Leylek, J.H., Computational Study of Film-Cooling Effectiveness on a Low Speed Airfoil Cascade - Part I: Methodology and Validation, 2002.

Wang, X. and Damodaran, M., Aerodynamic Shape Optimization Using Computational Fluid Dynamics and Parallel Simulated Annealing Algorithms, *AIAA Journal,* 39:1500-1508, 2001.

Wilcox, D.C., Simulation of Transition with a Two-Equation Turbulence Model, *AIAA Journal,* 32, No.2:247-255, 1994.

Wright, L.M., McClain, S.T. and Clemenson, M.D., Effect of Density Ratio on Flat Plate Film Cooling with Shaped Holes Using PSP, *Journal of Turbomachinery,* 133:041011-1, 2011.

Yao, J. and Yao, Y.F., Computation study of hole shape effect on film cooling performance, *Journal of Power and Energy,* 225:505-519, 2011.

Yavuzkurt, S. and Hassan, J.S., Evaluation of Two-Equation Models of Turbulence in Predicting Film Cooling Performance under High Free Stream Turbulence, 2007.

York, W.D. and Leylek, J.H., Leading-Edge Film-Cooling Physics - Part III: Diffused Hole Effectiveness, *Journal of Turbomachinery,* 125:252-258, 2003.

York, W.D. and Leylek, J.H., Leading Edge Film Cooling Physics: Part I - Adiabatic Effectiveness, 2002.

Young, J.B. and Horlock, J.H., Defining the Efficiency of a Cooled Turbine, *Journal of Turbomachinery,* 128:658-667, 2006.